EFFECTS OF HUB TREATMENT ON COMPRESSOR ENDWALL FLOW FIELDS

by

Mark Christian Johnson

B.S. Arizona State University
(1983)

Submitted to the Department of
Aeronautics and Astronautics
in Partial Fulfillment of the
Requirements of the
Degree of

MASTER OF SCIENCE IN AERONAUTICS AND ASTRONAUTICS

at the

MASSACHUSETTS INSTITUTE OF TECHNOLOGY

January 1985

Signature of Author _____
Department of Aeronautics and Astronautics
January 18, 1985

Certified by _____
Professor Edward M. Greitzer
Thesis Supervisor

Accepted by _____
Professor Harold Y. Wachman, Chairman
Departmental Graduate Committee
Department of Aeronautics and Astronautics

EFFECTS OF HUB TREATMENT ON COMPRESSOR ENDWALL FLOW FIELDS

by

MARK CHRISTIAN JOHNSON

Submitted to the Department of Aeronautics and Astronautics on January 18, 1985 in partial fulfillment of the requirements for the Degree of Master of Science in Aeronautics and Astronautics

ABSTRACT

An experimental investigation was carried out to examine the influence, on stator passage endwall flow of a slotted hub treatment rotating beneath an axial compressor stator row. The main focus of the investigation was better understanding the mechanism of operation of the treatment. To obtain this, a detailed mapping of the three dimensional, unsteady velocity field near the hub endwall was done, using hotwire anemometry for both a solid hub endwall and an endwall treated with axial skewed slots.The velocity measurements indicate that, with the smooth wall, a large region of blockage occurs near the rear of the blade passage. This blockage is seen to be associated with the hub endwall rather than either the suction surface or the pressure surface of the blade. With axial skewed slots, the blockage is eliminated, and the stalling flow coefficient is reduced by 12%. The measurements showed that the hub treatment induces both a region of removal near the rear of the passage and a strong flow injection, or jet, near the front. The data appears to support the idea that it is the region of removal, and not the jet, which is responsible for the improvement in stall margin.

To my parents, Chuck and Jan, for
their continual support.

ACKNOWLEDGEMENTS

The author would like to express his gratitude to many members of the Gas Turbine Laboratory staff for their assistance. In particular the author is indebted to Professor E.M. Greitzer for his guidance and encouragement in all phases of this project. In addition, the author thanks Capt. R.N. Gamache for his many helpful suggestions and advice. The efforts of J. Nash and R. Andrews in the mechanical aspects of the project are also appreciated. Special thanks is extended to Mr. Zongan Hu and Dr. H.W. Shin for their assistance in designing the experiment. Furthermore, the author is grateful for the efforts of Dr. C.S. Tan, W. K. Cheng, W. Cooke, and A. Barron.

This work was supported by the Air Force Office of Scientific Research, Contract Number F49620-82-k-0002, Dr J.D. Wilson, Program Manager, and was carried out while the author was a trainee in the Air Force Research in Aero-Propulsion Technology (AFRAPT) program.

CONTENTS

CHAPTER 1
INTRODUCTION

1.1 INTRODUCTION

Compressor stability is a major concern for manufacturers of aircraft engines and industrial power plants. Figure 1.1 is a schematic of a typical compressor performance map, which shows that, for a given rotational speed, as the mass flow decreases the pressure rise increases. However, if the machine is throttled enough, the compressor will stall and the pressure rise may fall sharply. In an engine, compressor stall can have detrimental affects and may even lead to loss of the engine. Because of these adverse consequences, extensive efforts have been made to improve the stall margin of compressors, in other words, to move the stall line to the left.

It has been experimentally observed that the application of slots or grooves over the tips of compressor rotor blades can have a strong affect on the stall margin. One example of this is found in the data of Smith [1] whose results are presented in Fig 1.2. This figure presents the compressor characteristics for a smooth (casing) wall and a casing with axial skewed slots. As seen in the figure, this 'casing treatment' improved both the stall margin and the peak static pressure rise of the compressor. Other examples can be found in the references listed in [1] and [2].

In experiments performed by Smith [1] and Greitzer [2] it

was observed that the treatment reduced the boundary layer blockage associated with the endwall and retarded the onset of stall. It also appeared that the mechanism by which the treatment works is associated with the relative motion between the blades and the treatment. In view of this, it is natural to ask whether a rotating treatment moving underneath a row of stator blades would also be effective in improving stall margin.

The work of Cheng et.al [3] showed the successful application of this idea. It was demonstrated there that a 'hub treatment' rotating beneath a row of cantilevered stator blades could lead to a substantial improvement in stall margin of the treated blade row. Also it was found that hub treatment reduced the blockage associated with the endwall, just as casing treatment did. These similarities give strong indication that both casing treatment and hub treatment work by the same mechanisms. This is important because it enables researchers to investigate the area of tip treatment, in general, by analyzing hub treatment, thus avoiding the use of rotating instrumentation. This is the approach taken in the present experiment.

The work reported in [2], and [3] also points up another important result. It appears that one can often make a distinction between two types of compressor stall. One of these, termed 'blade stall', is roughly a two-dimensional type of stall where a significant portion of the blade span has a

separation on the suction surface. The other, termed 'wall stall', occurs when a separation occurs on the endwall. These two phenomenon are shown schematically in figure 1.3. The research mentioned above has shown that tip treatment is only effective when the type of stall is wall stall.

1.2 OBJECTIVE

The overall goal of this project is to investigate a particularly effective treatment, the axial skewed slot. In particular, the specific objective of the present effort is to determine the mechanisms by which this treatment improves stall margin.

In the past a great deal of attention has been focused on a particular feature of this treatment, namely, the strong flow injection, or jet, which occurs near the leading edge of the slots. There may be two reasons for this. First, the jet is very striking and it seems reasonable that it would have a large affect on the flow field. Second, at first glance, data seems to support the idea that the jet is responsible for the improvement in stall margin.

An illustration of this second point is seen by considering a particular set of data taken by Takata [4]. Takata carried out a parametric investigation of many treatments, including the axial skewed slot, recorded the changes in stall margin and measured the flow in the slots. He determined that an axial slot, skewed such that the slot faced

the pressure surface, lead to the greatest improvement in stall margin, while, an axial slot, skewed such that the slot faced the suction surface, actually lead to a decrease in stall margin (compared to the solid wall). Furthermore, he found that in the former, termed 'axial skewed slot', there was a strong flow in the slots and a corresponding jet, whereas in the later, termed 'reverse axial skewed slot', there was very weak flow in the slots and a correspondingly weak jet. This trend can be explained by noting the fact that in the reversed skewed case the flow is not oriented in such a way as to readily enter the slots. This point is an important one and will be discussed further below. Graphs showing Takata's results are shown in Fig. 1.4.

Figure 1.4 presents time traces of flow velocity in the slots for both the axial skewed slot and the reverse skewed slot. The figure clearly shows that only in the axially skewed slot case is there appreciable flow in the slots and therefore a strong jet.

Takata also did some recent work [5] which investigated the affect of various treatments on efficiency. He found that the treatments most effective at improving stall margin were the treatments which lead to the greatest reduction in efficiency.

Takata's study was typical of several parametric studies all of which showed the axial skewed slot as being effective at improving stall margin and having associated with it a strong

jet. However to have a jet there must also be a region where flow is removed from the mainstream and this is another characteristic of the axial skewed slot.

In view of this, one can ask whether this removal is more important to the effectiveness of the treatment*, and there are at least two reasons why the answer to this question may be yes. First, it would be consistent with data. Takata showed that the reversed skewed axial slot, which worsened stall margin, had very little slot flow therefore very little removal, whereas the axial skewed slot, which improved the stall margin, had appreciable slot flow and therefore appreciable removal. Second, since this removal must take place near the rear of blade row the region of removal could act directly on the region where wall stall might form.

From the arguments presented above it is clear that there is an important question to answer about which mechanism, injection or removal, is important to the operation of tip treatment. To answer this, an experimental approach was employed to examine the passage endwall flow field for both a smooth hub and a treated hub rotating under the stator. In order to compare of the flow phenomena associated with the two builds. The results of the experiment provide strong evidence that it is the removal that is responsible for the improvement in stall margin rather then the jet, which is merely a consequence of this removal.

* This question has also been posed (independently) by N. A. Cumpsty

CHAPTER 2
EXPERIMENT DESIGN

2.1 DESIGN OBJECTIVES

There are two distinct objectives to be met in the design of this experiment. It is crucial that the stator be stall limiting and furthermore that the type of stall be wall stall emanating from the hub endwall. It is also required that the data acquisition system be precise and flexible enough to resolve all the important regions of the flow field.

2.2 COMPRESSOR DESIGN

The design of the compressor used in the present experiment is described by Cheng et.al [3] and only a brief review of that work will be presented here. The compressor is a one stage low speed axial compressor. The design of the compressor aimed at having the low rotor loading at the stator stall point so that the IGV and rotor act as merely a 'flow generator' for the stator. Thus, in choosing the blade setting angles, it was desired that the rotor have a high stagger angle relative to the stator. The requirement of high stator hub loading was satisfied by using rotor blades with very low twist. This created only a small static pressure rise across the rotor hub relative to the tip which in turn loaded the stator hub. Also, to further 'decouple' the stator and rotor a large axial distance was left between them. This allowed ample

room for any non uniformities, such as rotor blade wakes, to smooth out.

To determine appropriate geometry for a wall stall situation, a correlation presented by Koch [7] was used. This correlation relates wall stalling static-pressure-rise coefficient of a compressor stage to the blade passage geometry, tip clearance, blade row axial spacing and reynolds number. This correlation provided design criteria (stagger, tip clearance) which were implemented to insure wall stall at the stator hub. The detailed design and analysis of the compressor blading was done with an axisymmetric compressor design program developed by Hearsey [8].

2.3 DATA ACQUISITION GRID

There were two major concerns in generating the data acquisition grid. First, since later modifications were expected, it was desired to have the capability to modify the grid easily. Second, in order to better understand the flow phenomena, it was desired to display the flow field in different ways. To insure flexibility in the grid generation procedure, a computer program was written to allow easy modification of the data acquisition grid. This proved very useful as the grid was changed many times.

To allow flexibility in displaying the flow field, the grid locations were placed such that they aligned on several

different surfaces. The velocity vectors are projected onto these various planes and displayed in two dimensional views. To illustrate this consider Fig 2.1, which presents the projection of a constant radius surface that cuts through the blade row of interest. For convenience in discussion this surface will be referred to as a 'radial plane' (although the actual surface is not a plane). It is one of the 2-D planes on which the projections of the velocity vectors can be viewed. Furthermore, if one imagines stacking several of these radial planes on top of one another at various radial locations it is clear that the grid locations will align on several other types of 2-D planes. One such plane is parallel to the blade stagger angle, another is normal to the axis of the compressor, and another is parallel to the axis of the compressor. The grid was designed this way because it was not known, a priori, what would be the best way to view the flow field. The geometry described above, which allows viewing of the flow field in four different ways, was incorporated into the computer program mentioned above.

To determine the necessary radial and axial extent of the data acquisition grid a preliminary investigation of the flow field was carried out using a hotwire. This showed that all of the important phenomena associated with the treatment were found below 25% span. Furthermore it was found that the phenomena were confined within the passage. However, for completeness, the axial extent of the grid went slightly beyond the passage.

The final grid consisted of seven radial planes for the smooth wall and eight for the treated wall. Each plane has 97 locations. The radial range of these planes was from 2% span to 27% span. The circumferential and axial extents can be seen in Fig 2.1. Note that there are also points in the adjacent passage. These additional points were useful for examining flows across the blades, and for providing a redundancy, on the measurements made in the main passage.

2.4 POSITIONING SYSTEM

A part of the present work was the design and construction of a system to position the hotwire probe in the blade passage at the locations specified in Fig. 2.1. A detailed presentation of the design, geometry, calibration, and use of the system developed is given in appendix A. However, to provide a better understanding of the material presented in chapters 3 and 4, a brief description of the positioning system is presented here.

Figures 2.2 and 2.3 show the configuration of the positioning system. Figure 2.2, a top view, shows the major components of the positioning system. These components are the traversing mechanism (screw actuator), the 15/1 reduction gear box, the angular transducer, and the stepping motor.

Figure 2.3 presents a side view of the positioning system. This provides a clearer view of how the traversing mechanism is

moved by the stepping motor and the 15/1 reduction gear box and how this movement affects the position of the probe relative to the stator. The angular transducer, which can be seen in Fig. 2.2, rotates as the angle of the traversing mechanism changes and the output of the transducer is calibrated with the traverser angle. The information provided by the angular transducer is read by computer and used to determine how the stepping motor should be moved. An interface between the computer and the stepping motor closes the loop and allows for automated control of the traverser angle.

The heart of the positioning system, the traversing mechanism, or screw actuator, is also computer controlled. It traverses the probe radially and also rotates the probe about its axis. The actuator operates by stepping motors on both radial traverses and angular rotations. The total length of radial traverse motion is 203 mm and is divided into 1000 locations. Similarly, the angular range of motion spans 360 degrees and is divided into 1000 positions. The traversing mechanism is controlled by a microprocessor based control system, which in turn is interfaced and controlled by a computer.

The circumferential location of the probe is controlled by moving the entire traverser platform (this circumferential movement is the only link of the positioning system that is not automated). The traversing platform is mounted on an inner casing sleeve that slides relative to the outer casing. This inner sleeve is shown in Fig 2.3 and is moved via a chain and

gearbox, which are not in the figure, located on the bottom of the compressor. To measure the circumferential location a linear displacement transducer is mounted on the traversing platform. The output of this transducer is calibrated with circumferential location.

CHAPTER 3
DESCRIPTION OF EXPERIMENT

3.1 EXPERIMENTAL FACILITY

The experiment was conducted on a single stage research compressor driven by a variable speed D.C. motor. The compressor was equiped with an inlet bell mouth with a screen honeycomb combination, an inlet guide vane, a discharge throttle, a plenum/ exhaust duct, and a downstream fan. The compressor had stationary casing treatment over the tips of the rotor blades and the rotating hub was run with both a smooth wall and a treated wall. A cross sectional schematic of the compressor showing blading and treatment locations is given in Fig 3.1. Both rotor and stator have a constant chord of 38mm, a nominal solidity at midspan of 1.0, and constant camber of 30 degrees. Further information about of the geometry is presented in Table 3-1 and the details of the rig design are given by Cheng [6].

The inlet bell mouth and honeycomb screen are new modifications to the rig. These were added because it was desired to eliminate effects of objects near the entrance to the rig. In addition, a newly fabricated acoustic box designed by Cheng was used in front of the compressor to reduce noise during testing.

All of the measurements were taken at 2600 RPM for both the smooth wall (untreated) and treated wall builds. This

corresponds to a rotor tip Mach number of .24 and a Reynolds number based on blade chord at the stator midspan of 1.0×10^{5} at the stall point. .pa Reynolds number effects on the compressor characteristic were examined by Cheng et.al [3] and found to be small.

The compressor RPM was set and measured by a magnetic pickup mounted next to a sixty tooth gear which rotates with the shaft. This was connected to a frequency counter through which one can read the shaft RPM directly.

The hub treatment consists of axial slots skewed at a 60 degree angle to the radial direction. A presentation of the hub treatment geometry showing angles and dimensions is presented in Fig. 3.2. the slots are skewed circumferentially such that they face towards the pressure surface. The slots rotate under the middle 90% of the stator tip chord. The slot aspect ratio (axial length/tangential width) is 3.0, and the radial depth is 30% of the axial length.

3.2 INSTRUMENTATION

The pressure instrumentation consisted of 20 total pressure kiel-head probes, 24 hub and casing static pressure taps, and 1 pitot tube. These were located at five axial stations as shown in Fig. 3.3. A detailed description of the pressure instrumentation was presented by Prell [9]. In the present experiment, the only modification made to the previous

instrumentation was the addition of the pitot tube, which was used in measurement of flow rate (see section 3.3).

A hotwire anemometer was used for time resolved velocity data as well for overall examination of flow behavior at various flow coefficients. The anemometer output was monitored and recorded on a Tektronix 486 digital storage oscilloscope. To maneuver the hotwire to desired locations the automated positioning system described in chapter 2, was used.

3.3 STEADY-STATE DATA ACQUISITION AND REDUCTION

Acquisition of steady-state pressure data was done by a 48 channel scanivalve pressure scanner which was read by an analog to digital converter and controlled by a microcomputer. A calibration of the transducer used in the scanivalve is presented in figure 3.4. The standard deviation of the measurements was .0223 IN. H20. The pressures measured in the experiment, such as the static pressure rise across the stator were on the order of 1.00 IN. H20 therefore the relative error is approximately 2%.

The free stream axial velocity, Cfs, was determined by a measurement of dynamic head at station 1. The static pressure at this station was determined by the average of the four casing static pressure taps and the static port of the pitot tube.

The midspan total pressure was acquired by averaging the

readings from the pitot tube and the two total pressure probes not in the wakes of upstream struts. The circumferential average total pressure was then obtained by correcting for the presence of the struts. This correction, which was calculated using a simple control volume analysis of the flow around the struts, was found to be slightly less than 5 per cent of the dynamic pressure.

To determine the annulus average axial velocity, Cx, it was necessary to have a measurement of the blockage due to the displacement thicknesses of the endwall boundary layers. To acquire this blockage an inlet calibration was performed by measuring the inlet velocity profiles. A detailed presentation of the results of the inlet calibration is given in chapter 4.

In this report data is presented in non-dimensional form; mass flow is presented as Cx/U (where U is mean rotor blade speed), pressure differences are non-dimensionalized by $\frac{1}{2}pU^2$, and velocities are normalized by Cx, the annulus averaged axial velocity.

3.4 HIGH RESPONSE DATA ACQUISITION AND REDUCTION

Acquisition of time resolved velocity data was by hotwire anemometry. The technique used, which allows for the acquisition of 3 dimensional unsteady velocity vectors, employs a single hotwire probe. This is a modification of that presented by Wagner and Okishi [10]. A detailed presentation of the calibration, acquisition, and reduction procedures

involved with this technique is given in appendix B. However, for completeness a brief account is presented here.

To obtain the direction and magnitude of flow the single hotwire is immersed in the flow and rotated about its axis. The output of the wire is measured at three different angular locations. From these three measurements, along with the proper calibrations relating probe output to pitch angle, yaw angle, and speed, a three dimensional vector is derived.

This technique works well when the flow direction is within the calibration range of the probe. However, if flow angles are varying widely or if they take on extreme values, the probe may not be able to resolve the velocity vectors. This problem occurred in the present work. To illustrate, consider the probe geometry presented in Fig. 3.5. Typically, the probe slant angle is set to 45 degrees, however, in the present work this was found to give an inadequate range of calibration. Specifically, the pitch angles were found to be very large and could not be resolved with the standard 45 degree slant angle wire. Because of this a hotwire with no slant would work and this was employed, and this gave satisfactory results.

In the present work both the time averaged flow field and the time resolved flow field were obtained. The time averaged flow fields were obtained by averaging the hotwire measurements over 13.2 rotor revolutions which corresponds to 2200 slot passings or 580 rotor blade passings. The slot passing

frequency was 7K, therefore, to prevent aliasing, the measurements were taken at 32khz and 10000 samples were averaged. Far fewer samples would have sufficed over much of the flow field, however, since it took no more time, and it was desired to have precise results, 10000 was the number of samples averaged for all of the time averaged data. This procedure was repeated for all three of the angular orientations required, then this data was stored for later reduction.

To obtain time-resolved data a phase lock system was used in conjunction with an ensemble averaging technique. The phase lock system consisted of a photodetector mounted over the tips of the rotor blades and a Schmitt trigger to discriminate the signal from the detector. All of the rotor blades were painted with flat black paint except one which was polished. When the polished blade passes the photodetector the Schmitt trigger 'opens' and triggers a train of 25 pulses at a frequency of 40 khz. The accuracy of this trigger system is limited by a 1MHZ crystal oscillator which was used to generate the pulse train. Since the rotor was rotating at 43HZ, this corresponds to an angular resolution of .015 degrees which is much less than the resolution of the hotwire used. This pulse train is used to externally trigger an analog to digital converter which samples the hotwire output.

The procedure outlined above yields one digitized 'trace' of the hotwire signal over a specific portion of a rotor

revolution. This procedure is repeated and many such traces are acquired and then ensemble averaged. This averaging process retains any periodic characteristics of the signal while removing any random noise or turbulence. After some experimentation, it was found that an ensemble average of 250 traces was sufficient to return a smooth final trace. A comparison of the actual traces and the ensemble averaged traces shows that they each have the same features but the ensemble averaged traces are smoother. The resultant time traces cover a period of time equal to 1.5 rotor blade passings or, in the treated build, 5 slot passings.

	Rotor	Stator
Hub diameter	444 mm	444 mm
Casting diameter	597 mm	597 mm
Number of blades	44	46
Chord	38 mm	38 mm
Solidity at midspan	1.0	1.0
Aspect ratio	1.9	1.9
Camber	30°	30°
O. D. stagger angle	65°	40°
Midspan stagger angle	60°	42.5°
I. D. Stagger angle	55°	45°
Blade clearance	.8 mm	1.5 mm

CHAPTER 4
EXPERIMENTAL RESULTS

This chapter presents the results of the experiment described in chapter three. Also a simple analysis is presented as a model of the phenomena. This is used to provide justification for the conclusions the author proposes.

4.1 INLET CALIBRATION

To have an accurate measure of mass flow, or average axial velocity (Cx), it was necessary to know the blockage due to the boundary layers on the endwalls. This was especially important in view of the fact that major modification had been made to the inlet as discussed in chapter three. This blockage is defined as the ratio of the blocked area to the total annulus area. The average Cx and the freestream axial velocity (Cfs) are related to the blockage ratio by the simple relation.

$$\frac{C_x}{C_{FS}} = 1 - \frac{A_{BLOCK}}{A_{TOTAL}} \qquad (4.1)$$

The left hand side of eq. 4.1 was measured by performing a radial traverse of the annulus. A typical velocity profile obtained is presented in Fig 4.1. Note that the casing boundary layer is thicker than that at the hub; this is expected since the casing boundary layer has a longer distance to develop (see Fig 3.1).

Because the machine was to be operated at many flow rates, it was necessary to determine the blockage ratio as a function

of flow condition. To this end, the blockage ratio was calculated foarange of flow rates and correlated as a function of Reynolds number. Figure 4.2 shows the results of this correlation with the Reynolds number based on freestream velocity and surface distance measured from the beginning of the bellmouth to the calibration station. A linear curve fit of this data was used through out the experiment to calculate Cx from the measured Cfs and Reynolds number. It seems strange that the blockage ratio does not decrease with increasing Reynolds number. This may be due to transition to turbulence as the Reynolds number increases.

4.2 COMPRESSOR PERFORMANCE

Constant speed compressor characteristics were taken at 2600 rpm for both the smooth wall and treated wall builds. The data is presented as pressure rise, DP, nondimensionalized by $\frac{1}{2}pU^2$ versus Cx/U, where U is mean rotor blade speed. The first performance map presented, figure 4.3, is the overall compressor characteristic for the complete stage where delta-P is defined as the stator exit static pressure minus the total pressure at the inlet to the IGV. The figure shows the results for both builds and indicates the corresponding stator stall points, i.e. the point of onset of rotating stall in the stator.

Note that due to large pressure rises in the rotor, the improvement in stator performance is not brought out in this

figure. However, the figure does show that the overall characteristic in the smooth build is negative, indicating that the rotor is operating far from stall and that the stator is stall limiting.

A comparison of the stator static pressure rise characteristics are shown in Fig 4.4, where DP is defined as the stator exit static pressure minus the stator inlet static pressure. Here it can be seen that the application of hub treatment has resulted in a substantial reduction in stator stalling flow coefficient. The treated and smooth wall stalling flow coefficients are .295 and .337 and correspond to non-dimensionalized peak static pressure rises of .145 and .084 respectively.

These results are in close agreement with previous speedlines taken on this rig and presented in [9]. The only minor difference is a flow coefficient shift to left of approximately 2.7% (corresponding to a change in flow coefficient of .007 at stall.) The reason for this is that previously the inlet total pressure was taken to be ambient when in fact there is a small loss due to the struts upstream of the inlet station (see section 3.3)

The discussions above, along with the performance maps and the evidence given in [3], imply that the stator hub is wall stall limited. To examine in more detail whether the stall a series of radial traverses were made with a hot wire inside the blade passage near the rear of the passage at midpitch. These

traverses were performed at flow coefficients just above and below the stalling flow coefficient of .337. The results are shown in Fig 4.5 in the form of hotwire traces. Although these only provide qualitative information it is clear that at either flow coefficient the output of the hotwire decreases in magnitude as the span decreases. At Cx/U = .330 the flow becomes increasingly disturbed as the span decreases and it becomes impossible to tell whether the flow is forward or reversed. This is typical of part span rotating stall. These plots provide further qualitative evidence that the stall is emanating from the hub endwall.

As discussed in [6], it thus appears that the objectives of the design of the compressor have been met; The hub treatment has a pronounced effect on the stator performance and the machine is stall limited by the stator hub endwall. Establishment of these conditions paved the way for the main thrust of this work, to acquire the three dimensional velocity field.

4.3 AVERAGE VELOCITY FIELD

The velocity fields for both the smooth and treated builds were taken at a 'near stall' flow coefficient of .350. This corresponds to a distance from stall of 3.7% and 15.7% in axial velocity for the smooth and treated builds respectively.

To better understand the flow, velocity vectors are

presented from three different views. A radial view, which presents the vectors projected onto a plane normal to a radial line, a chordal view which presents the vectors projected onto a plane parallel to the blade stagger angle, and an axial view which presents the vectors projected onto a plane normal to the axial direction. In each case, the origin (tail) of the vector is the true location where the measurement was made. In addition, at the origin of each vector a symbol is printed which indicates the direction of the flow normal to the view. An O indicates flow out of the paper and an X indicates flow into the paper. This relays no information about the magnitude of the normal component, however that magnitude can be seen by looking at another view.

For easy comparison, the views of time averaged velocity vectors are presented in pairs, one for the smooth wall build, and one for the treated build. First, the radial views will be presented and discussed. These will provide detailed information about the axial and tangential velocity components. To visualize the radial components of velocity, the chord and axial views will then be presented. These upcoming figures provide information which is at the crux of the present work and appears to settle the question about which phenomenon, the jet or the removal, is more important to the treatment operation.

Figures 4.6 and 4.7 present radial views for two different radial locations very near the hub. In this, and succeeding figures, the radial location is described in terms of percent

span (span is defined as the radial distance from the hub divided by the total radial distance from the hub to the casing).

Figure 4.6, which is at 2% span, corresponds to a location that is in the clearance, below the bottom of the blade, which is at 3% span. For the smooth wall there is a large region of low axial velocity which covers the rear of the passage over nearly the entire pitch. It should be emphasized that this is not a suction surface separated region, which it might appear at first glance, because this plane is below the blade as indicated above. Furthermore, it seems unlikely that the low momentum fluid associated with the suction surface boundary layer is being transported down the blade and then to the center of the passage. This point is seen more clearly in the smooth wall view of Fig 4.7, where the blockage , though less pronounced, is seen to be in the center of the passage. In this view, which is at 6% span and therefore well above blade bottom, it is clear that the vectors near the suction surface are following the surface with no separation. This is to be expected, based on the analysis by Cheng [6] of the stator D-factors.

The treated flow field, displayed in Figures 4.6 and 4.7, shows a much different flow structure. In the figures the axial extent of the treatment slots is indicated. In Fig. 4.6 the most striking difference is seen near the leading edge, where the velocity is extremely high (about four times C_x), and

almost completely tangential in direction. This is due to strong flow injection from the slots into the mean flow. This flow injection, or jet, is present across the entire pitch of the passage and extends from the leading edge to about 40% axial chord. The jet travels across the passage and impacts the blade pressure surface which diverts it downstream. The region near the leading edge is dominated by this jet and, at points, the flow is actually moving with a negative component of axial velocity. This appears as a blockage to the incoming flow which diverts radially over the jet. This diversion is seen, in this view, by noticing the O's at the vector origins. It seems unlikely that this jet induced blockage is beneficial and it may simply be dissipative so that the high total pressure of the jet is lost.

A less striking, but perhaps more important, characteristic of the treated wall flow field is the removal which takes place near the trailing edge. This effect can be seen in both Figures 4.6 and 4.7 by noticing the X's at the origin of the vectors. When one compares this to the smooth wall views of figures 4.6 and 4.7 it can be noted that the region of flow removal in the treated flow field (X's at the vector origins) is precisely the region of flow blockage in the smooth wall flow field (O's at the vector origins).

One can also examine chordal views of the flow which show radial flows more clearly. Figures 4.8 through 4.10 display these for three different pitch locations of 8%, 38%, 68% from the pressure surface. In all three figures the smooth wall

data indicates large blockage near the rear of the passage, especially near the midpitch plane (i.e. the 38% pitch data in Fig. 4.9). In the treated wall data this blockage is eliminated. Furthermore, the regions of strongest flow removal in the treated view are precisely the regions of largest blockage in the smooth wall views. Very clearly, the low momentum fluid has been sucked into the slots and reinjected near the leading edge in the form of a high velocity, high total pressure jet.

The jet and its effects are also visible in the chord views of Figures 4.8 through 4.10. Near the leading edge, the jet is clearly visible since it has a large radial velocity component. Furthermore, in Figure 4.8, which shows chordal views at 8% pitch, the path the jet follows after it impacts with the pressure surface is quite clear. Here it is seen that the jet proceeds diagonally along the pressure surface and exits the passage from (roughly) 20% to 30% span. From the discussions pertaining to Figures 4.6 and 4.8, therefore one can piece together the entire path of the jet. From the radial view of Figure 4.6, the jet is seen to travel across the passage and impact the pressure surface, whereas, from the chordal view of Figure 4.8, the jet is seen to travel diagonally across the blade and exit the passage from 20% to 30% span. The important point here is that, the jet never approaches the the region where, in the smooth build, the main blockage occurs.

The final views of the flow field, the axial views, are presented in Figures 4.11 and 4.12. In Figure 4.11, which is at 20% axial chord, the features associated with the leading edge are seen a little more clearly. For the smooth wall view the flow has only a slight upward bias. This is expected since the blockage typical of the smooth build occurs further downstream. The treated view of Figure 4.11 shows the jet very clearly moving across the passage towards the pressure surface.

The views of Figure 4.12, which are at 78% axial chord, show the features of the downstream side of the blade passage. With the smooth wall the blockage is very clear. Once again , it is emphasized, the blockage is not associated with either blade surface, but is rather in the middle of the passage and emanating from the endwall. Furthermore, in the treated build data of Figure 4.12, the blockage is gone and the flow is moving strongly downward into the slots. Once again, it appears that this removal, seen in the treated build, is responsible for cleaning out this region of low momentum fluid.

This situation in which the blockage is emanating from the endwall and is seen in the middle of the passage is not particular to this rig. This phenomenon has been reported before by Greitzer et al [2], and a contour plot showing their results is presented in Figure 4.14. The data in [2] is for casing treatment applied to a rotor tip and Fig. 4.14 shows a comparison of contours of relative total pressure at the rotor exit for a smooth casing and a treated casing. In the contour plot for the smooth wall there is a region of low total

pressure near the casing endwall which seems very similar to the flow shown in the present work. This is important for two reasons. First, it indicates that the results found by this author are not an anomaly; this situation may exist in many rigs (see also [1] for another illustration of this). Second, the rig used by Greitzer showed this situation occurring in the rotor, not the stator as in data presented here, with the blockage forming on the casing endwall. This means that this phenomenon is not particular just to stators but rather the basic concepts developed should hold for (rotor) casing treatment as well.

In all of the figures which show radial components, i.e. Figures 4.8 through 4.12, the radial extent of all the important features that we wish to examine is within approximately 25% span from the hub. As an example of this Fig 4.13 shows a radial plane at 22% span, and it can be seen that the treated and smooth wall flows are almost identical. The differences are only near the trailing edge region of the pressure surface where the remnants of the jet are still visible.

4.4 UNSTEADY VELOCITY FIELD

The time resolved velocity fields were also measured at a flow coefficient of .350 for both treated and smooth builds. As discussed in chapter three, to obtain time resolved data, an analog to digital converter, triggered by the phase lock

system, was used to sample the hotwire signal. The digitized samples were then ensemble averaged. A detailed account of the high response data acquisition technique is given in appendix B, but the result is (ensemble averaged) time resolved traces of each of the velocity components at each position in the data acquisition grid. The resultant time traces cover a period of time equal to 1.5 rotor blade passings or 5 slot passings.

To display the unsteady effects, views of the velocity vectors are presented at different instants in time. These views are instantaneous 'pictures' of the flow field. For the treated wall data the plots also include the instantaneous locations of the slots.

The views are again presented in pairs for easy comparison. However, this time the pairs will be from the same build but separated in time by 1/2 the period of the relevant time scale for that build as discussed below. For the smooth build this time scale is the rotor blade passing period. For the treated build the time scale is the period of one slot passing.

In addition to the instantaneous views of the flow field, time traces of the velocity components are also presented. These contain all of the time resolved information available at a given physical location. Careful consideration of these graphs yields an in-depth understanding for the unsteady flow at a given location.

Figure 4.15 presents two radial views of the smooth wall build at 6% span. Again, these are separated in time by one-half rotor blade passing. The two can be seen to be virtually identical. This result is typical of the entire smooth wall flow field and merely indicates that the wakes from the upstream rotor are small, nearly mixed out, and most importantly have very little effect on the flow in the stator. This, of course, is a desirable situation and is a result of the facility design, where (as discussed in chapter 2) the rotor was intended to be a 'flow generator' and thus was placed a large distance upstream of the stator. The implication of Fig. 4.15 is that unsteady effects are small and the time averaged flow field is representative of the instantaneous flow fields at all times.

A final piece of evidence for this point is presented in Fig 4.16, where time resolved velocity components are displayed for a location at the leading edge, midway between the blades, at 22% radial span. In this figure all three velocity components and absolute magnitude are graphed versus time and in each graph the level is nearly constant except for small fluctuations which are the remnants of the rotor blade wakes.

Unlike the smooth build, the treated build has regions of strong unsteadiness. These can be seen in figures 4.17 and 4.18. The views in these figures are separated in time by one-half slot passing time. Figure 4.17 presents a radial view of the treated hub flow field at 2% span. One can see differences in the velocity field near the leading edge of the slots where

the individual jets are exiting. This is due to the fact that some portions of the passage are flowing 'normally', at an angle of roughly 45 degrees to the axial direction, whereas other portions of the passage are flowing almost tangentially. The 'normal' flow is slipping in between two adjacent slots whereas the large angle flows are in the jets. In some locations, these are, in fact, in the negative axial direction.

Figure 4.18 shows an axial view at 20% axial chord (i.e. at the second axial grid location). The same situation visible in the radial view of Fig 4.17 is visible in the axial view of figure 4.18, however the latter shows the radial extent of the unsteadiness.

In either Fig 4.17 or 4.18 the maximum variation of the velocity vectors can be observed by comparing the same vector in the two instantaneous views. A better representation of the magnitude of these changes, however, is provided in Fig 4.19 which shows the time resolved velocity components for a location near the slot leading edge, in the middle of the passage, at 2% radial span. In this region the unsteadiness is most marked and Fig 4.19 shows the unsteadiness clearly.

In each of the components graphed in Fig 4.19 the slot passings are visible, however the effect is most dramatic for the axial component. The axial velocity is seen to vary from levels near Cx to substantial negative values, as the jet from the slot sweeps by. Furthermore, if one compares the radial and axial components it is seen they are 90 degrees out of

phase, i.e. ,when the axial velocity is low, corresponding to a jet passing by, the radial velocity is high. So a jet, when it passes by, not only results in a reversal in the axial component but also in a strong outward radial velocity. It seems doubtful that the incoming boundary layer is benefitted in any way by this.

This region of violent unsteadiness is confined to a small region near the slot leading edge, below 6% span. Figure 4.20 shows this point by displaying axial velocity traces (which showed the largest unsteadiness) for various spans. In each graph of this figure the locations were near the leading edge at midpitch. Clearly by 6% span most of the unsteadiness is gone and by 22% span all that is visible is the small fluctuations associated with rotor blade wakes as in figure 4.16. Figure 4.21 displays the same information as figure 4.20 except at a location near the slot trailing edge at midpitch. In this figure the unsteadiness is seen to be much weaker and it decays more rapidly with distance than in 4.20. In general it was found that the unsteadiness is not the main phenomena. It was found that the jet mixes rapidly on a slot-to-slot basis and that in fact the only region where unsteadiness was significant was at the leading edge below 6% span.

CHAPTER 5
ANALYSIS

This chapter provides some simple first order calculations of the jet direction and magnitude which are compared to the experimental results. An argument referring to the direction of the jet relative to the mean flow is also given. Lastly, a discussion concerning the effect of the slots on compressor efficiency is presented. Note that these should be regarded as preliminary hypotheses.

5.1 JET DIRECTION AND MAGNITUDE

The geometry of the jet flow is presented in Fig 5.1 In this figure Vjet is the velocity of the jet relative to the moving slots, Vmeas is the velocity of the jet that is measured by the hotwire (also the absolute velocity), and Vh is the velocity of the slots. There are two assumptions made about the direction of the jet. First, it is assumed that the jet has no axial component. This is reasonable based on the data presented in Ch. 4. Secondly, it is assumed that the jet relative velocity leaves at angle equal to the slot angle, As. Basic geometrical relations yield the following relation between Vmeas, Vjet, and Vh.

$$V_{MEAS} = \sqrt{V_{JET}^2 + V_H^2 + 2 V_H V_{JET} \sin\alpha} \qquad (5.1)$$

To calculate Vmeas, which of course is needed to compare with the experimental measurements, a value for Vjet is needed.

To estimate this value, one may apply the steady Bernoulli's equation to the slot flow in the slot reference frame. This is a very crude estimate since unsteady and viscous effects are neglected. A statement of Bernoulli's equation is

$$P_{T.E.} + \tfrac{1}{2}\rho V_H^2 = P_{L.E.} + \tfrac{1}{2}\rho V_{JET}^2 \qquad (5.2)$$

where Pte and Ple are the static pressures in the blade passage at the slot trailing and leading edge locations. This assumes that the relative dynamic head of the flow entering the slots is approximately .5pU^2. This is a good approximation since U^2 is much larger than Cx^2. Equation 5.2 may be rearranged to

$$V_{JET} = \sqrt{V_H^2 + (P_{T.E.} - P_{L.E.})^2/\rho} \qquad (5.3)$$

From speedline data the static pressure rise across the stator is about one tenth the relative dynamic head of the flow coming into the rotor, therefore the second term under the square root in equation 5.3 is negligible. Using this the following simplified result is obtained.

$$V_{JET} \approx V_H \qquad (5.4)$$

Combining 5.1 with 5.4, and using alpha equal to 60 degrees, one finds that Vmeas equals 1.7Vh. This corresponds to Vmeas equal to 4.1Cx. If one measures the velocity vectors displayed in figure 4.17 it is found that the strongest part of the jet has a velocity of 3.8Cx, only 10% under the predicted value. In the weaker part of the jet discrepancies from the prediction approach 25% and this merely indicates that there are viscous

effects, which are not accounted for, which dissipate the jet velocity.

Now that the jet direction and magnitude have been estimated, it is important to compare those features to the direction of the incoming flow. Figure 5.2 presents the geometry which shows the direction of the jet relative to the incoming flow is nearly normal. This is based on free stream incoming velocity. An analogous situation occurs in casing treatment, where the proper reference frame is the relative frame and, again, the jet and the incoming flow are almost perpendicular. The geometry of Fig. 5.2 is supported by data presented in chapter 4.

The geometrical arguments presented above will be different for other rigs where the vector diagrams will differ. However, the general result will still apply; the jet is not oriented in such a way as to impart momentum in the direction of the flow. Also the jet is not acting near the trailing edge where trouble is expected. On the contrary, the jet, with its high velocity (4Cx), is entering normal to the mean flow near the leading edge. It seems unlikely that this is beneficial and is responsible in any way for the stall margin improvement associated with this treatment.

5.2 EFFICIENCY DISCUSSION AND CALCULATIONS

In addition to improved stall margin, another

characteristic of the treatment tested is reduced efficiency. Although the current experiment made no measurement of efficiency this effect has been shown in the past. To determine the cause of this reduction it is useful to do a simple analysis to determine the ratio of the treated efficiency to the smooth walled efficiency. First consider the definition of efficiency

$$\eta = \frac{W_s}{W} \tag{5.5}$$

where W is actual power supplied and Ws is the useful power out or the isentropic work. This equation may be manipulated as follows:

$$\eta = \frac{C_p T_{IN} \left(\frac{T_{OUT_s}}{T_{IN}} - 1 \right)}{\tau \omega} \tag{5.6}$$

T_{IN} = average total temperature in

T_{OUT_s} = average isentropic temperature out

τ = shaft torque

ω = shaft angular speed

P_{IN} = total pressure in

P_{OUT} = total pressure out

by isentropic relations

$$\frac{T_{OUT_s}}{T_{IN}} = \left(\frac{P_{OUT_s}}{P_{IN}} \right)^{\frac{\gamma-1}{\gamma}} = \left(\frac{P_{OUT}}{P_{IN}} \right)^{\frac{\gamma-1}{\gamma}} = PR^{\frac{\gamma-1}{\gamma}} \tag{5.7}$$

Substituting into 5.6 yields

$$\eta = \frac{C_p T_{IN} \left(PR^{\frac{\gamma-1}{\gamma}} - 1 \right)}{\tau \omega} \tag{5.8}$$

For low speed machines with small pressure rises

$$PR^{\frac{\gamma-1}{\gamma}} - 1 = \left[1 + \frac{P_{OUT} - P_{IN}}{P_{IN}}\right]^{\frac{\gamma-1}{\gamma}} - 1 = \left(1 + \frac{\Delta P_t}{P_{IN}}\right)^{\frac{\gamma-1}{\gamma}} - 1 \approx \frac{\gamma-1}{\gamma}\frac{\Delta P_t}{P_{IN}} \qquad (5.9)$$

which leads to

$$\eta = \frac{C_p T_{IN} \frac{\gamma-1}{\gamma} \frac{\Delta P_T}{P_{IN}}}{\tau \omega} \qquad (5.10)$$

Now we may form the ratio of treated wall efficiency to smooth wall efficiency as

$$\frac{\eta_{TR}}{\eta_{SM}} = \frac{\tau_{SM}}{\tau_{TR}} \frac{\Delta P_{TR}}{\Delta P_{SM}} \qquad (5.11)$$

where all the pressures are total pressures and the subscript sm stands for smooth wall and the subscript tr stands for treated wall. This equation shows that the efficiency reduction is dependent on the ratio of torques (power input) and the ratio of average pressure rises (useful power out). The equation is general and may be applied to either casing treatment or hub treatment. The ratio of torques can be regarded as representing a 'potential' for efficiency loss and the ratio of pressures determines whether this loss is incurred.

An estimation of the terms on the right hand side of equation 5.11 can be done for the present experiment by the use of Cheng's data. First, to estimate the torque ratio we may write

$$\frac{\tau_{SM}}{\tau_{TR}} = \frac{\tau_{ROTOR}}{\tau_{ROTOR} + \tau_{SLOTS}} = \frac{1}{1 + \frac{\tau_{SLOTS}}{\tau_{ROTOR}}} \qquad (5.12)$$

where

torque due to rotor

$$\tau_{ROTOR} = \int_{\text{TOTAL MASS FLOW}} \Delta U_\theta \, r \, dm \tag{5.13}$$

torque due to slots

$$\tau_{SLOTS} = \int_{\text{SLOT MASS FLOW}} \Delta U_\theta \, r \, dm \tag{5.14}$$

The torque on the rotor is the same for both cases. In the present experiment the mass flow in the slots was estimated, using the velocities from the hotwire data. It was found that the slot flow was 5% of the total flow. Using this and the data of Cheng [4] the integrals in equations 5.13 and 5.14 can be calculated. Using data at a flow coefficient of .35 (which is the same operating point where velocity data was taken) it was found

$$\frac{\tau_{SM}}{\tau_{TR}} = .64 \tag{5.15}$$

This value is quite low; and the reason for this is that the rotor is very lightly loaded. Similarly, the average pressure rise ratio was found from Cheng's data to be

$$\frac{\Delta P_{TR}}{\Delta P_{SM}} = 1.42 \tag{5.16}$$

Substituting 5.15 and 5.16 into 5.11 yields

$$\frac{\eta_{TR}}{\eta_{SM}} = .90 \tag{5.17}$$

This shows a reduction in efficiency of 10% in the treated build. This is consistent with data taken by Prince et.al [10] where they found an 8.6% reduction in efficiency.

The above discussions indicate that the efficiency of a

treated compressor stage is not only determined by the efficiency of the blade rows but also the by the efficiency with which the work done, or induced, by the treatment is converted into useful pressure rise. Since the overall stage efficiency is seen to drop when treatment is applied it is clear that the current treatment configurations are not doing work efficiently. Furthermore, it appears likely that the poor 'treatment efficiency' is associated with the strong flow injection, or jet, that is characteristic of the axial skewed slot. As mentioned earlier, the jet exits the slots with high velocity and total pressure (due to the work done on the slot flow) and enters normal to the mean flow. This certainly is accompanied by mixing losses thus lowering the efficiency.

In order to improve treated stage efficiency two things are needed. First, to reduce the 'potential' for efficiency loss, the torque ratio should be increased. This can be done by designing the slots to do less work, or equivalently, less change in tangential velocity. Also the mass flow in the slots should be kept as low as possible. Second, in order to improve the 'treatment efficiency', the jet should be reinjected smoothly into the flow, hence reducing mixing losses.

CHAPTER 6
CONCLUSIONS AND RECOMMENDATIONS

6.1 SUMMARY AND CONCLUSIONS

To better understand the operation of compressor casing treatment a detailed investigation of the flow phenomena occurring with one of the more effective treatment geometries, the axial skewed slot, has been carried out. The experiment utilized a rotating hub treatment (axial skewed slots) moving underneath the tips of a cantilevered stator blade row.

The application of this hub treatment resulted in substantial improvement in stall margin and peak pressure rise compared to the same stator with a smooth hub.

Radial traverses with a hotwire just inside the blade passage near the trailing edge have provided evidence that the stall encountered in the smooth build is a wall stall. As has been hypothesized previously it appears that this condition is crucial to the effectiveness of tip treatment.

The three dimensional unsteady velocity field has also been examined via hotwire anemometry. In this the time averaged flow field was found to be most significant. Results with the smooth hub showed that the region of high blockage, is in the center of the blade passage emanating from the hub endwall and not associated with either blade surface.

In the treated build two important phenomena were found. The more striking is the strong flow injection or jet that

appears near the leading edge. Less obvious, but far more important, is a region of fluid removal near the trailing edge.

It is seen that, when hub treatment is applied, blockage that occurs is completely removed. The removal acts directly on the region where blockage occurs and in fact the strongest removal occurs in the same location where (with the smooth build) the blockage would be the greatest.

The jet, on the other hand, never approaches the region of blockage and therefore cannot act directly on the blockage. It is thus proposed that, since it is the blockage that leads to stall, it is the blockage removal, which acts directly on the blockage, that is responsible for the effectiveness of the slots in improving stall margin.

It is arguable that any fluid that reaches the region of removal must first pass over the jet and this may have some effect. No quantitative evidence is available on this point. However, the measurements do show that jet is not oriented to impart momentum to the incoming boundary layer. In fact, the data shows that the jet and the incoming flow are are almost perpendicular. Therefore, though qualitative, the arguments presented are felt to provide strong evidence that it is not the jet interaction that is important but rather the subsequent removal.

High response measurements of the unsteady velocity field were also made. These showed that the flow in the smooth wall

build was essentially steady in the absolute reference frame, with only small remnants of the rotor blade wakes visible. For the treated build it was found that most of the velocity field could be regarded as steady, except for a small region near the hub where the individual jets exit from their respective slots. In this region a large unsteadiness was found. Most notably it was seen that the axial component of velocity was varying from 'normal' values near Cx to substantially negative, or reversed, values. It does not appear that this type of injection near the leading edge is beneficial to the incoming boundary layer.

Lastly, A discussion concerning the connection between the jet and compressor efficiency has been presented. A simple equation was derived which showed the efficiency loss was due to the (inefficient) work done by the slots. The increased torque associated with the treated case represents a 'potential' for efficiency loss while the ratio of average pressure rises determines whether the loss in efficiency was incurred.

If one accepts the above arguments, the conclusion is that the jet is merely a consequence of the removal and serves no directly useful purpose. This is an important result because it allows researchers to turn there attention to eliminating or making positive use of the jet. If the detrimental effects of the jet (e.g. mixing losses) can be eliminated while retaining the positive effect of the removal, (improved stall margin) then a significant advance would be made.

6.2 RECOMMENDATIONS FOR FUTURE WORK

We separate the recommendations into two parts. Those which have generic application and those which pertain to the present experimental set up. We discuss the former first. From the conclusions of the present work it seems extremely useful to devise an experiment that to investigate the effects of injection and removal separately on the stall margin. It is important here to carefully mimic the conditions that occur in the treated build while allowing for variation in the injection and removal rates.

As a complement to the above experiment, an analytical calculation that verifies the conclusions made in this report could be done. To do this it is suggested that the unsteady effects be neglected. Since we are essentially interested in the endwall region perhaps a three dimensional turbulent boundary layer calculation with injection and removal might be manageable.

There is a vast range of research possibilities that could explore the problem of improving the efficiency of a treated compressor stage. A treatment could be designed that retained the removal characteristic, which is what yields improved stall margin, but that that did less work on the flow, thus reducing the potential for efficiency loss. Furthermore this new treatment should reintroduce the jet in a smooth manner thus improving the 'treatment efficiency'.

In terms of the present experimental set up there are several modifications to be made. The most important of these is the installation of a torque meter, this will be useful and interesting no matter what direction future experiments take. Furthermore, it would take relatively few modifications to make the present set up capable of doing the injection/removal experiment discussed above. If this experiment is done it would not only confirm the hypotheses proposed by the present work but also it would also show how much slot mass flow is necessary to improve the stall margin.

REFERENCES

1. Smith, G.D.J., 'Casing Treatment in Axial Compressors', Doctoral thesis, Engineering Department, University of Cambridge, April 1980.

2. Greitzer, E.M., Nikkanen, J.P., Haddad, D.E., Mazzawy, R.S., and Joslyn, H.D., 'A Fundamental Criterion for the Application of Rotor Casing Treatment', ASME Journal of Fluids Engineering, June 1979, vol. 101.

3. Cheng, P., Prell, M.E., Greitzer, E.M., Tan, C.S., 'Effects of Compressor Hub Treatment on Stator Stall Margin and Performance', AIAA-83-1352, June 1983.

4. Takata, H., and Tsukuda, Y., 'Stall Margin Improvement by Casing Treatment - Its Mechanism and Effectiveness', ASME Paper 76-GT-A, February 1976.

5. Fujita, H., and Takata, H., 'A Study on Configurations of Casing Treatment for Axial Flow Compressors', JSME, Vol. 27, August 1984.

6. Cheng, P., 'Effects of Compressor Hub Treatment on Stator Stall And Pressure Rise', MIT, GTLPDL Report No. 167, September 1982.

7. Koch, C.C., 'Stalling Pressure Rise Capability of Axial Flow Compressor Stages', ASME Paper No. 81-GT-3, May 1981.

8. Hearsey, R.M., A Revised Computer Program for Axial Compressor Designs, vols. 1 and 2, ARL-TR-75-001, Aerospace Research Laboratory, Wright Patterson Air Force Base, Ohio, 1976.

9. Prell, M.E., 'An Experimental Investigation of Stator Hub Treatment in an Axial Flow Compressor', MIT, GTLPDL Report No. 161, July 1981.

10. Wagner, J.H., and Okishi, T.H., 'Analysis of Multistage, Axial Flow Turbomachine Wake Production, Transport, and Interaction', Department of Mechanical Engineering, Iowa State University, ISU- ERI-AMES-78173, December 1977.

11. Schmidt, D.P., and Okishi, T.H., 'Multistage Axial-flow Turbomachine Wake Production, Transport and Interaction.' AFOSR-TR-77-0720, November 1976.

12. Shin, H.W., Personal Communication (Sept. 1984)

13. Prince, D.C., Jr., Wisler, D.C., and Hilvers, D.E.,'Study of Casing Treatment Stall Margin Improvement Phenomena', NASA CR- 134552, March 1974.

TYPICAL COMPRESSOR CHARACTERISTIC

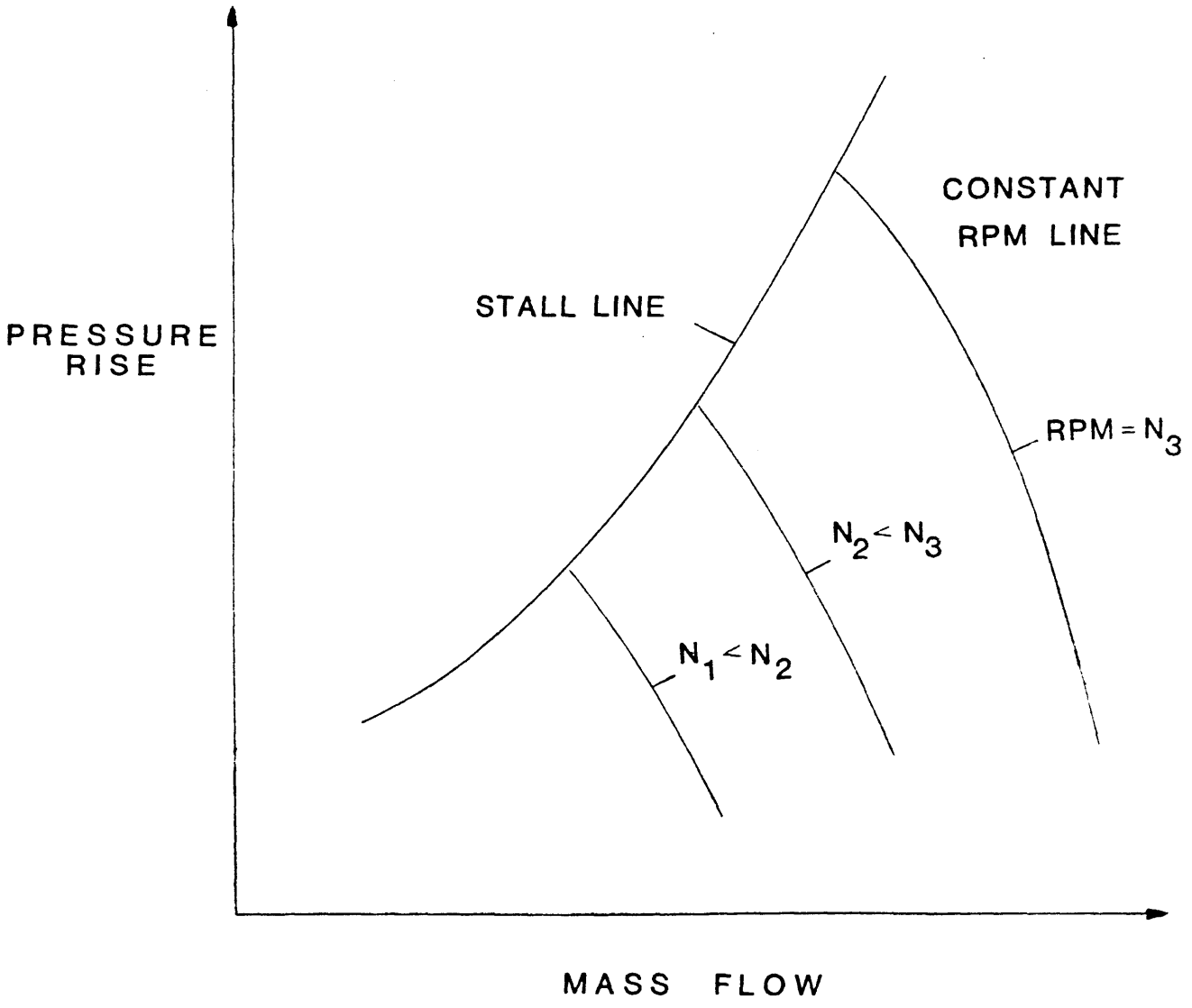

Fig 1.1 Generic compressor map

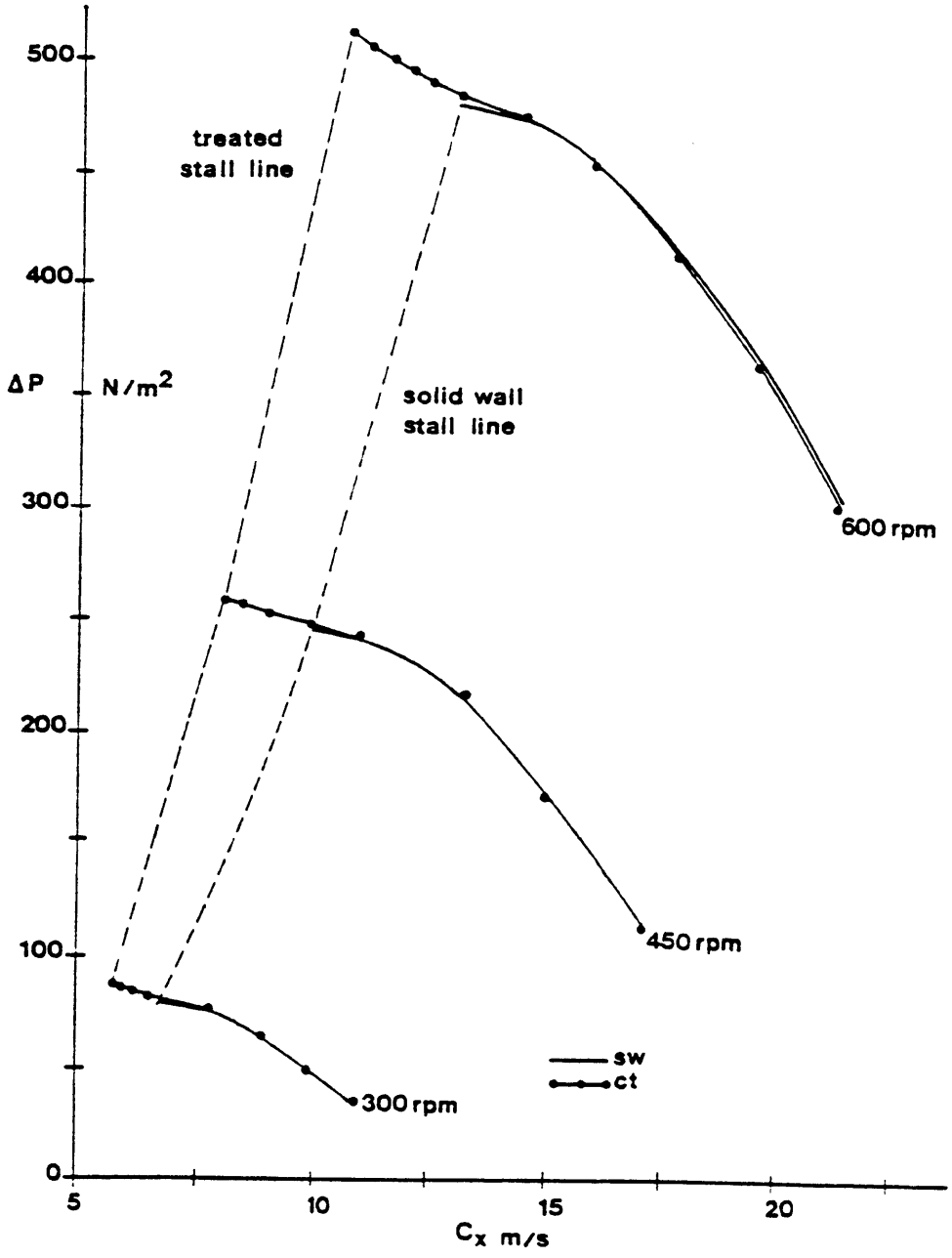

Fig. 1.2 Static pressure rise characteristics for solid wall and treated wall (Smith) [1]

TYPES OF COMPRESSOR STALL

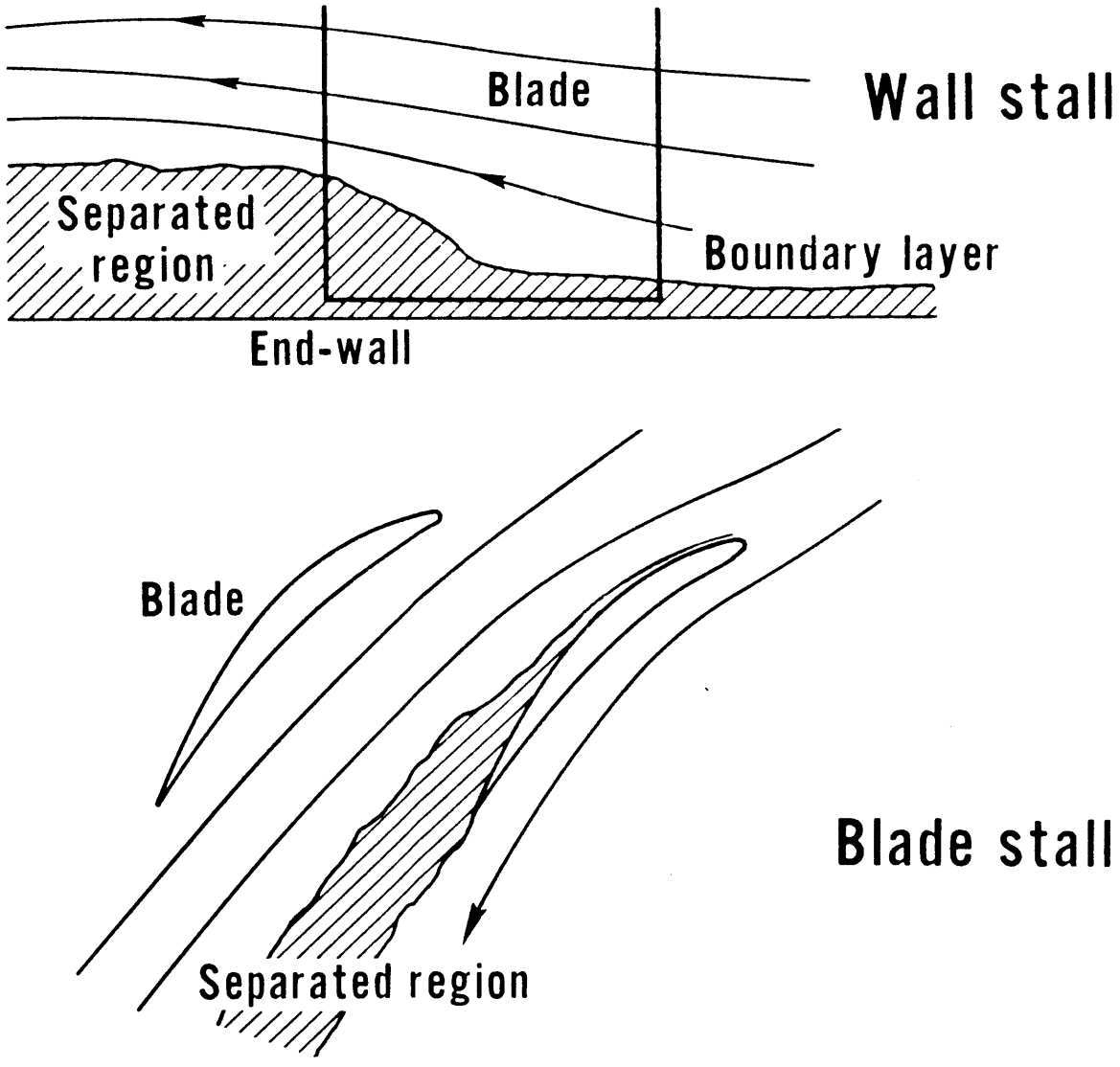

Fig 1.3 Blade stall and wall stall

TAKATA'S RESULTS [5]

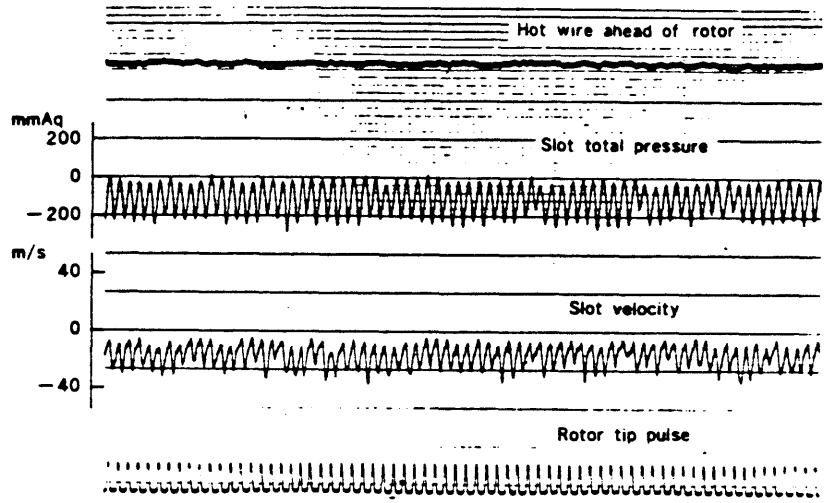

AXIAL SKEWED SLOT

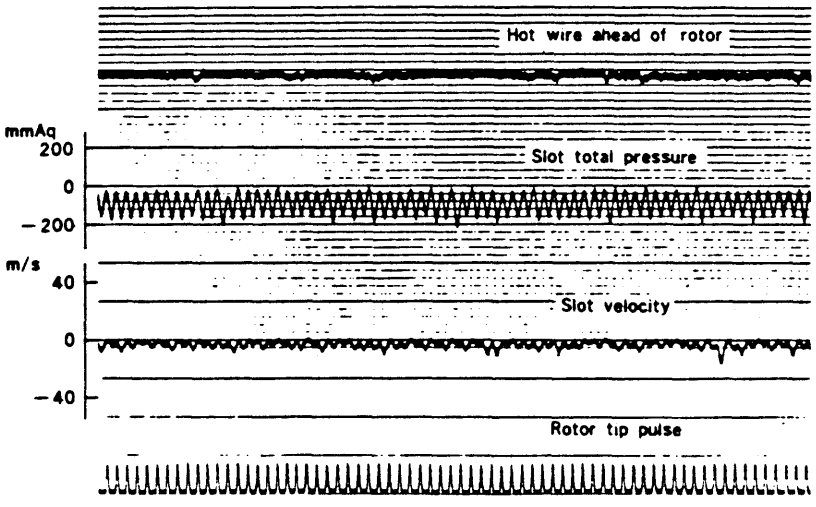

REVERSED AXIAL SKEWED SLOT

Fig 1.4 Takata's results

GRID LOCATIONS

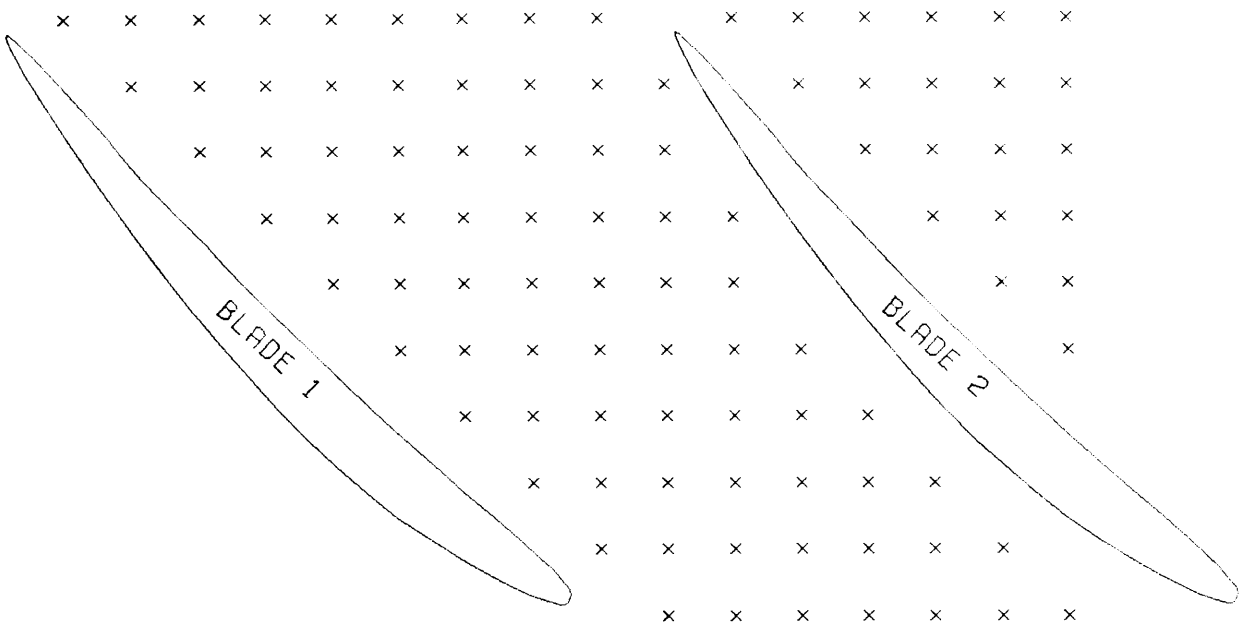

Fig. 2.1 Grid locations

TOP VIEW OF POSITIONING SYSTEM

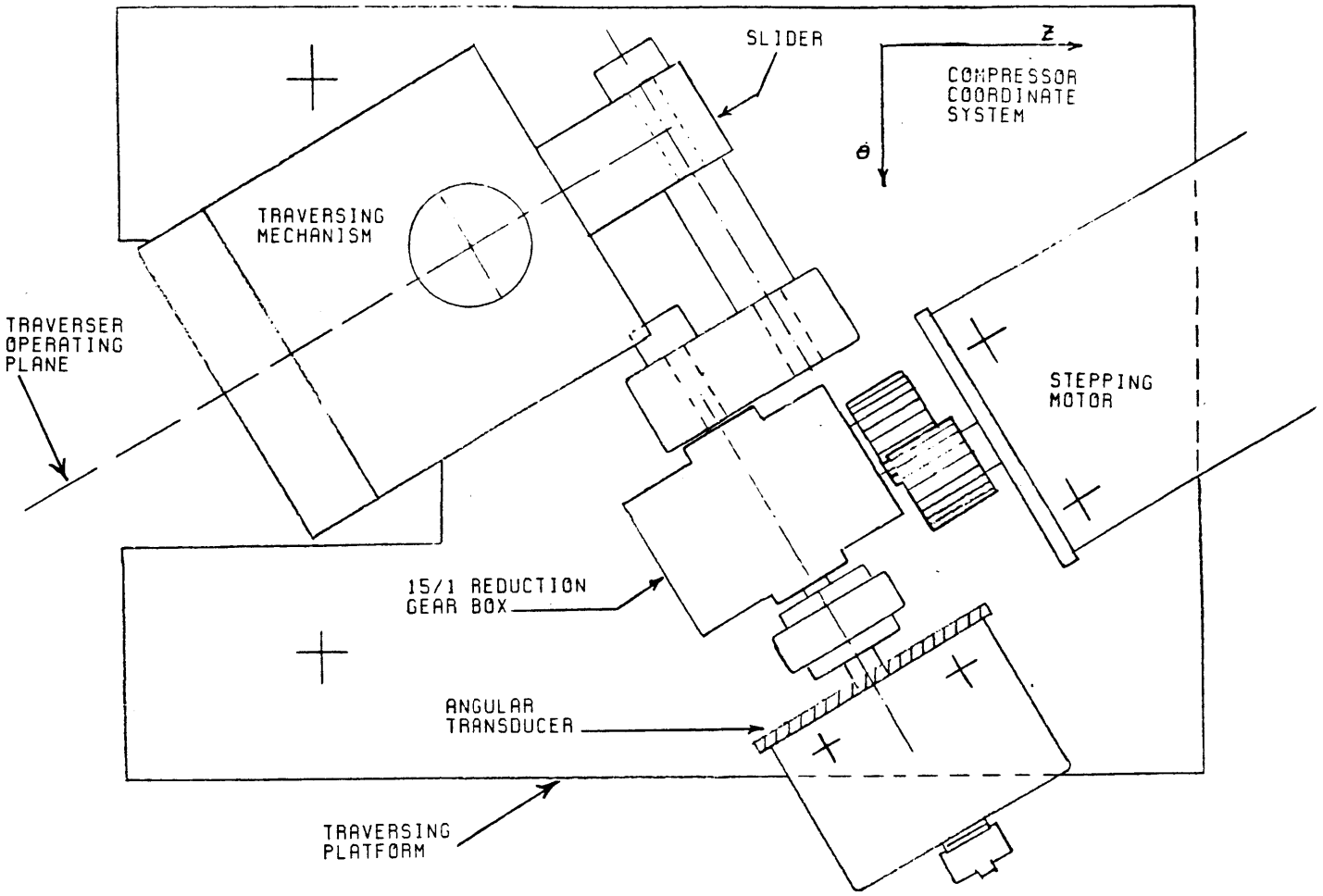

Fig. 2.2 Top view of positioning system

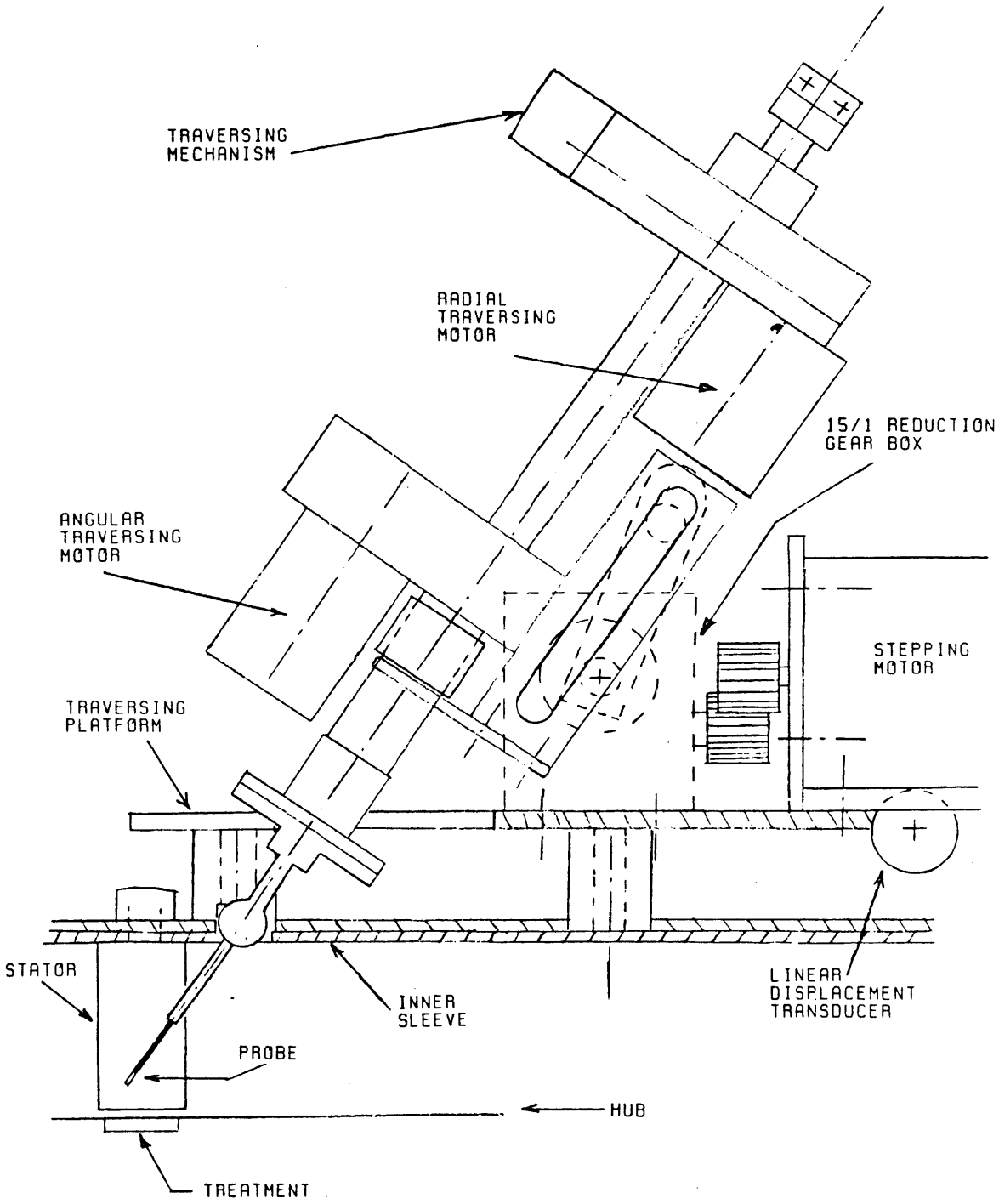

Fig. 2.3 Side view of positioning system

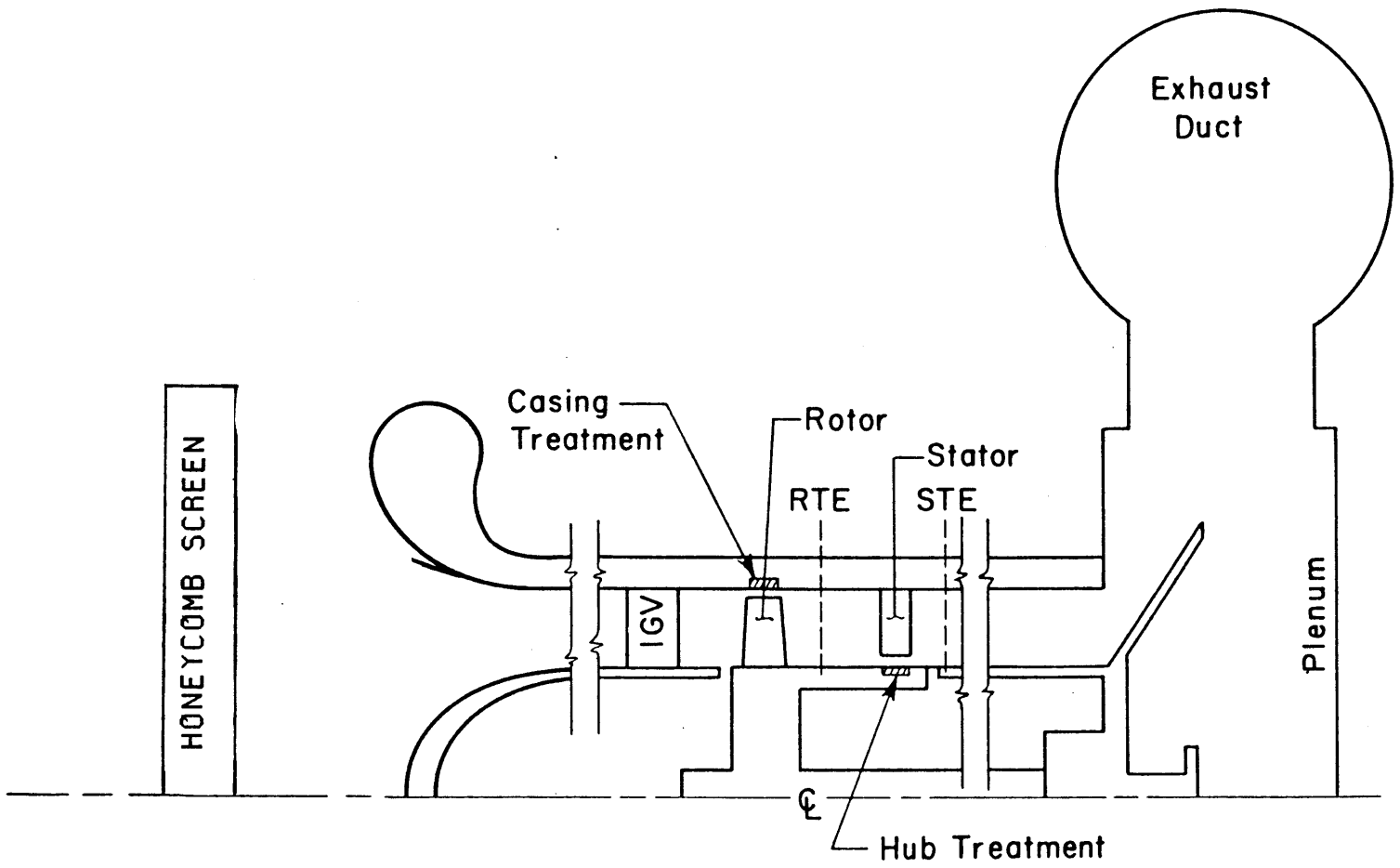

Fig. 3.1 Compressor schematic

TREATMENT GEOMETRY

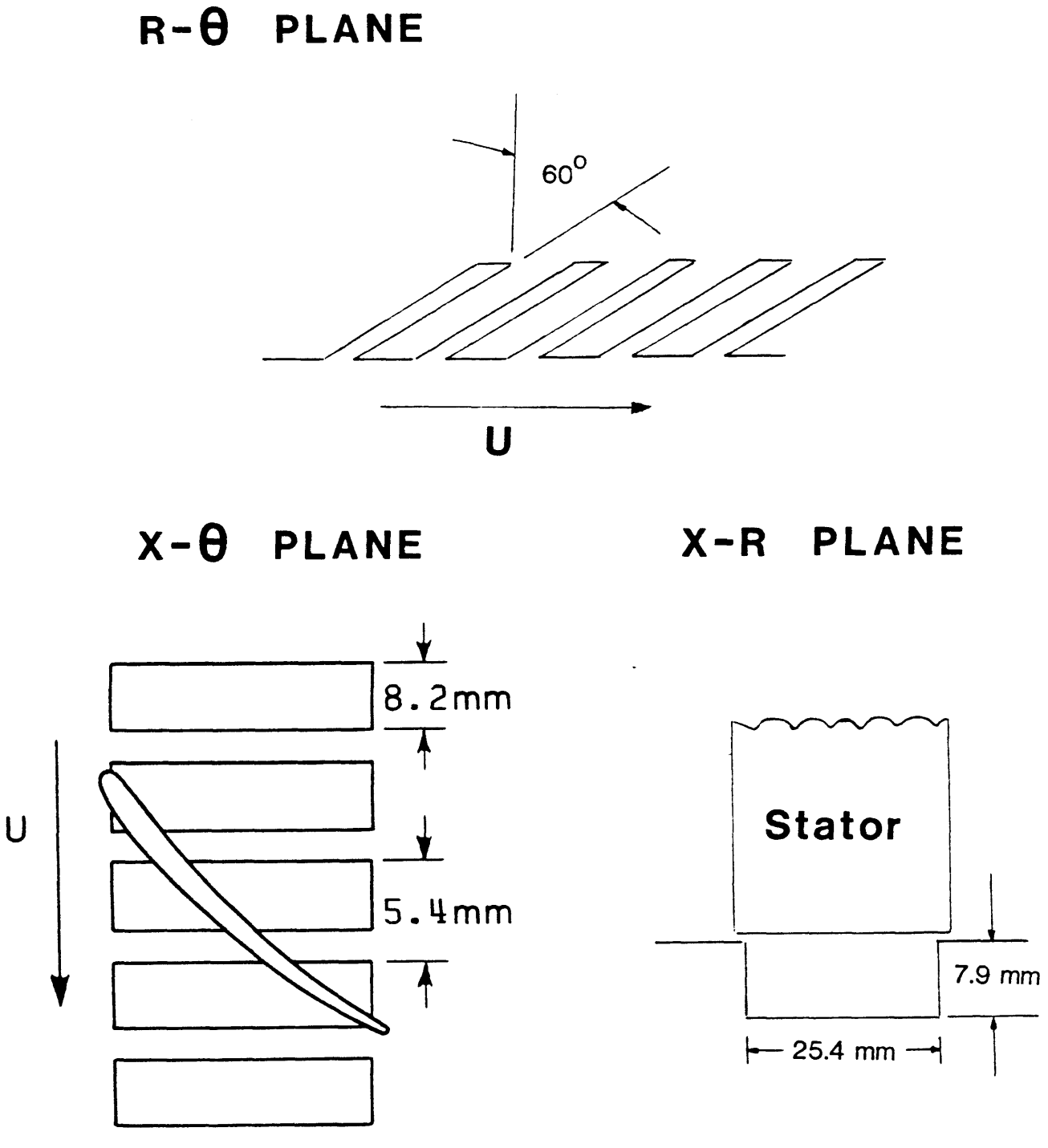

Fig. 3.2 Treatment geometry

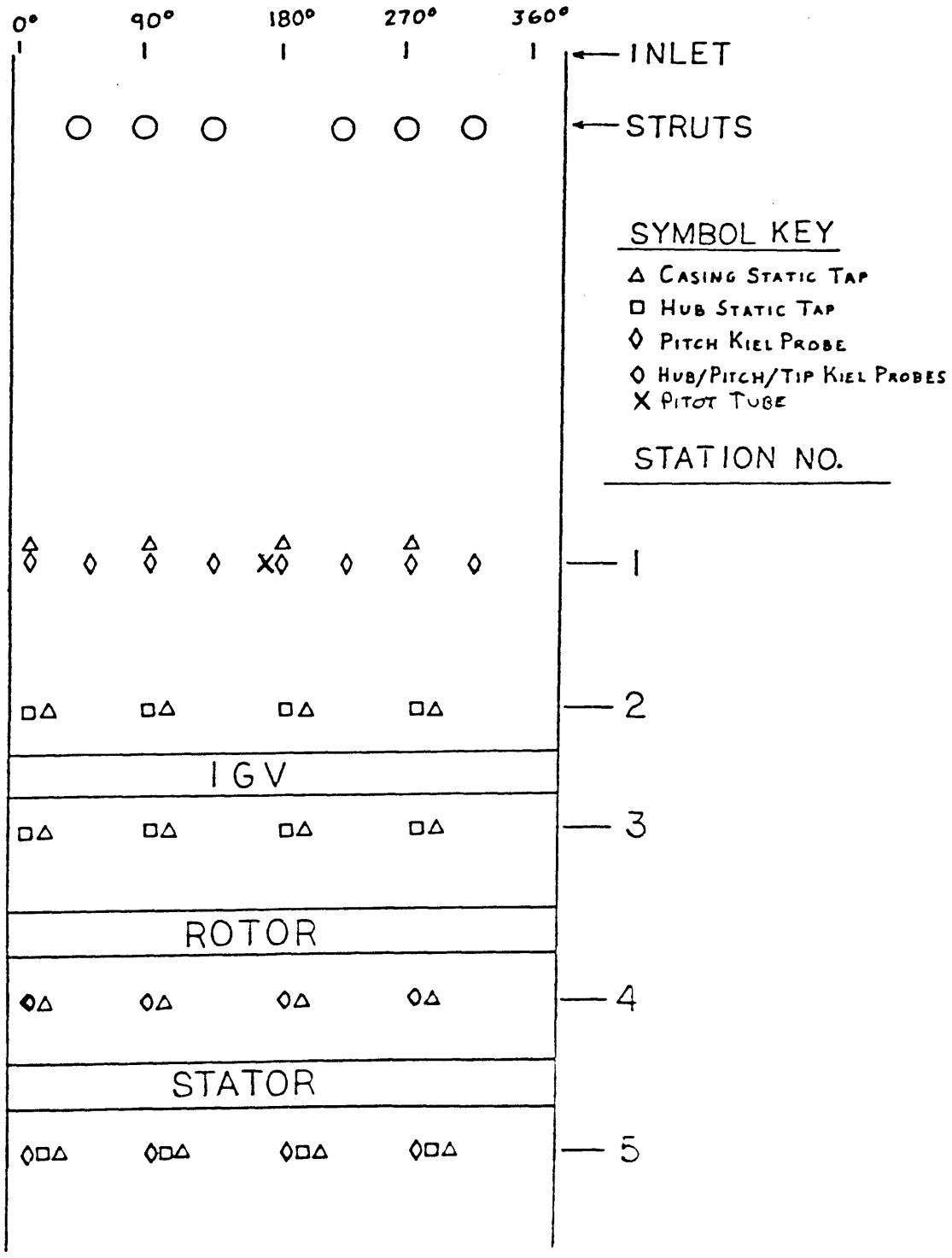

Fig. 3.3 Instrumentation schematic

PRESSURE TRANSDUCER CALIBRATION

DATE: 9 /3 /84

SERIAL NO.: C999

SLOPE (IN. H20/VOLT):	27.6690
Y-INTERCEPT (IN. H20):	-0.0353
SENSITIVITY (MV/IN. H20):	36.1
STD DEV (IN. H20):	0.0223

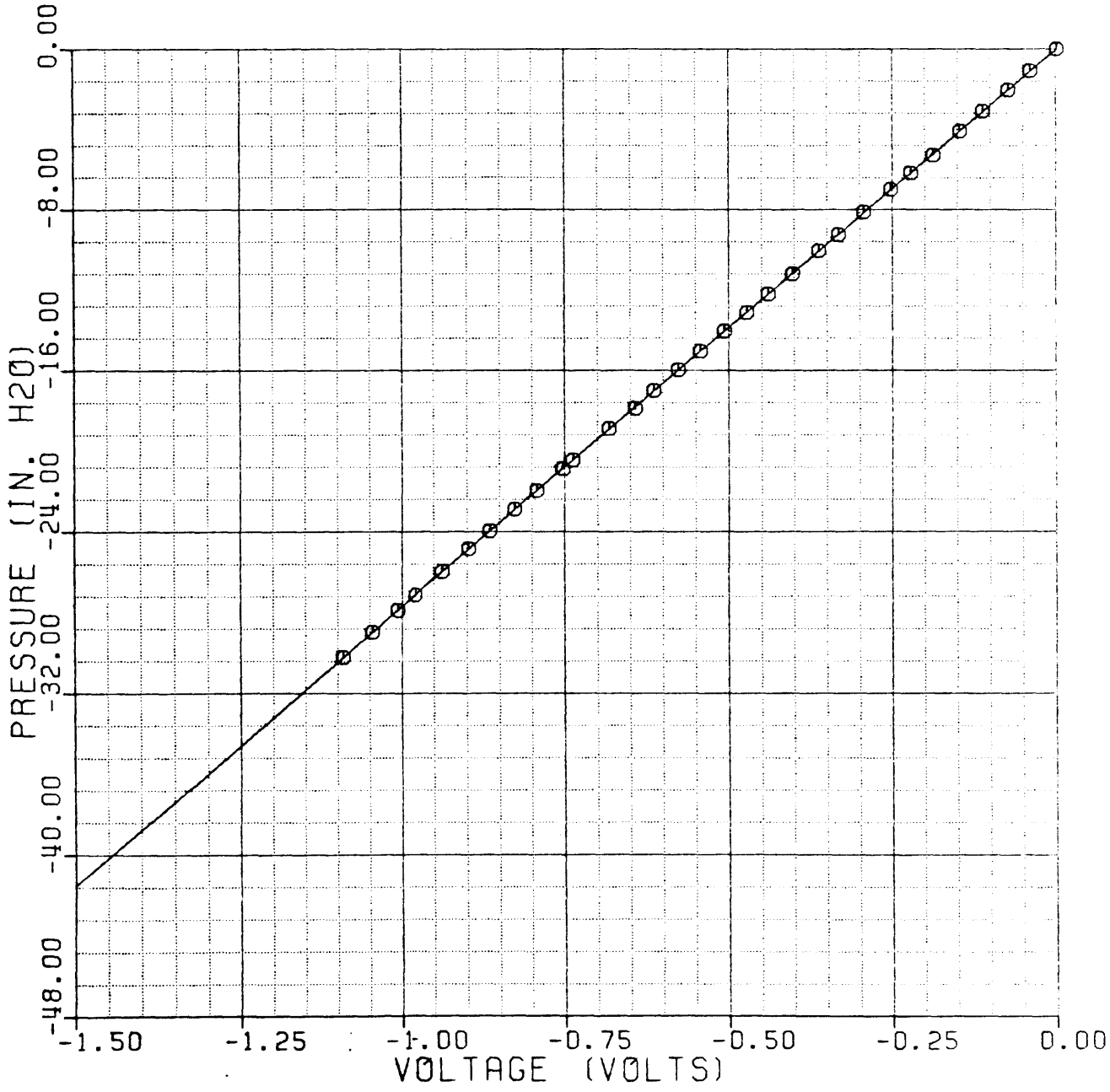

Fig. 3.4 Scanivalve calibration

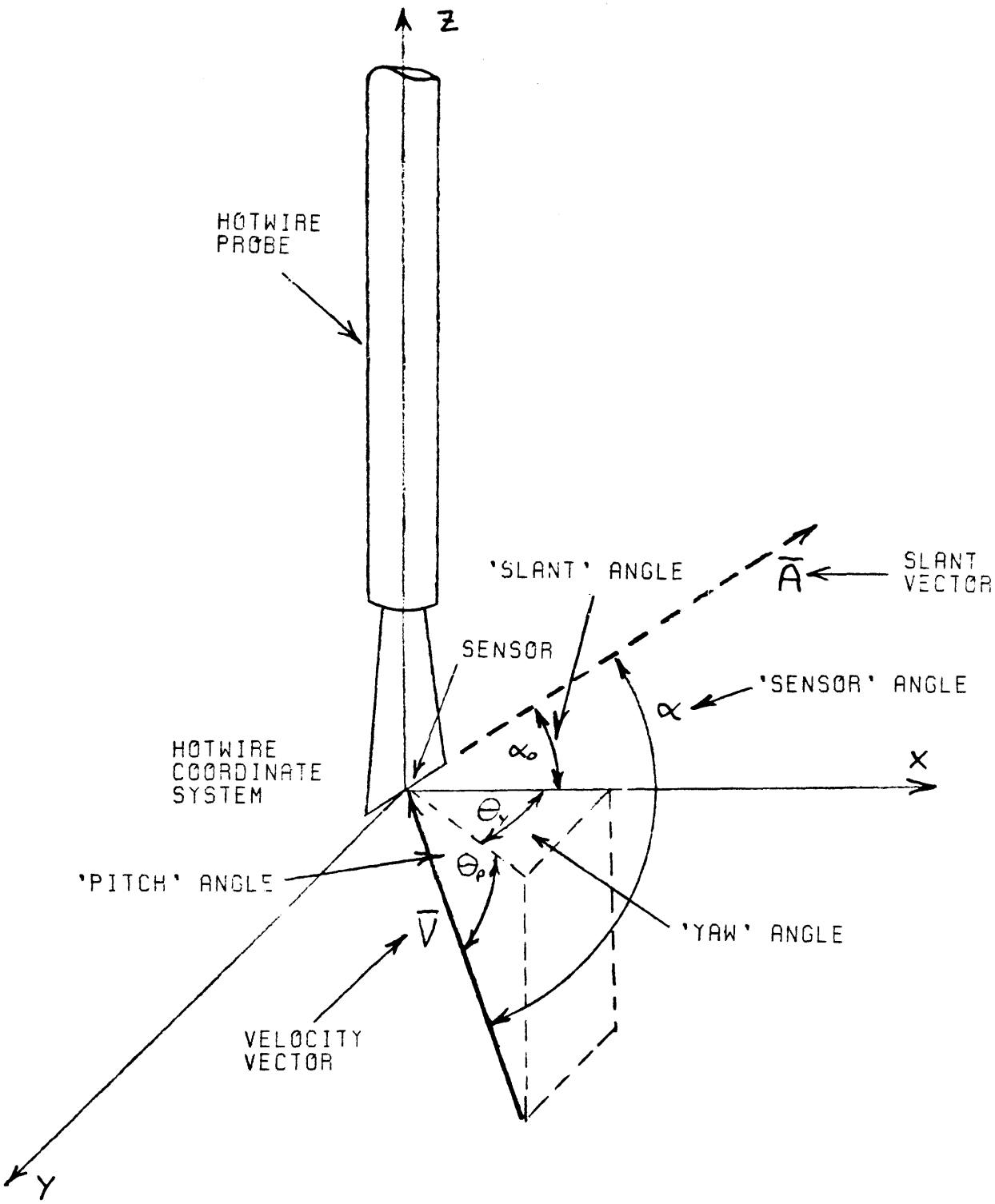

Fig. 3.5 Probe geometry

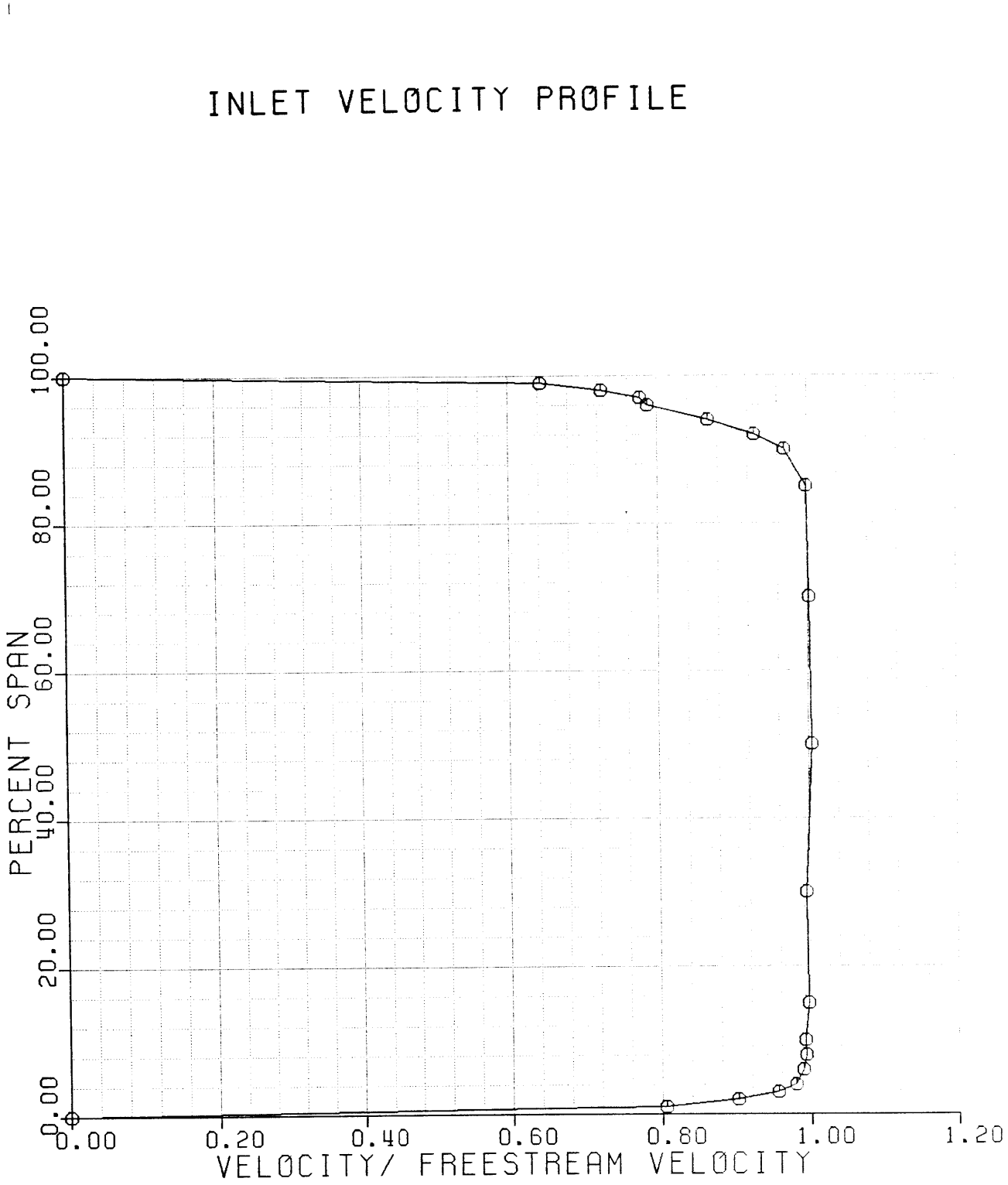

Fig. 4.1 Velocity profile

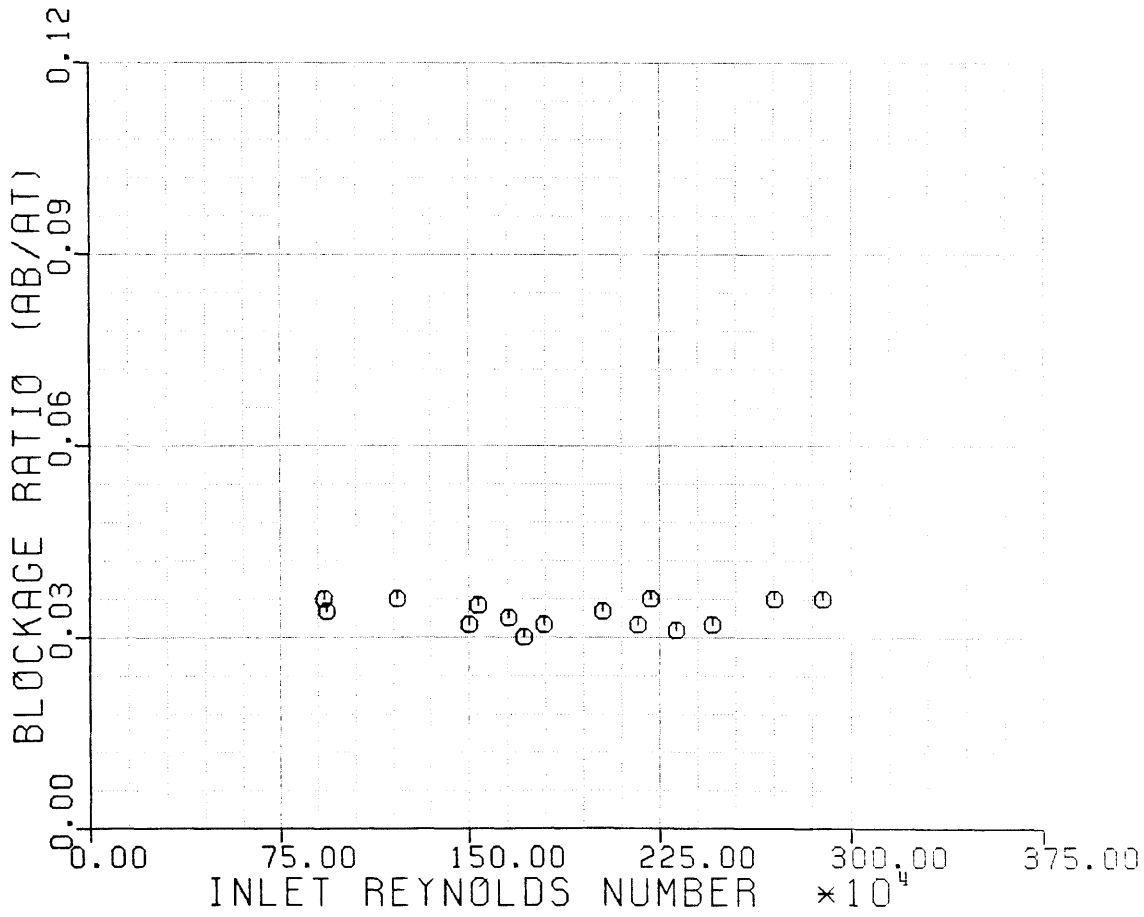

Fig. 4.2 Inlet blockage Vs. Reynolds no.

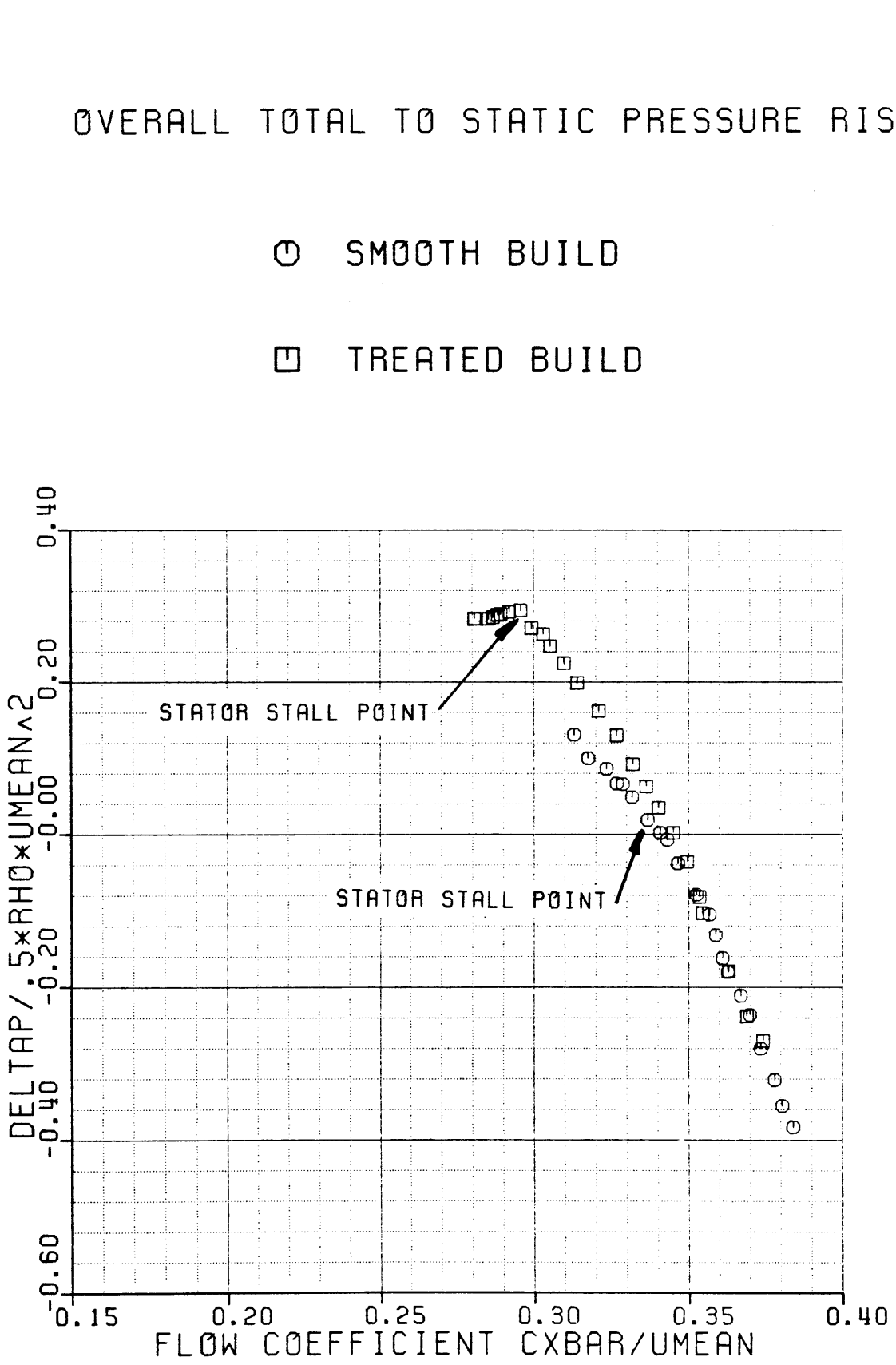

Fig. 4.3 Overall performance map

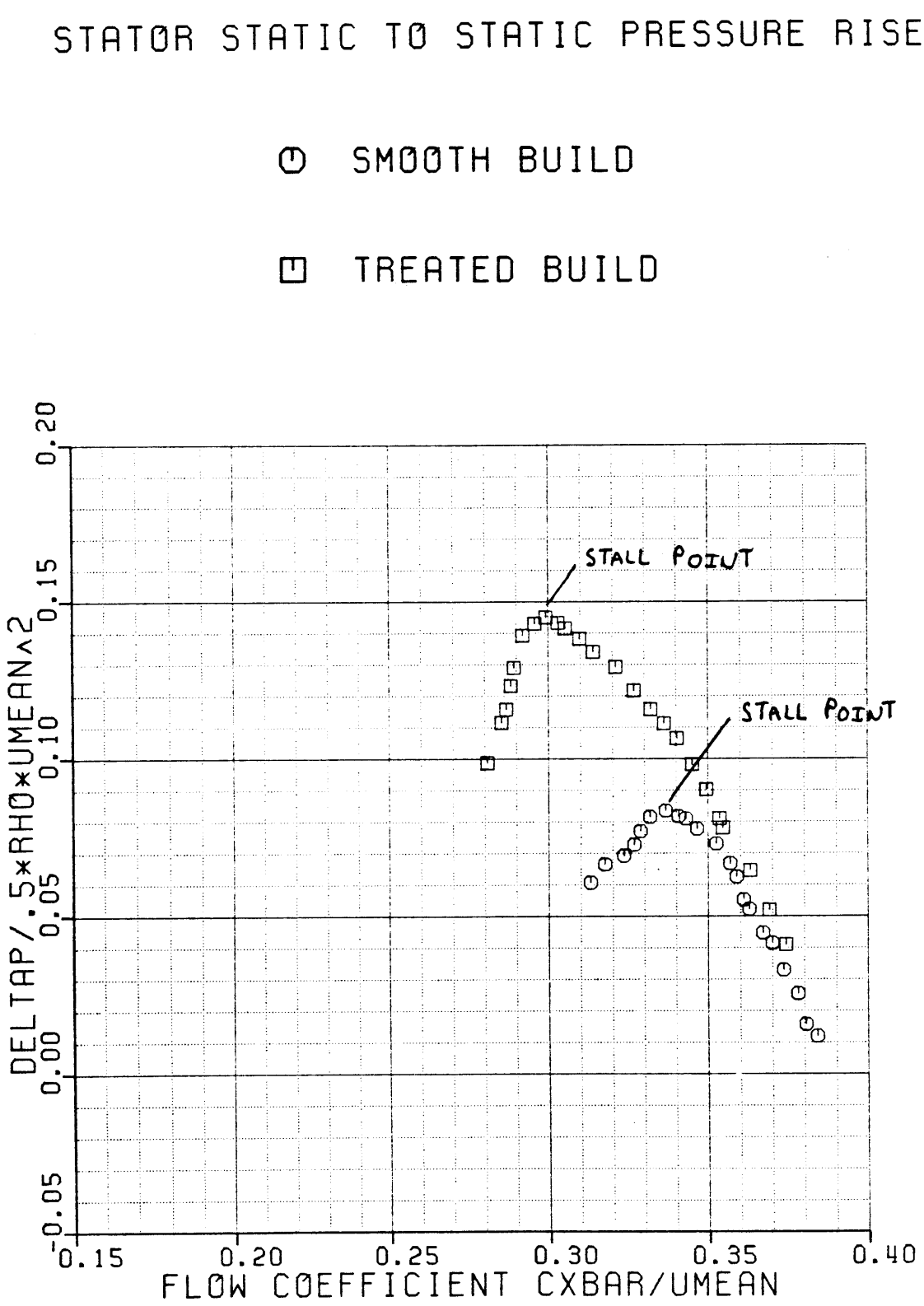

Fig. 4.4 Stator performance map

Φ=.330

Φ=.345

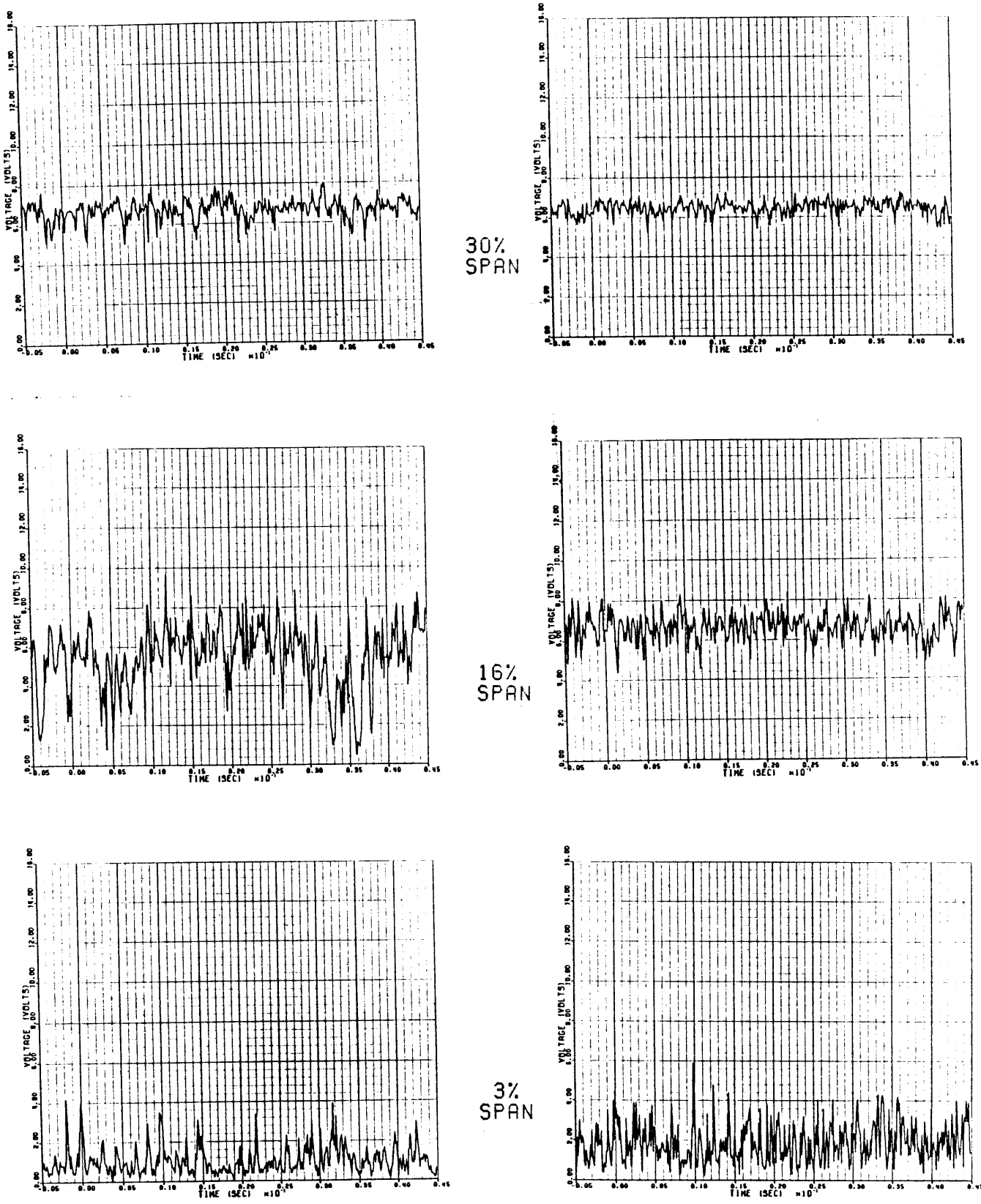

Fig. 4.5 Hotwire traces inside stator blade row

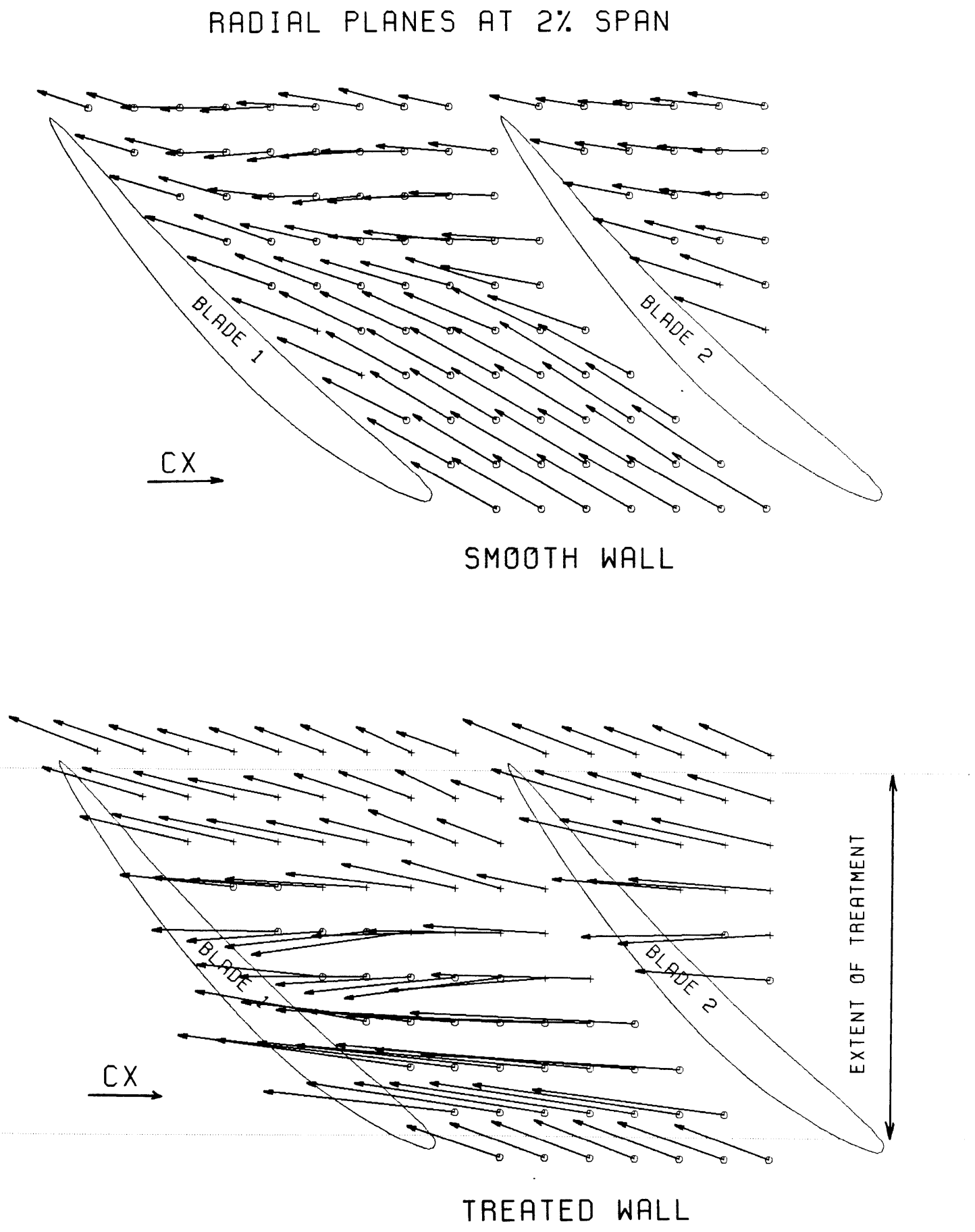

Fig. 4.6 Radial planes at 2% span

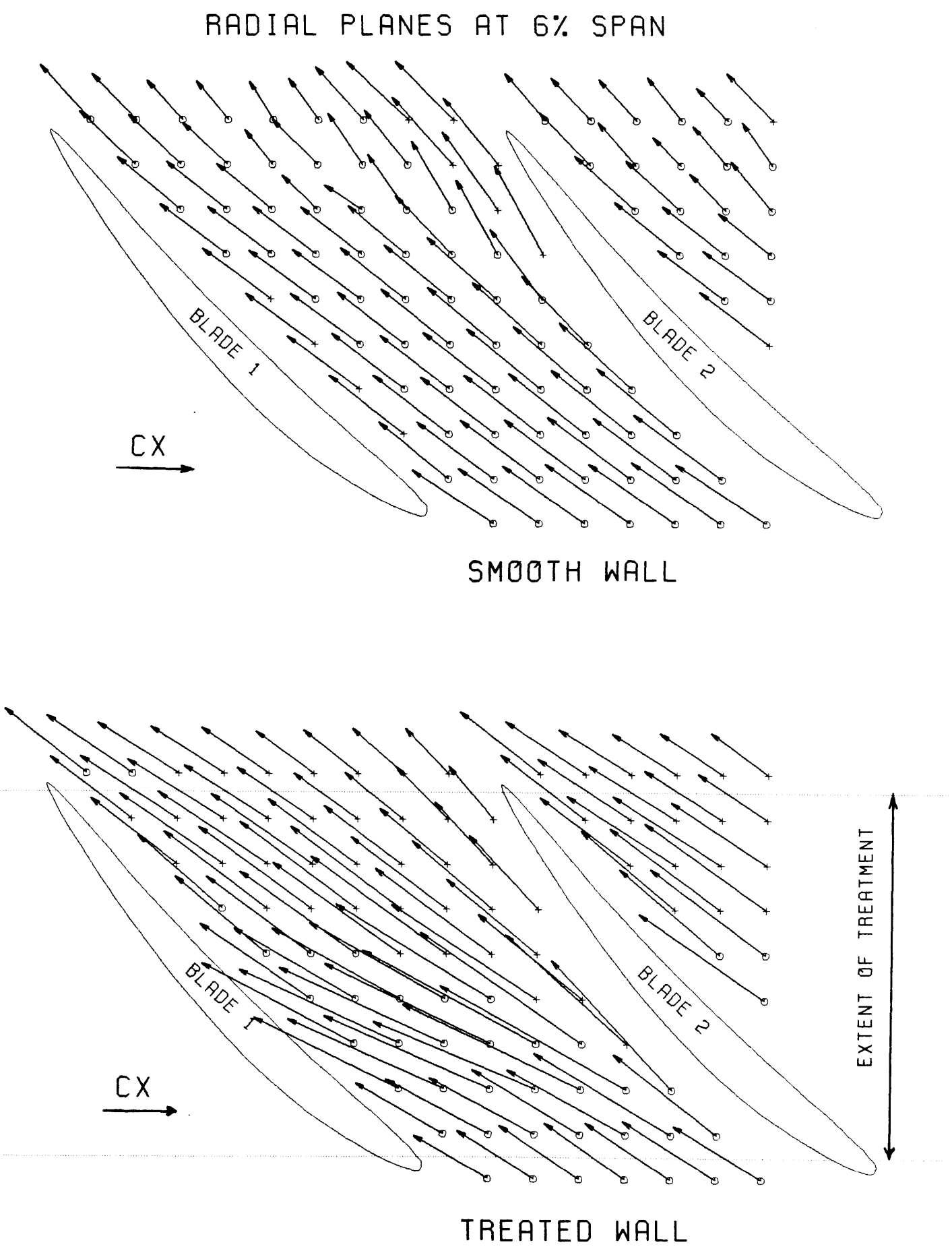

Fig. 4.7 Radial planes at 6% span

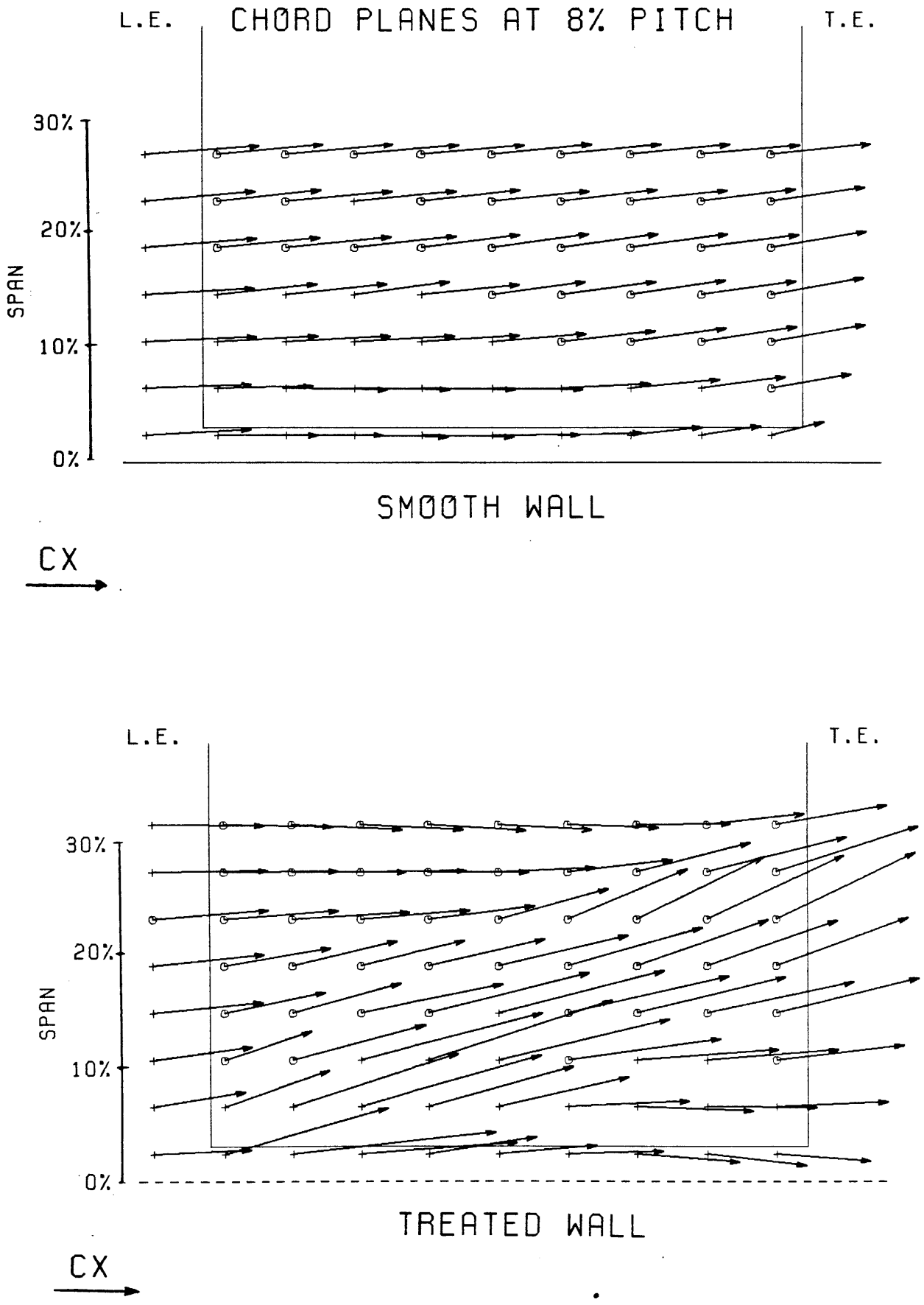

Fig. 4.8 Chordal planes at 8% pitch from pressure surface

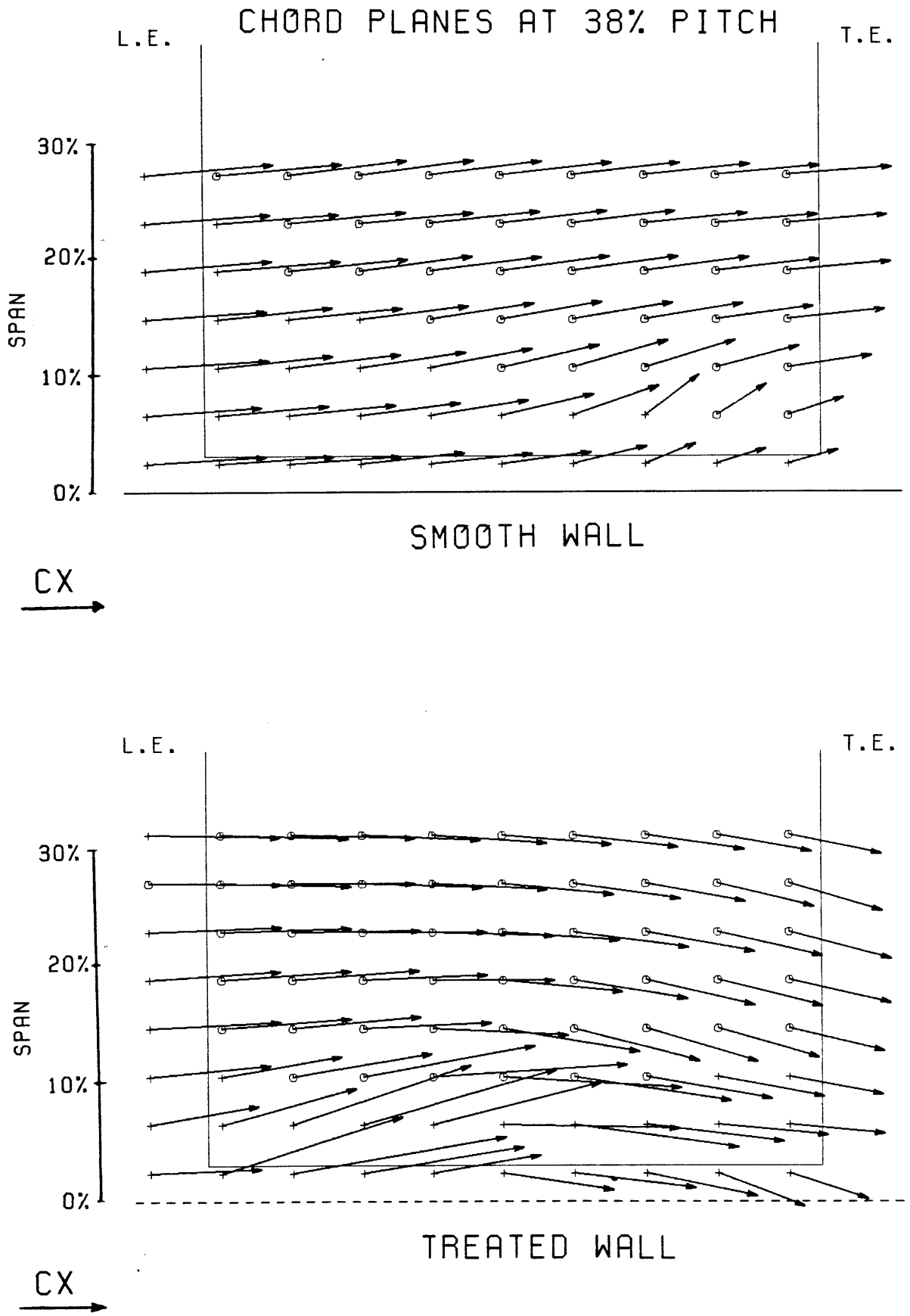

Fig. 4.9 Chordal planes at 38% pitch from pressure surface

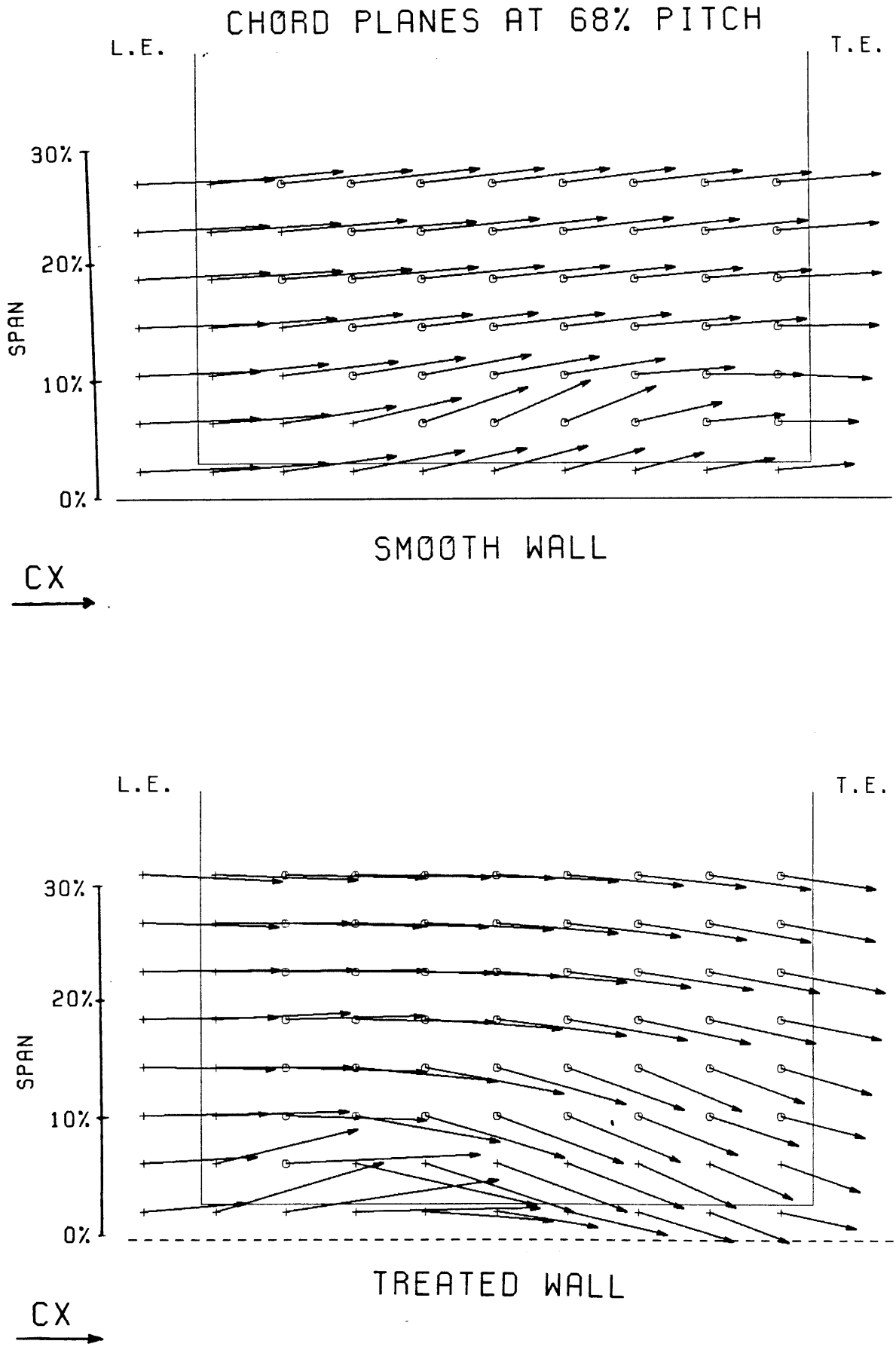

Fig. 4.10 Chordal planes at 68% pitch from pressure surface

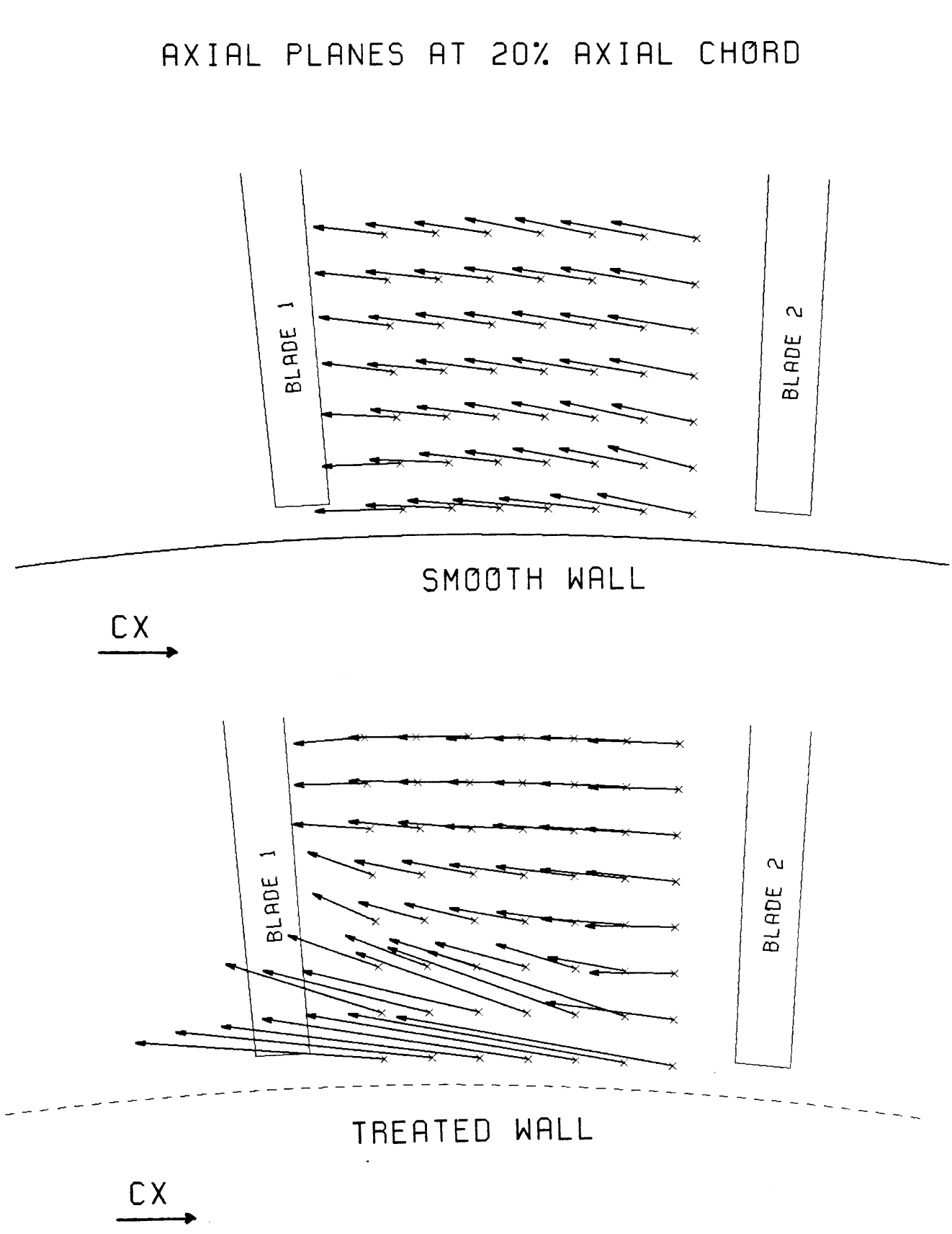

Fig. 4.11 Axial planes at 20% axial chord

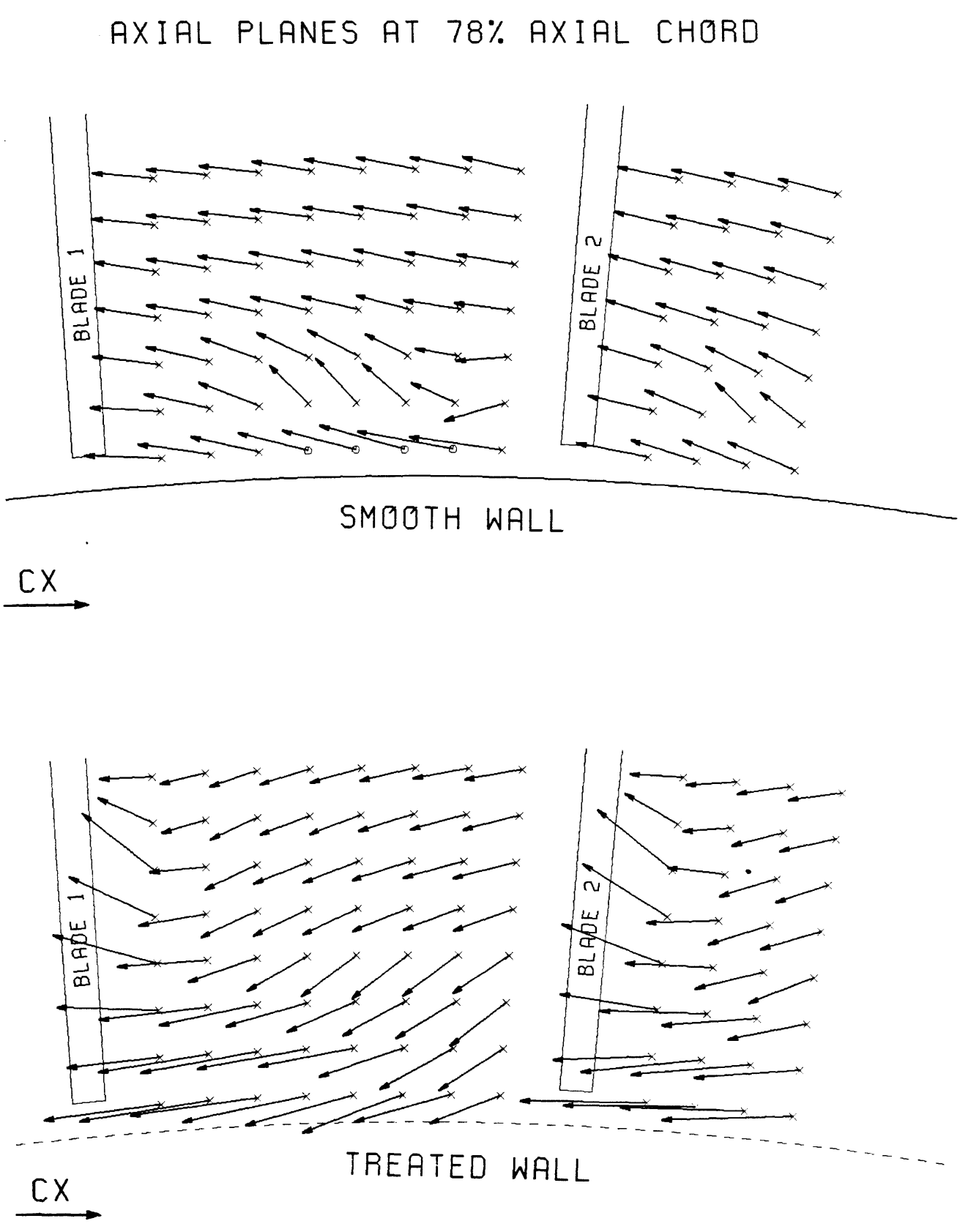

Fig. 4.12 Axial planes at 78% axial chord

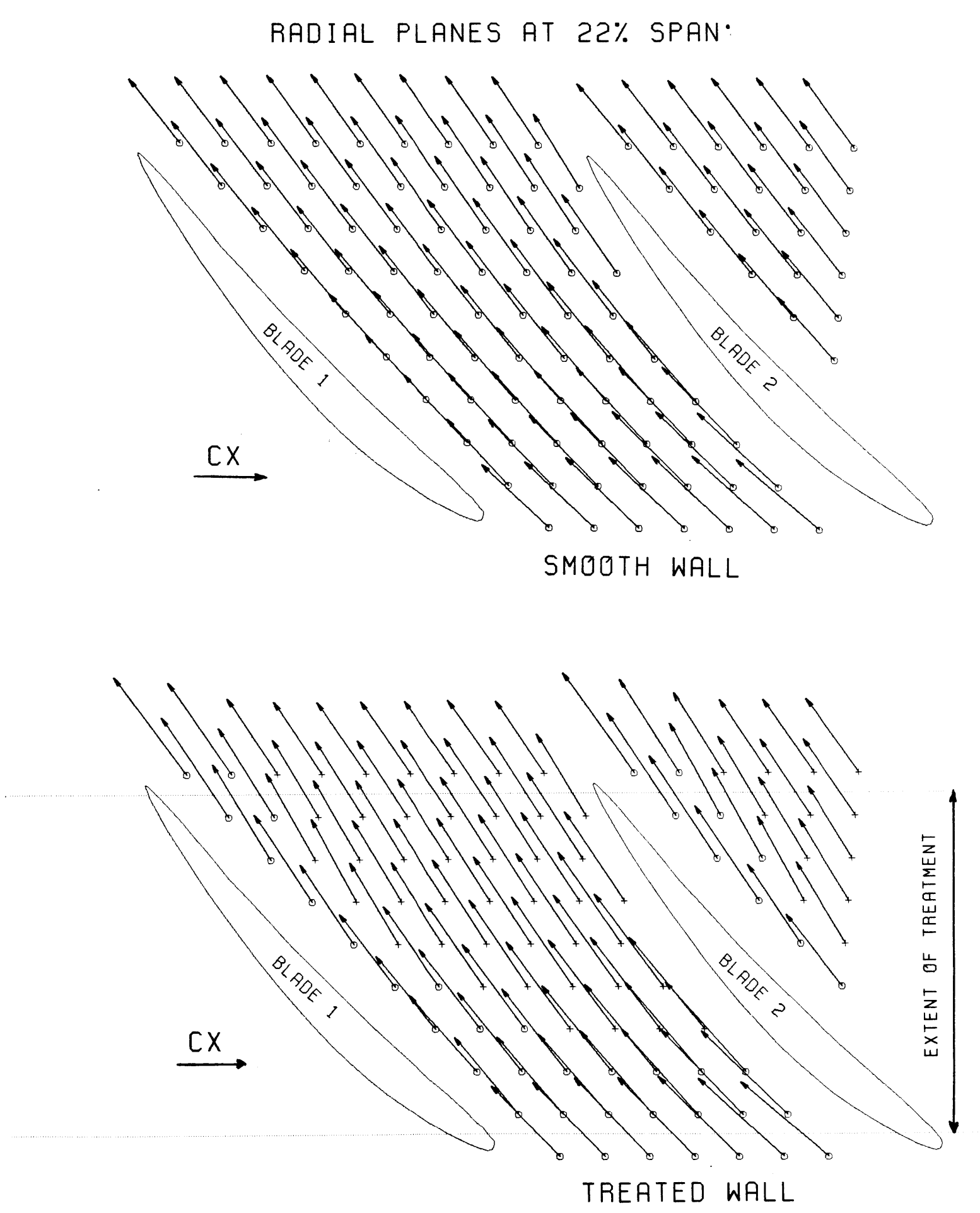

Fig. 4.13 Radial planes at 22% span

GREITZER'S RESULTS

ROTOR EXIT TOTAL PRESSURE LOSS CONTOURS NEAR STALL

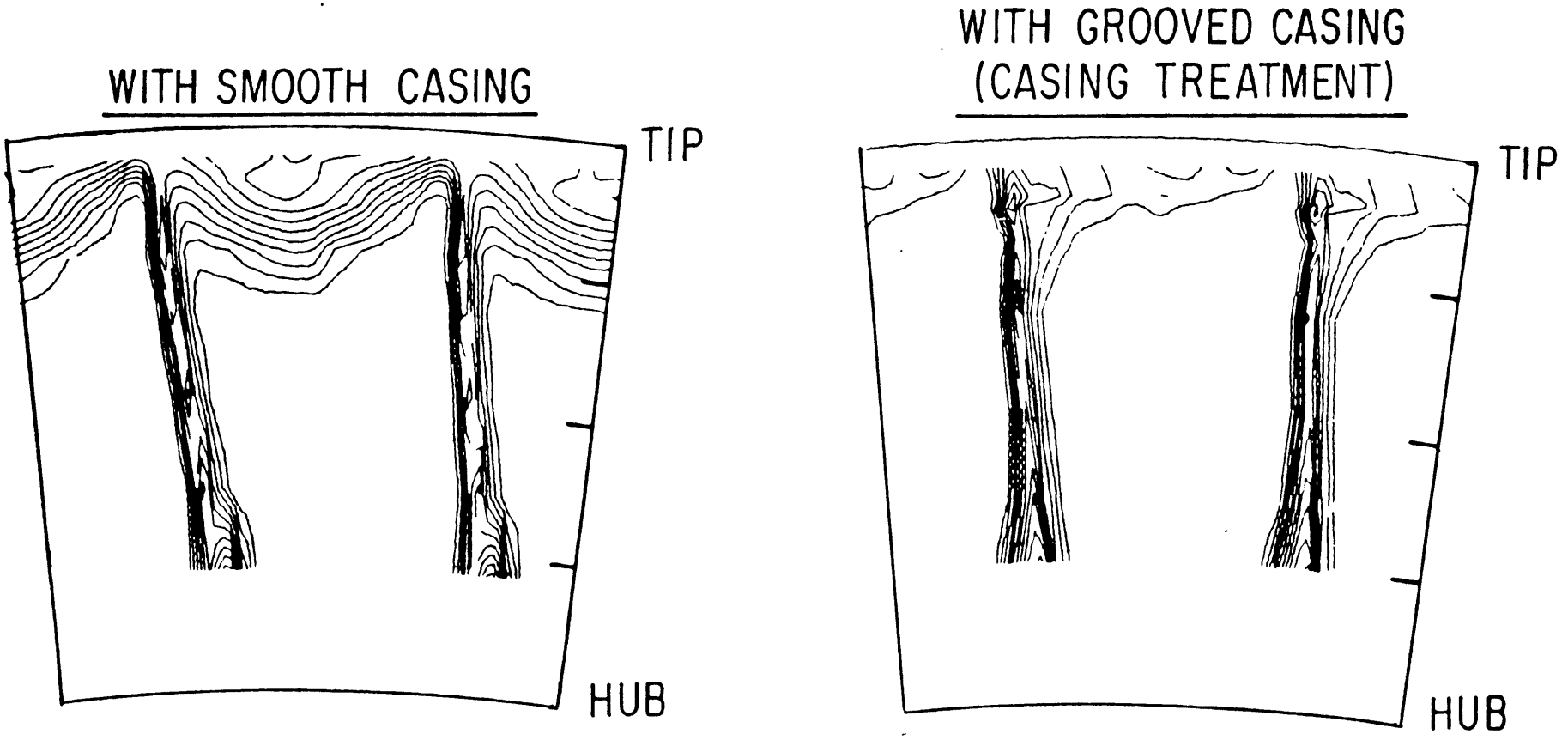

Fig. 4.14 Grietzers casing treatment results

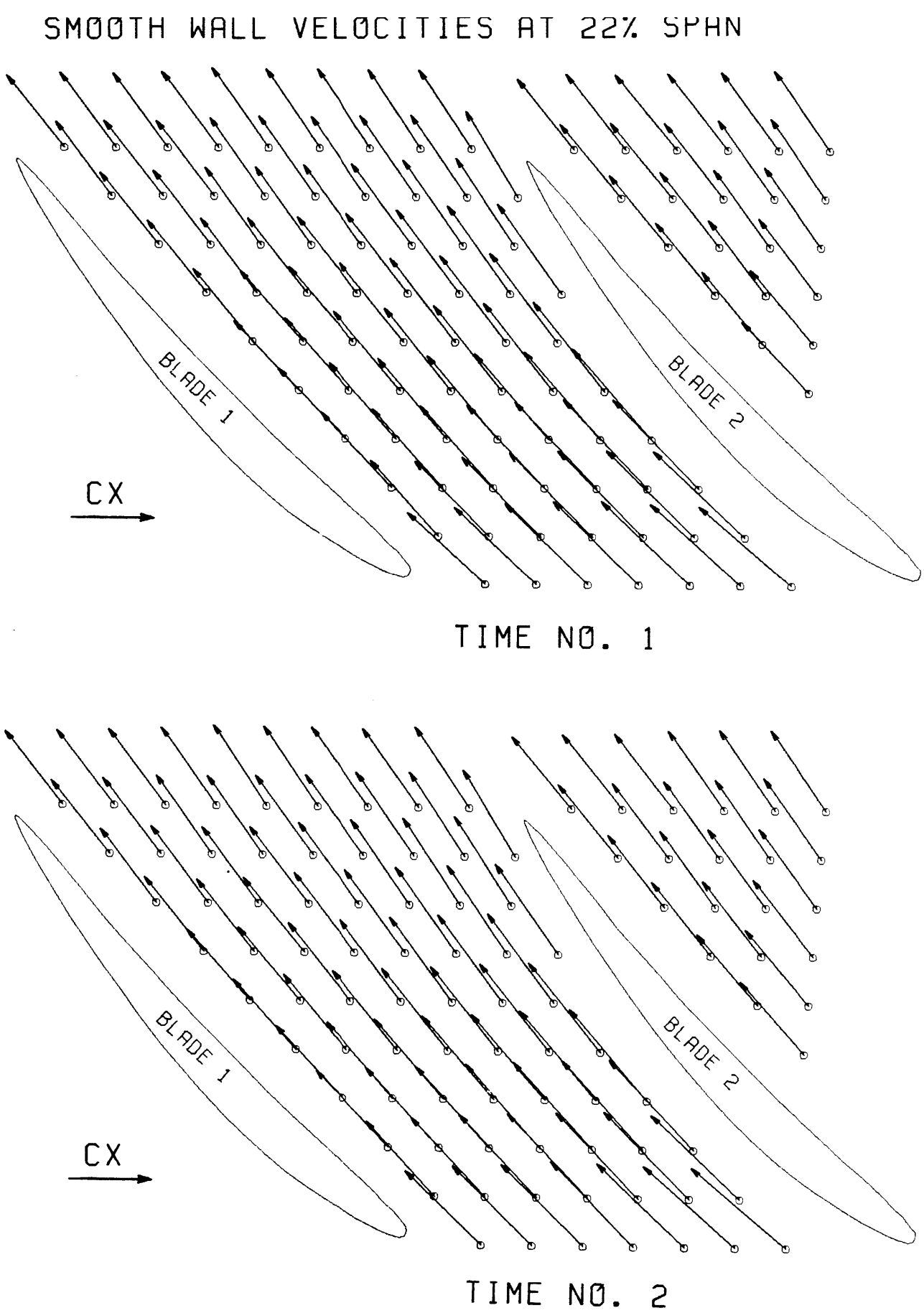

Fig. 4.15 Instantaneous smooth wall velocities at 6% span

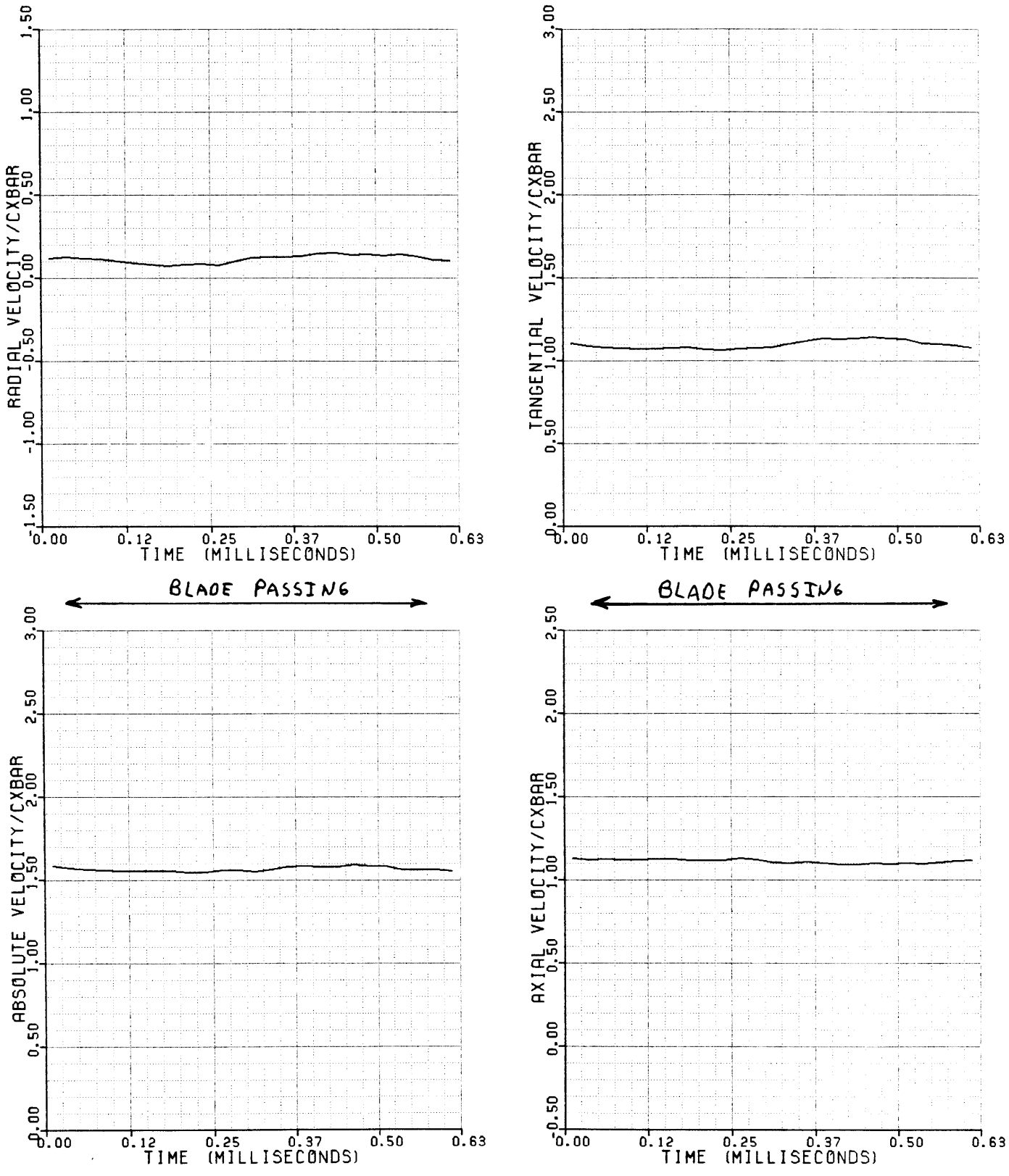

Fig. 4.16 Smooth wall velocity components at 22% span.

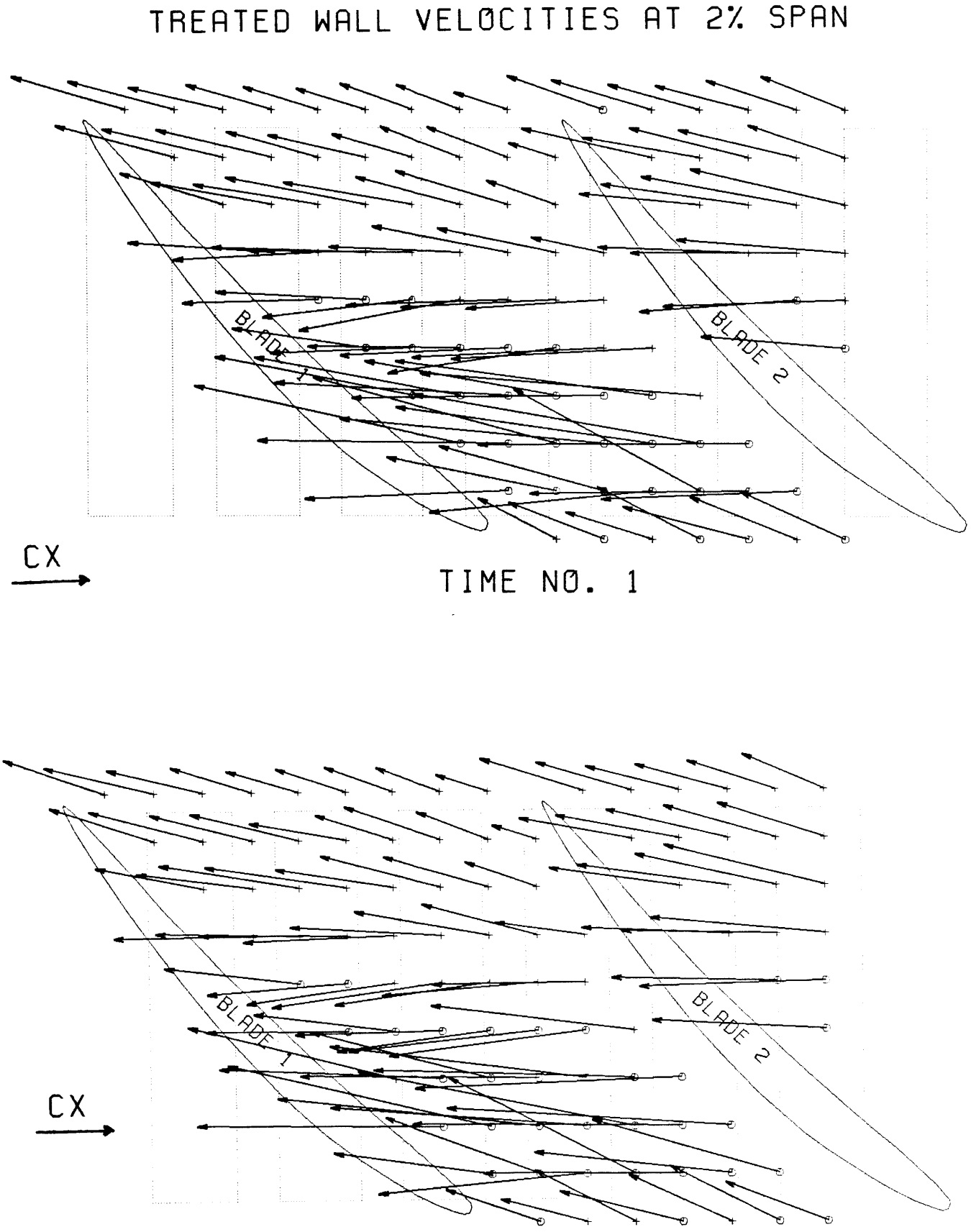

Fig. 4.17 Instantaneous treated wall velocities at 2% span

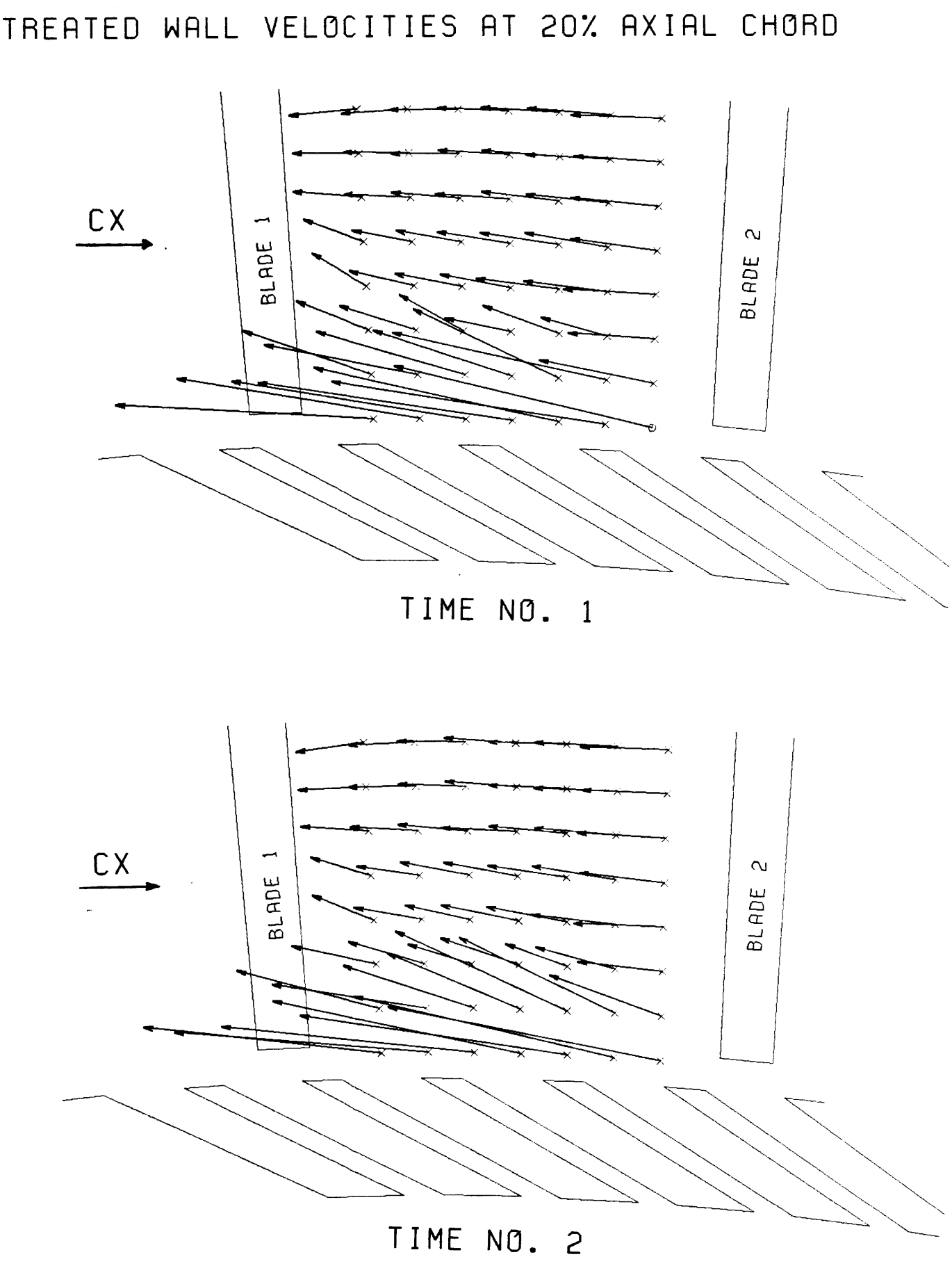

Fig. 4.18 Instantaneous treated wall velocities at 20% axial chord

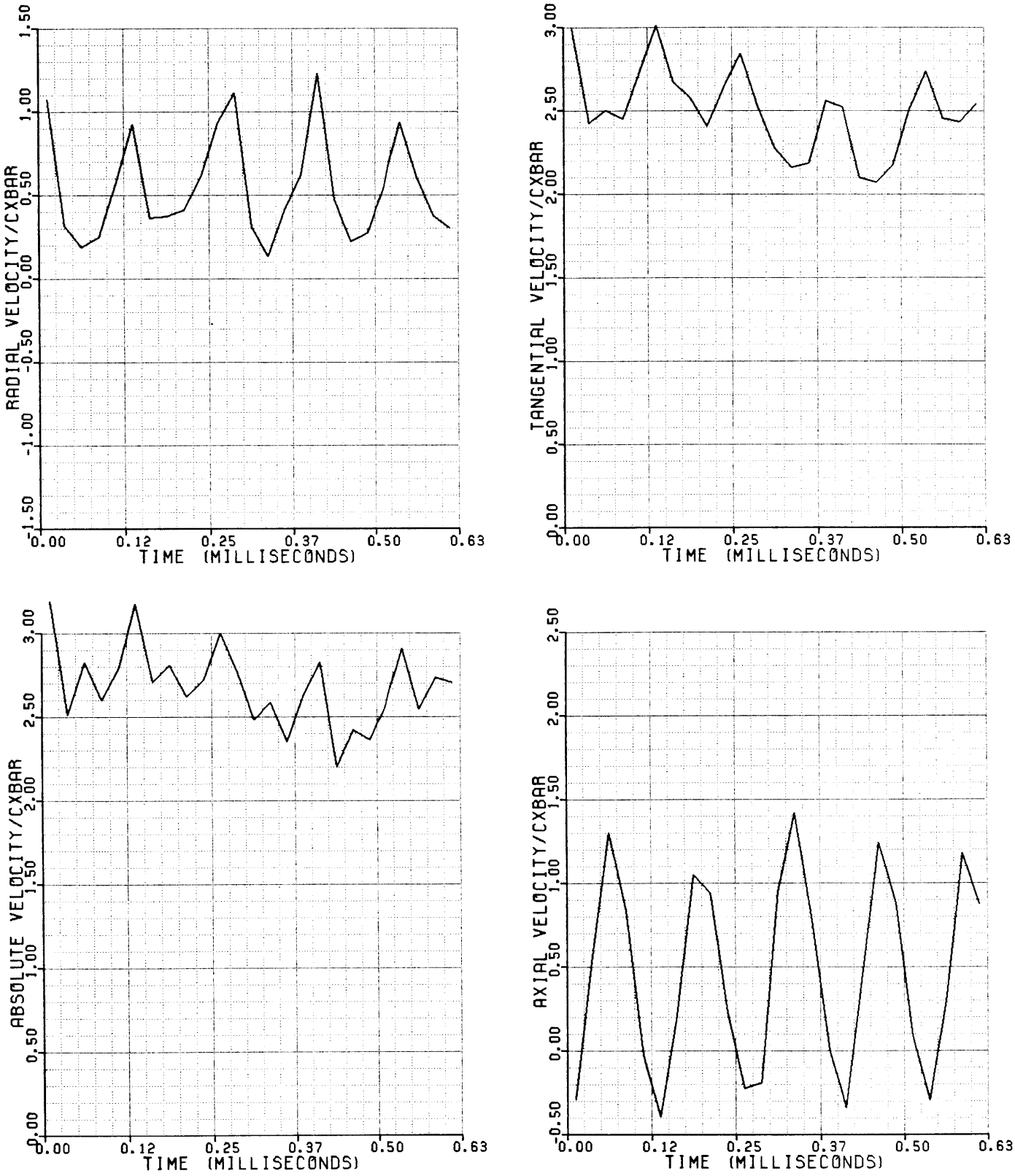

Fig. 4.19 Treated wall velocity components at 2% span

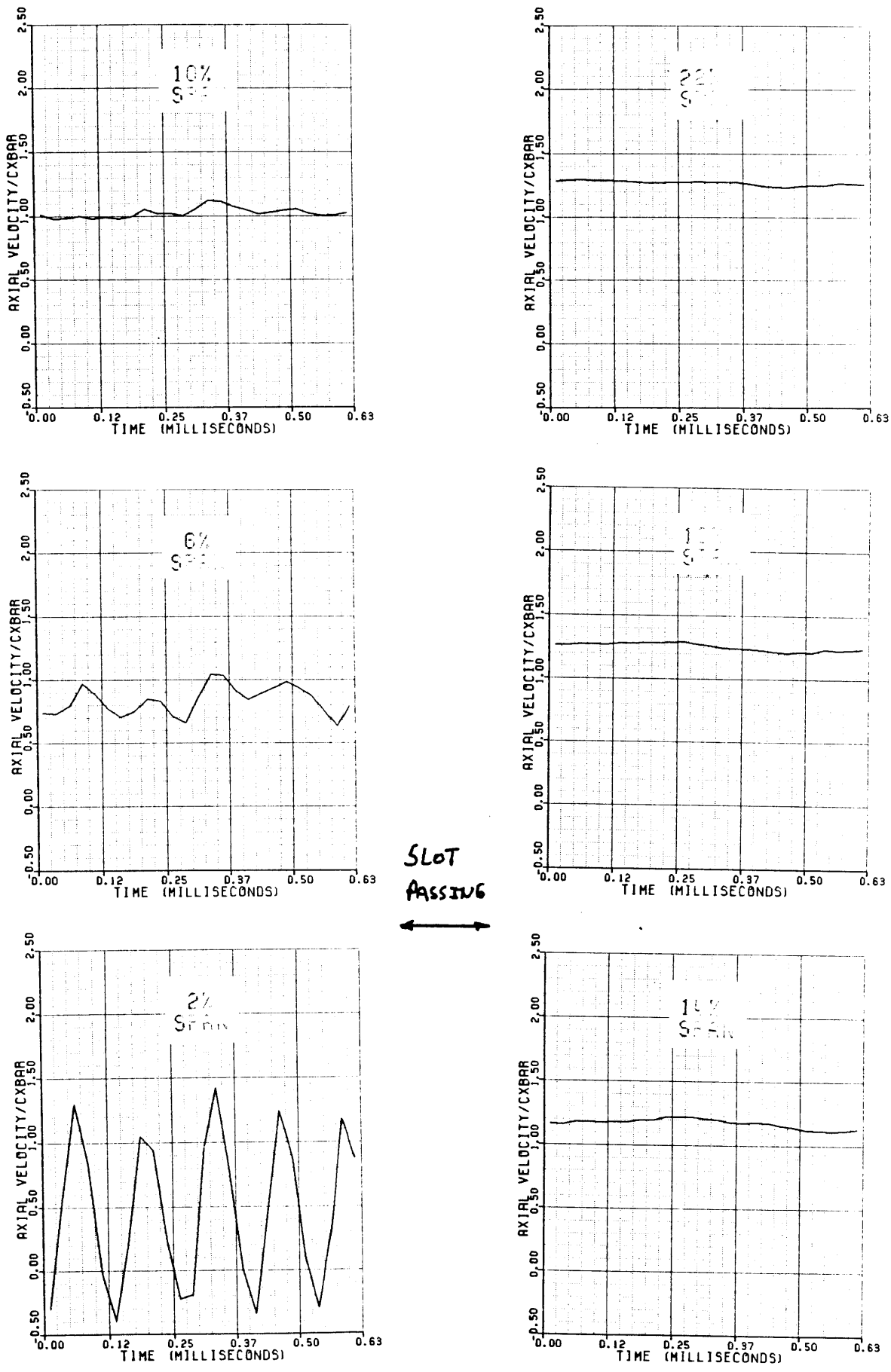

Fig. 4.20 Decay of axial unsteadiness near leading edge

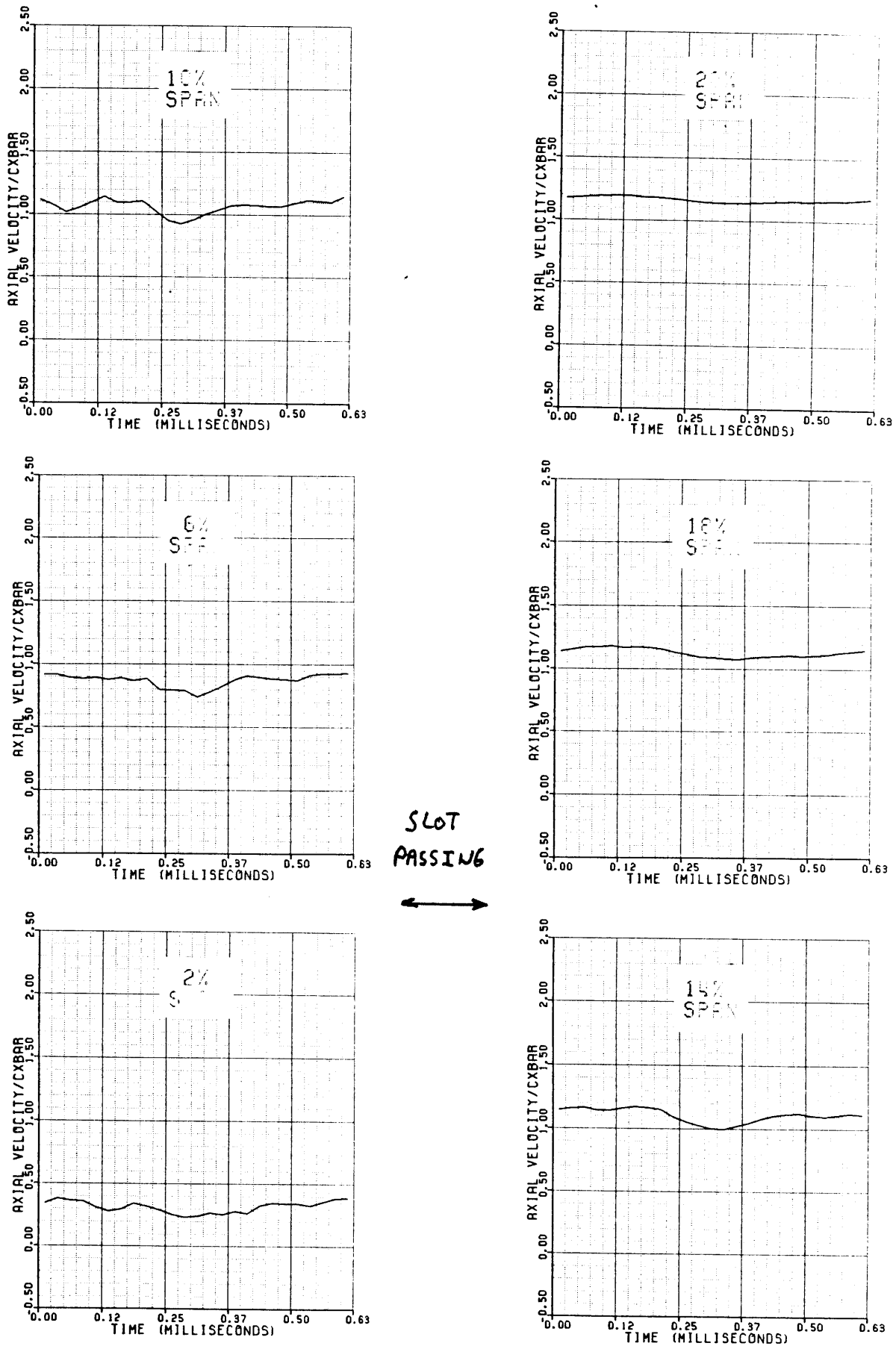

Fig. 4.21 Decay of axial unsteadiness near trailing edge

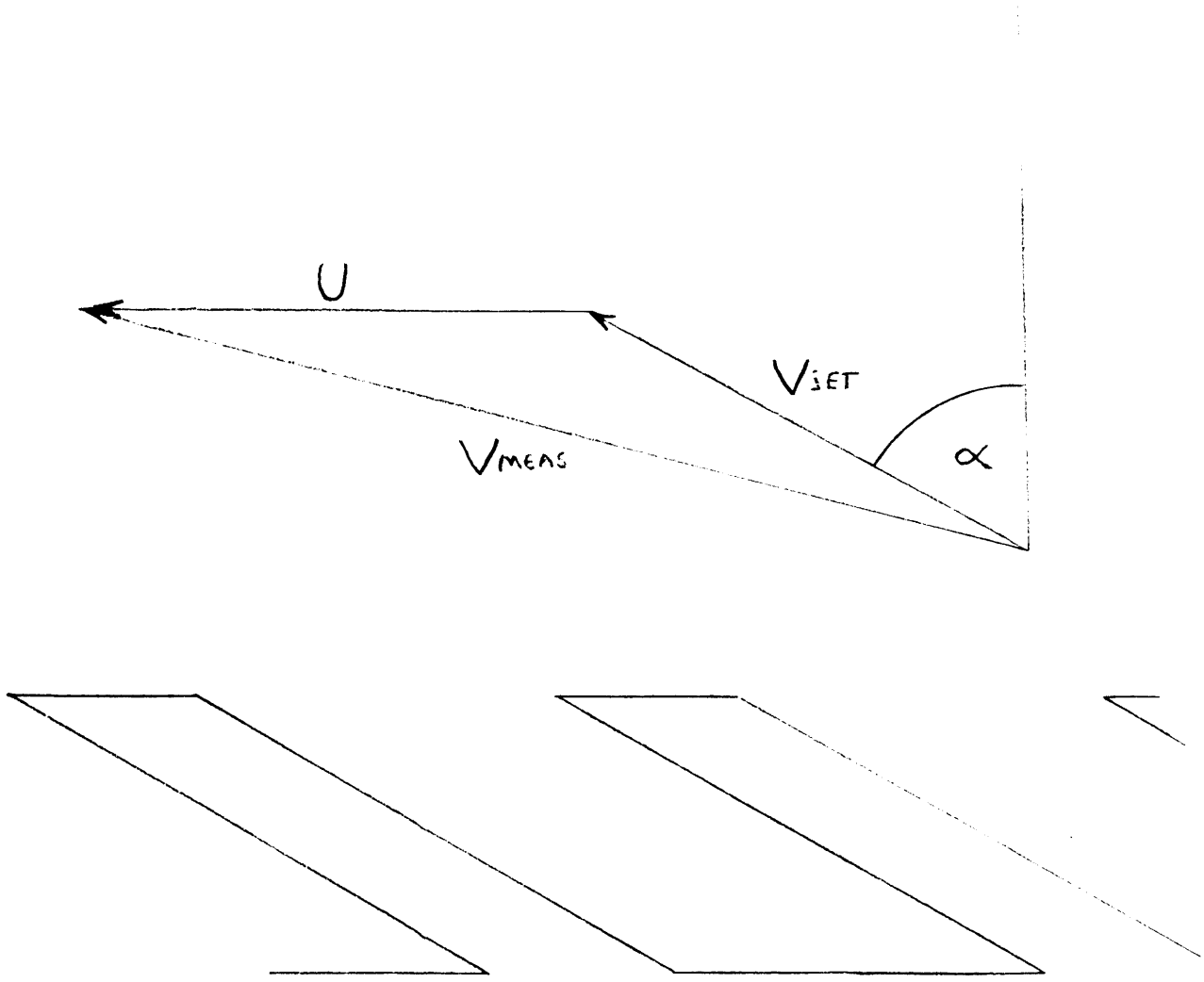

Fig. 5.1 Jet direction and magnitude

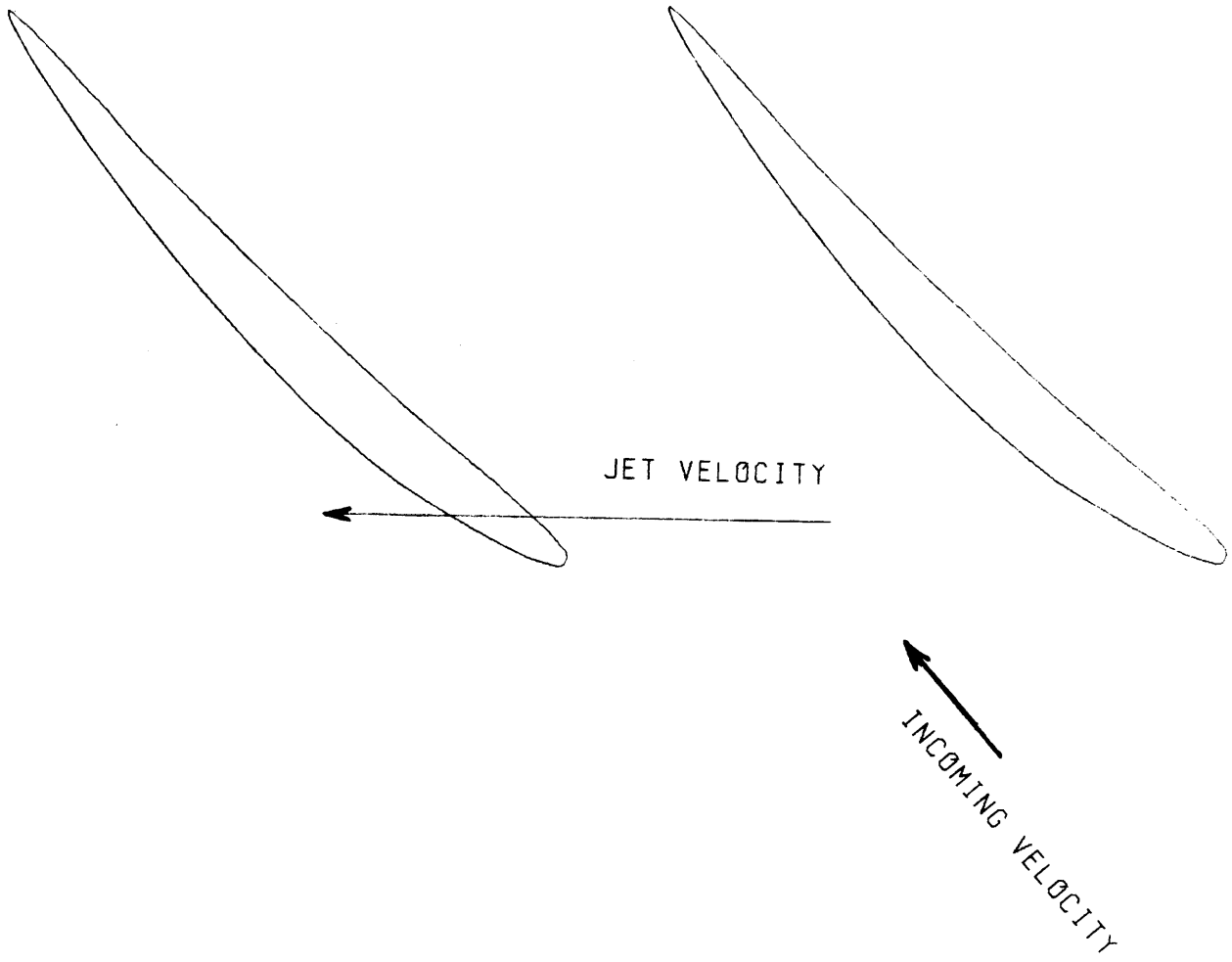

Fig. 5.2 Incoming free stream velocity and the jet

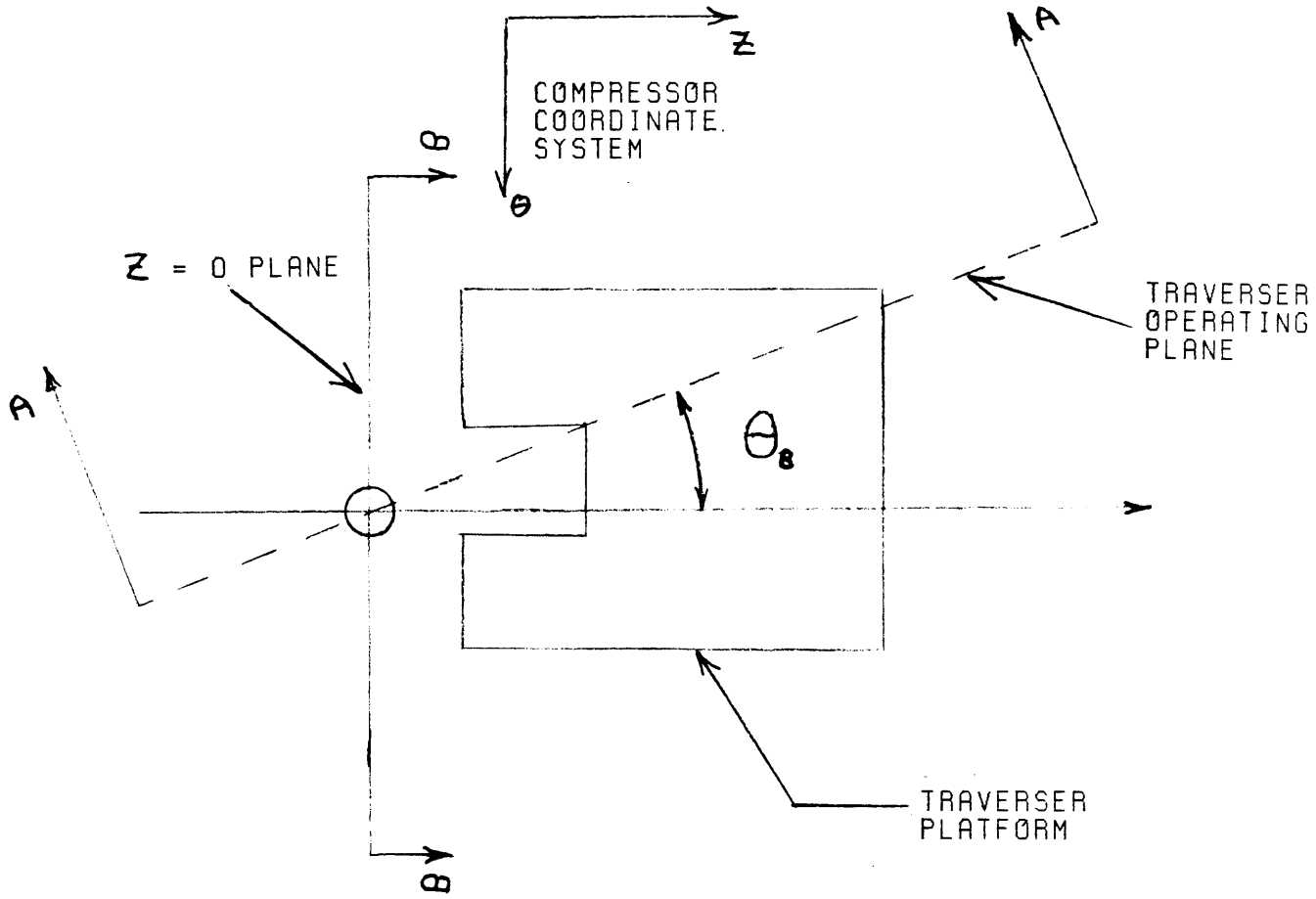

Fig. A.1 Positioning system external geometry

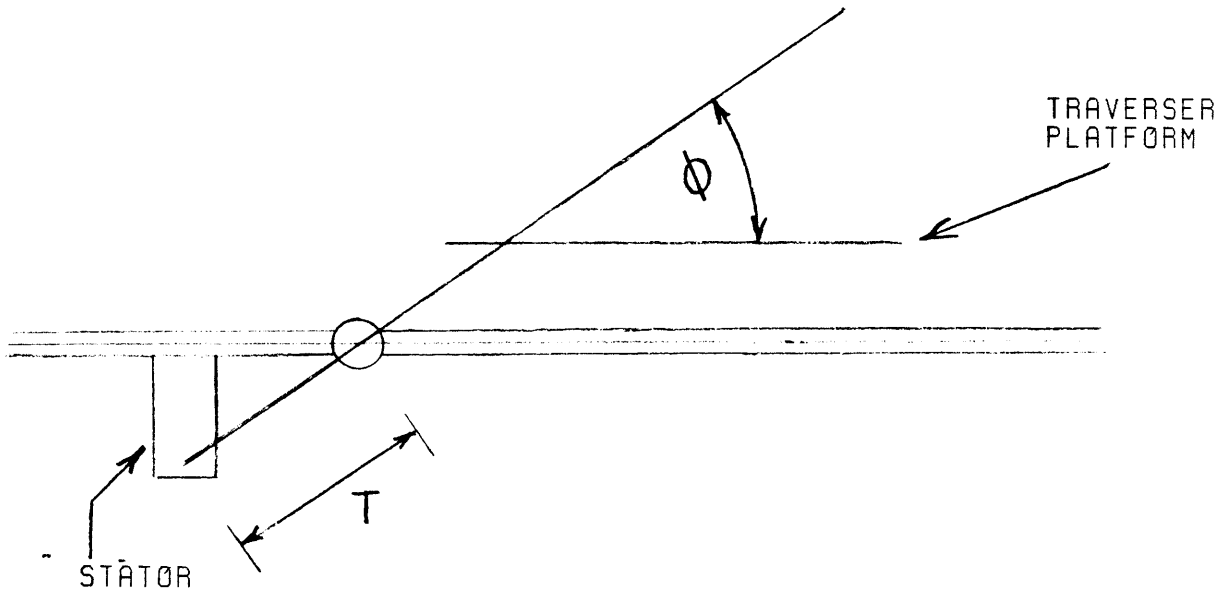

Fig. A.2 View of positioning system geometry at section A-A

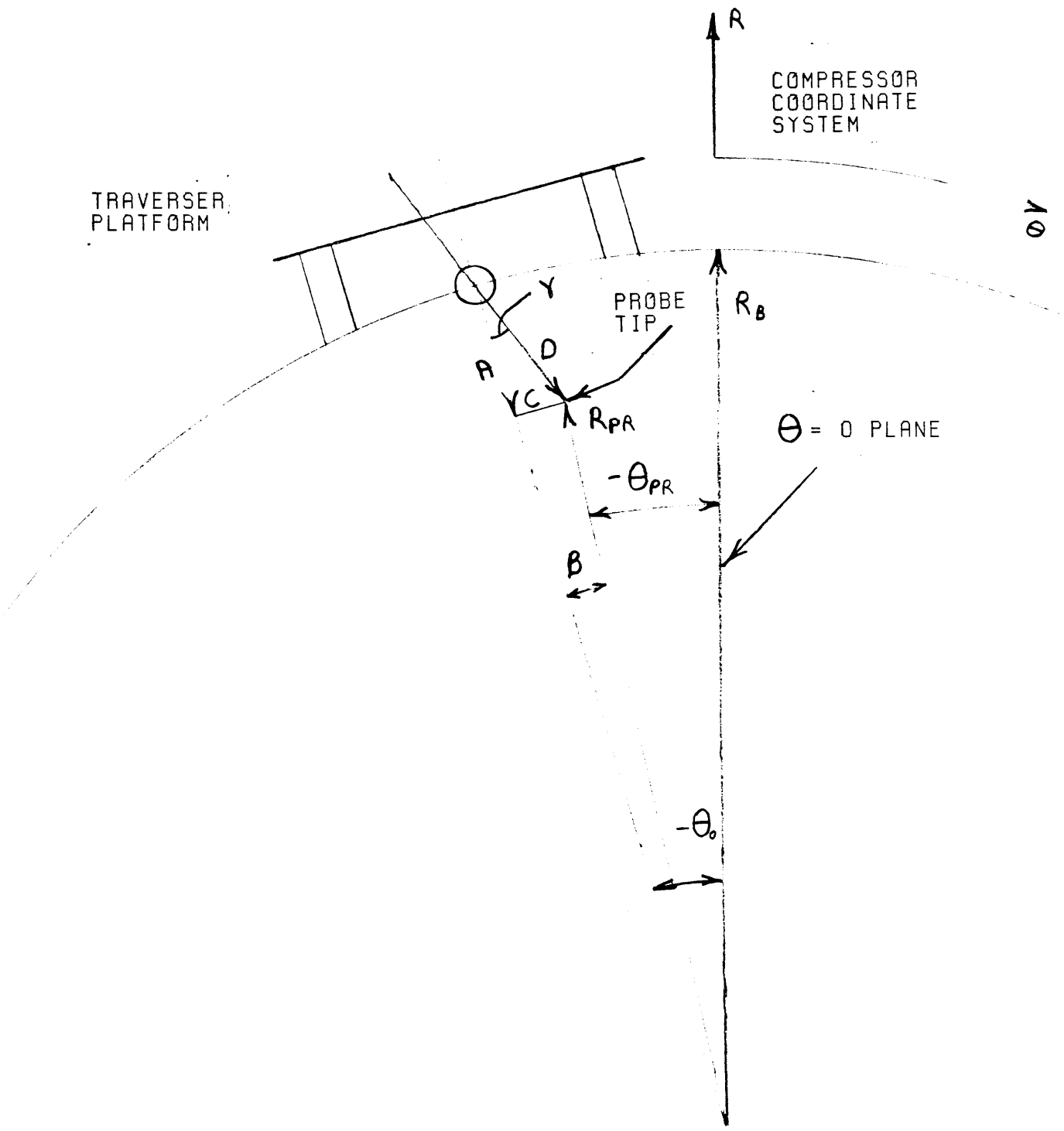

Fig. A.3 View of positioning system internal geometry

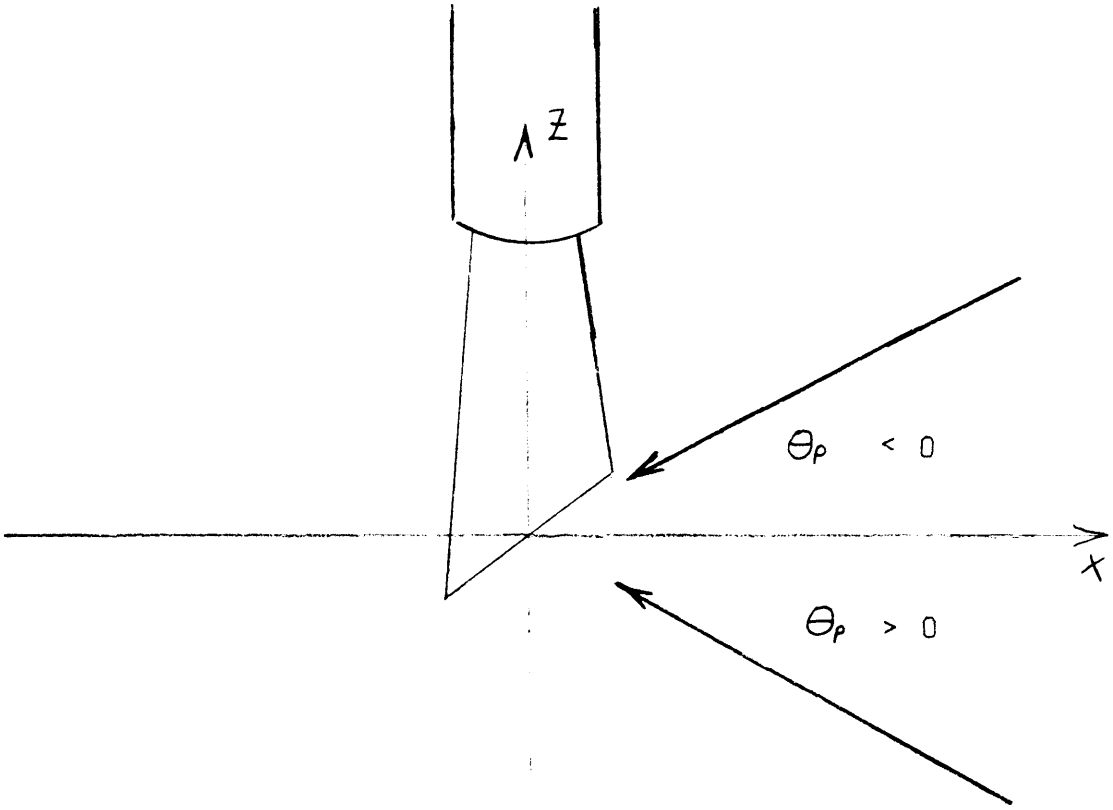

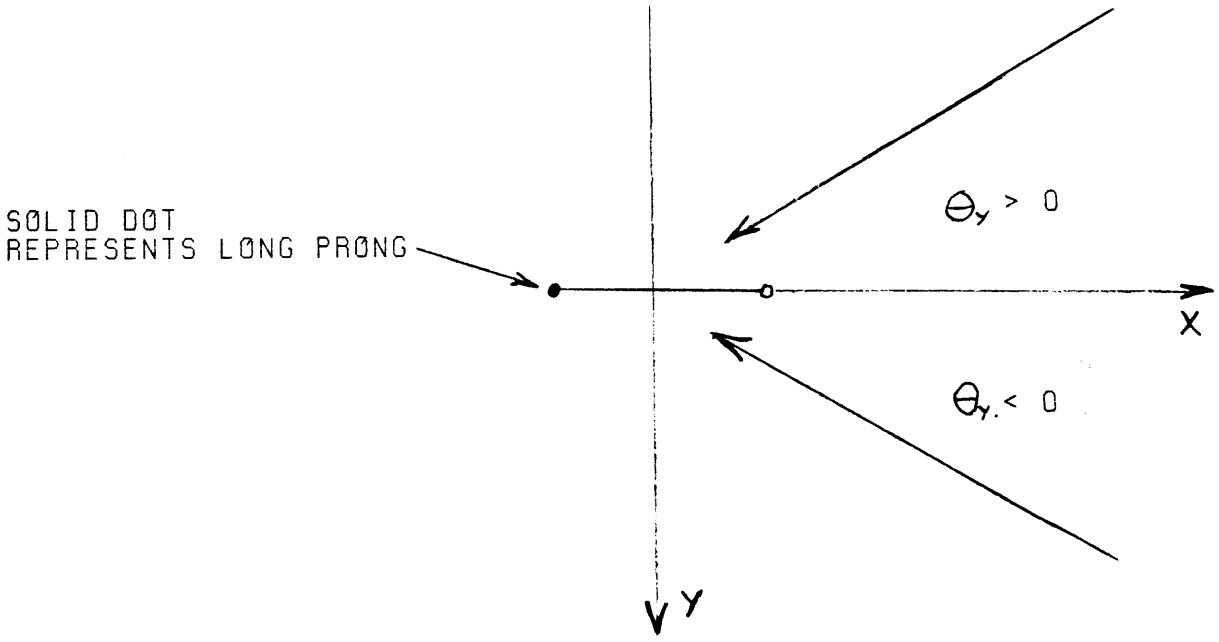

Fig. B.1 Conventions for pitch and yaw angles

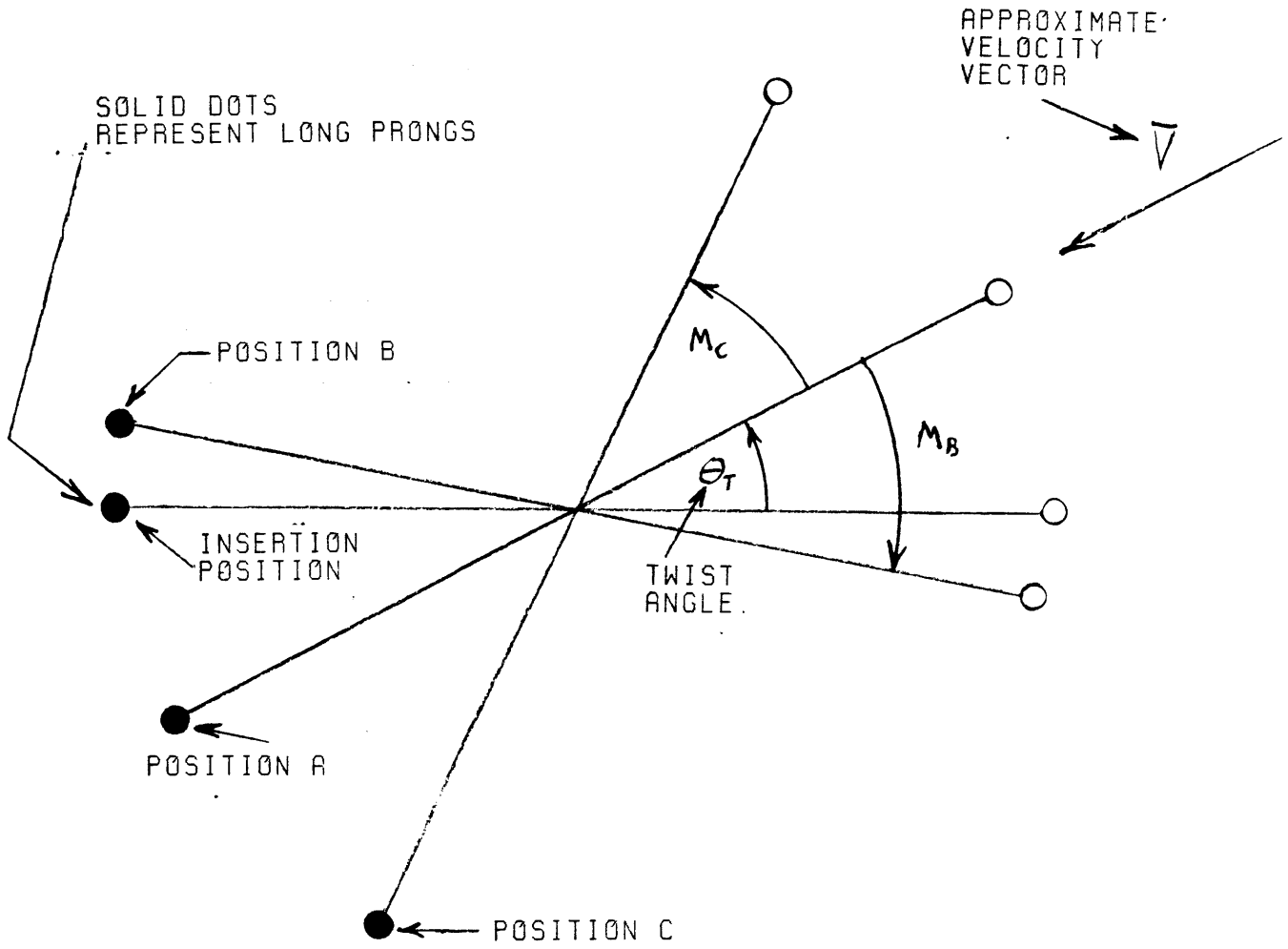

Fig. B.2 Different orientations of the hotwire

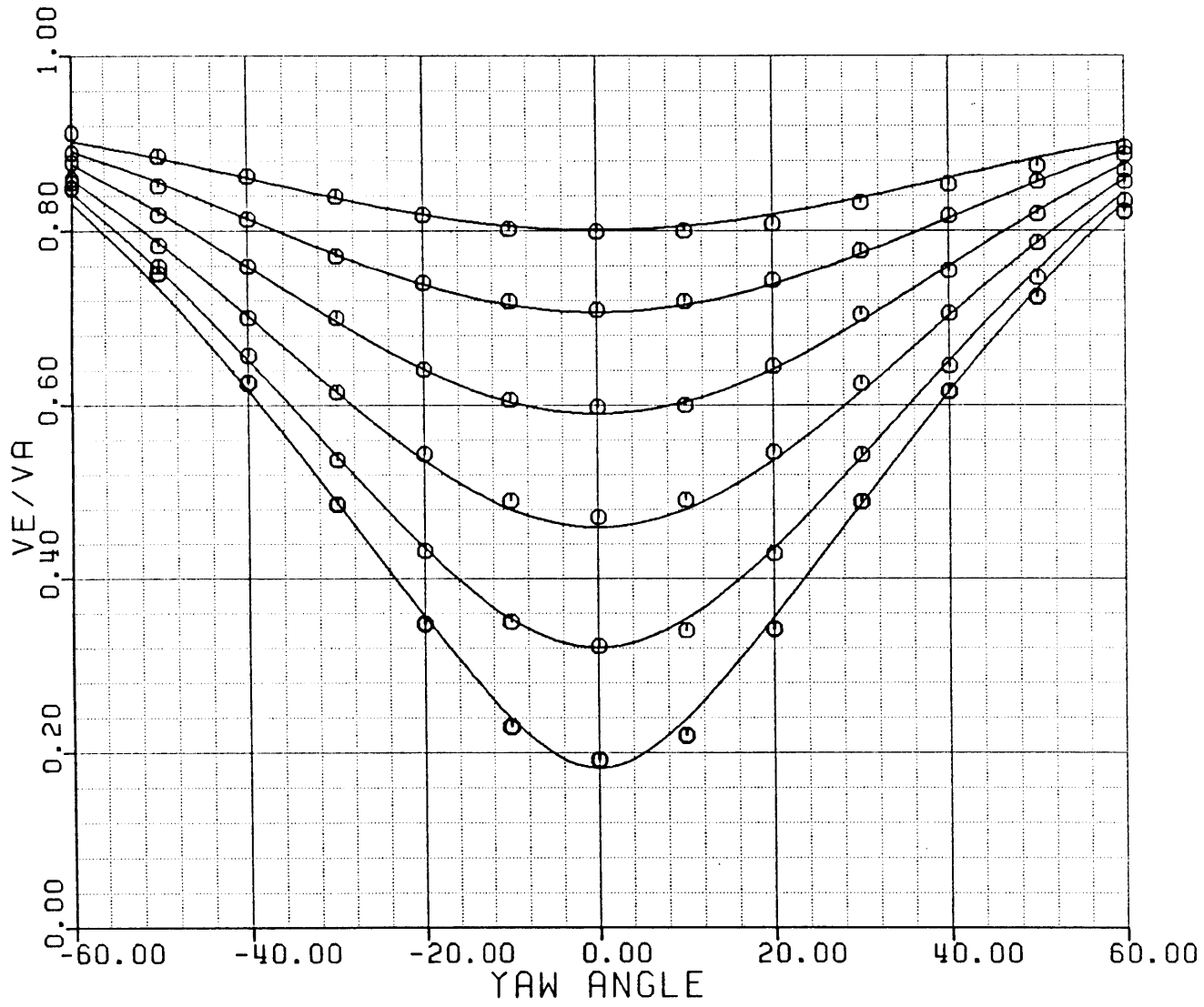

Fig. B.3 Typical directional calibration for 0 degrees of slant

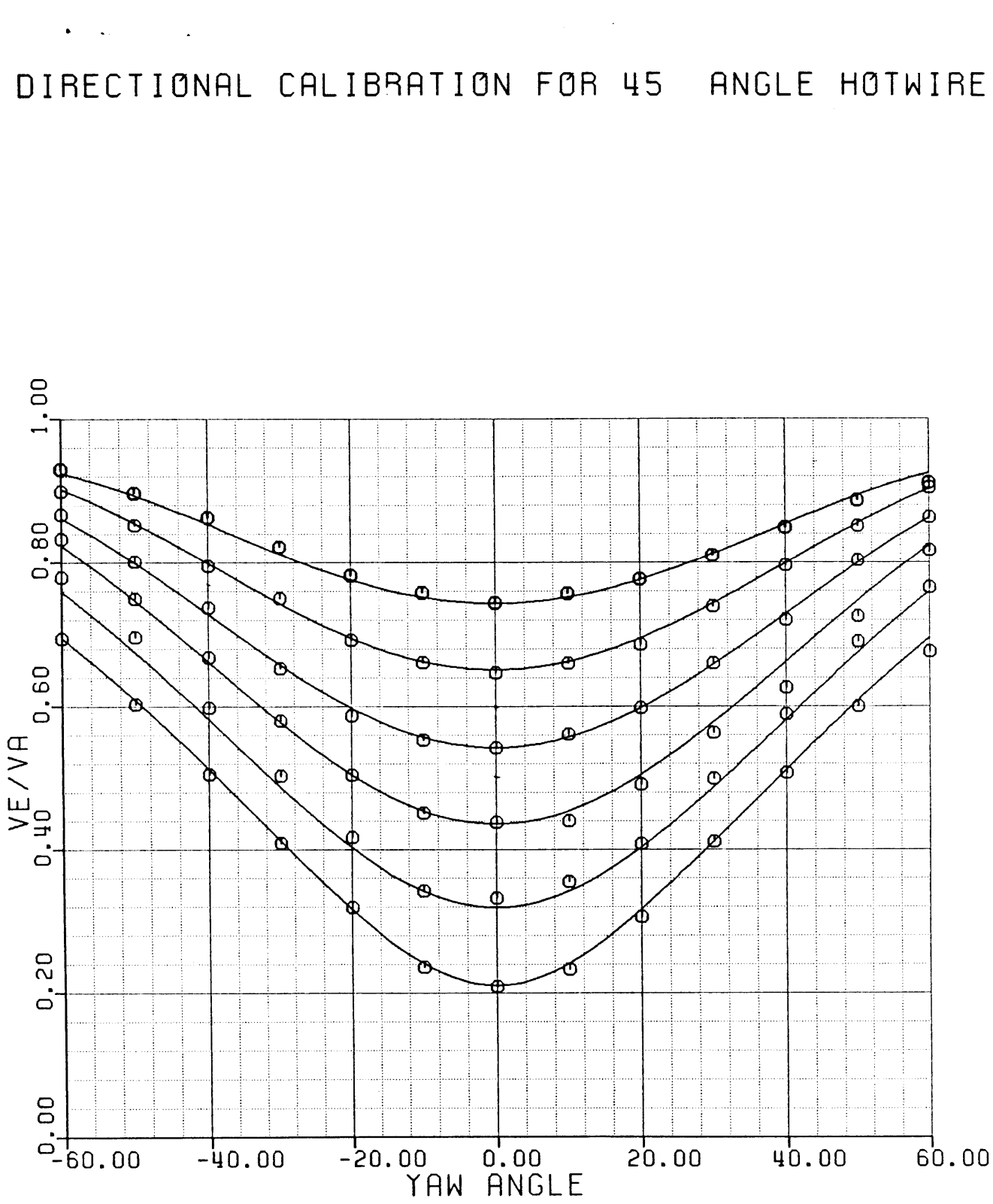

Fig. B.4 Typical directional calibration for 45 degrees of slant

APPENDIX A
POSITIONING SYSTEM GEOMETRY AND OPERATION

This appendix provides a detailed description of the design, geometry, calibration, and use of the hotwire positioning system. In the present experiment, this system, which is a network of mechanical and electrical devices, was used to precisely maneuver a hotwire probe (it could be used for any probe) in a single blade passage.

A.1 DESIGN OBJECTIVES AND RESULTS

The specifications of the positioning system were quite stringent; it was required to be very accurate, flexible, and automated. The accuracy was needed because the region to be investigated was only .5 IN^3 in volume and it was desired to resolve all flow phenomenon in this region. The final system was capable of positioning the probe at any spatial location within a radius of .5mm. This was measured directly and the level of accuracy estimated (within .5mm) was limited by the author's ability to measure the error. The system needed to be flexible because it was not known a priori where the regions of interest would be (e.g. suction surface, pressure surface, L.E., or T.E.). The final configuration was able to reach all regions of interest. Lastly, since it was desired to take a large number of data points (800 points for each build), it was desirable to have the system as automated as possible. The final design had only one link that was not completely computer

controlled.

A.2 DESCRIPTION

Figures 2.2 and 2.3 show the major components of the positioning system, the traversing mechanism (screw actuator), the 15/1 reduction gear box, the angular transducer, and the stepping motor. The screw actuator is the heart of the system and the other components work together to move it in the traversing plane. The actuator itself can translate along it's axis or rotate about it's axis.

The circumferential location of the probe is controlled by moving the entire traverser platform. This is done by sliding the inner sleeve that the platform is mounted on. Unfortunately this circumferential movement is not automated, rather it is affected manually via a chain and gearbox located beneath the compressor. To measure the circumferential location a linear displacement transducer is mounted on the traversing platform and the output of this transducer is calibrated with circumferential location.

A.3 EXTERNAL GEOMETRY

To effectively calibrate and use the positioning system described above it is necessary to have an in-depth understanding of the geometry which determines the movement of the probe. This geometry is broken in to two parts, the

external geometry, which is what is directly controlled by the positioning system, and the internal geometry, which is more complicated and relates external parameters to probe location.

A view of the positioning system external geometry is presented in Fig. A.1. This view is a top view and it contains most of the important geometry information. To begin with, one should note the compressor coordinate system which is cylindrical and contains three components R,Z,θ. The Z direction is axial, positive in the downstream direction, and is measured from the center of the traverser ball. The component measures circumferential location and is positive in the clockwise direction if one looks downstream. Furthermore, the origin for the component, i.e. the angular location where θ=0, is the top dead center of the compressor. The R component is measured radially from the centerline of the compressor.

With the compressor coordinate system firmly in mind (remember the compressor coordinates are what really counts in the end) one can consider other features of the geometry. One important feature is the traversing ball, which was mentioned above. The center of this ball is a reference for several important parameters. One of these parameters is the traverser operating plane angle, θ_β. θ_β, a constant, is the angle between the traverser operating plane and an R-Z plane which passes through the traverser ball center. Furthermore, and this is crucial, θ_β is measured in a plane that is normal to a radial line passing through the traversing ball center. It so

happens that the traverser platform lies in such a plane.

Section A-A of Fig. A.1 designates a view of the positioning system normal to the traverser operating plane and this view is presented in Fig. A.2. In this view the length t is the distance from the probe sensor to the traverser ball center. This length is controlled by the translational movement of the screw actuator. The other parameter seen in Fig. A.2 is the angle ϕ. This is the angle between the actuator axis and a plane normal to a radial line passing through the traverser ball center measured in the traverser operating plane. The traverser platform was positioned such that it lies in a plane normal to a radial line passing through the traverser ball center so, in practice, the angle may be measured relative to the traversing platform. As mentioned before the angle Φ, which determines the position of the traversing mechanism in the traversing plane, is controlled by the 15/1 reduction gear box and the stepping motor. As changes the angular transducer, which is mounted onto the shaft of the gear box, rotates and thus yields a measure for . The output of the angular transducer is calibrated with and is monitored by an analog to digital converter and a microcomputer. The stepping motor is also controlled by the computer and thus closes the loop and allows for completely automated computer control of the angle ϕ.

A.4 INTERNAL GEOMETRY

The internal geometry relates parameters like ℓ, ϕ, and θ_B to actual probe location. Section B-B designates a view of the geometry looking downstream at a Z-θ plane passing through the traverser ball center. This view is seen in Fig. A.3. Once again one should observe the compressor coordinate system. Note that the θ=0 plane is designated and it passes through top dead center and also the view itself is in the plane Z=0 cutting through the traverser ball center. The first parameter to consider is θ_0 which is the angular location of the traverser ball center in the compressor coordinate system. In fact, the coordinates of the traverser ball center are $(R,\theta,Z)=(Rb,\theta_0,0)$. Note that θ_0 is positive in the clockwise direction so that in Fig. A.3 θ_0 is negative. As mentioned previously, circumferential position is calibrated with the output of the linear transducer pictured in Fig. 2.3. Specifically, the angular location of the ball center, θ_0, is calibrated with the output from the linear transducer. As will be shown, with the value of θ_0 the angular location of the probe θ_{p_r} can be determined. In fact, given θ_B, α, θ_0, and ℓ, the location of probe head is completely determined.

A.5 EQUATIONS AND RESULTS

To determine the location of the probe (R_p,θ_p,Z_p) as a function of θ_B, ϕ, θ_0, and ℓ, it is necessary to define and use some intermediate quantities. These quantities are seen in Fig. A.3. D is the projection of ℓ in the Z=0 plane. To determine D we make use of A and C. C is the distance from the

probe tip to an R-Z plane passing through the traverser ball center. C is normal to the R-Z plane. A is the radial distance from the traverser ball center to the radial location of the intercept of the length C with the R-Z plane passing through the traverser ball center. A simple geometry transformation shows that A and C are defined in terms of and by the following equations.

$$A = t\,SIN(\alpha) \tag{A.1}$$

$$C = t\cos(\alpha)\,SIN(\theta_B) \tag{A.2}$$

Both D and ALPHA are now simply related to A and C and thus are determined since t, α, and θ_B are given. Rb is the radial location of the traverser ball center in compressor coordinates and is a constant equal to 304.89mm. Rb too is needed to represent probe location. By using the law of cosines R_p, the probe radial location, is described as follows:

$$R_p = \sqrt{R_B^2 + D^2 - 2DR_B\cos(\alpha)} \tag{A.3}$$

Upon substitution for D, Rp becomes:

$$R_p = \sqrt{R_B^2 + \left(t\,SIN(\alpha)\right)^2 + \left(t\cos(\alpha)\,SIN(\theta_B)\right)^2 - 2R_B t\,SIN\alpha} \tag{A.4}$$

Once Rp_r is known β may be calculated by the law of sines. Also θ_{p_r} the angular location of the probe is known in terms of θ_0 and β. Therefore θ_{p_r} is determined as fcllows:

$$\theta_{p_r} = \theta_o + ARCSIN\left(t/Rp\,SIN(\theta_B)\cos\alpha\right) \tag{A.5}$$

Lastly, Zp_r is determined by a simple coordinate transformation

just as A and B were.

$$z_p = -t\cos\phi\cos\theta_B \tag{A.6}$$

Equations A.4 through A.6 now define the probe location (Rp, θp,Zp) in terms of θ_B, t, ϕ, θ_0, and a constant Rb.

A.6 REVERSE PROBLEM

The procedure outlined above is only half the problem because in practice the desired probe location (Rp, p,Zp) is specified and it necessary to configure the positioning system to yield that position. Therefore what is needed is t, ϕ, and θ_0 given the desired position (Rp,θp,Zp) and the constants Rb and θ_B. This information can be obtained by a manipulation of equations A.4 through A.6. First we proceed by using the following substitution.

$$t\cos\phi = |z_p|/\cos\theta_B \tag{A.7}$$

Applying this substitution in A.4 yields, after minor manipulations, the equation

$$(t\sin\phi)^2 - 2R_B(t\sin\phi) + \left(R_B^2 - R_{Pr}^2 + (z_p\tan\theta_B)^2\right) \tag{A.8}$$

which is a quadratic in $t\sin(\phi)$. Solving A.8 for $t\sin(\phi)$ and considering only the physically acceptable root yields

$$t\sin\phi = R_B - \sqrt{R_{Pr}^2 - (z_p\tan\theta_B)^2} \tag{A.9}$$

which, when combined with A.7, yields solutions for ϕ and t.

$$\alpha = \text{ARCTAN}\left[\left(R_B - \sqrt{R_P^2 - (z_{P_r}\text{TAN}\theta_B)^2}\right)/\left(z_P/\cos\theta_B\right)\right] \qquad \text{(A.10)}$$

$$t = 1/\text{SIN}\alpha\left[R_B - \sqrt{R_P^2 - (z_{P_r}\text{TAN}\theta_B)^2}\right] \qquad \text{(A.11)}$$

Lastly, A.5 may be rearranged to yield the following equation for θ_0.

$$\theta_0 = \theta_{P_r} - \text{ARCSIN}\left(t/R_P\,\text{SIN}(\theta_B)\cos\alpha\right) \qquad \text{(A.12)}$$

As emphasized above, equations A.10, A.11, A.12 are the truly useful equations because in practice (Rp, p,Zp) are specified. Therefore, these are the equations used in the data acquisition programs.

APPENDIX B
VELOCITY ACQUISITION TECHNIQUE

A single hotwire technique was used to obtain three-dimensional unsteady velocity vectors. The technique is based on a similar technique presented by Wagner and Okishi [11]. Before the measurement technique can be discussed, some relationships linking probe geometry and hot-wire cooling velocities must be presented.

B.1 PROBE GEOMETRY

The hot-wire sensor, the probe coordinate system, pertinent geometry, and a general velocity vector are shown in Fig. 3.5. The coordinate system is fixed to the probe with the X-Z plane lying on the sensing portion of the probe and the probe axis and with the Y-axis perpendicular to the X-Z plane and centered on the sensor. The wire is slanted an angle α_0 to the X-axis. The velocity vector V can be resolved into components along X, Y, and Z for each orientation of the wire. When the wire and coordinate system are rotated about the Z-axis, the yaw angle, θ_y, changes by the amount of turning, whereas, the pitch angle, θ_p, remains the same. The conventions for θ_y and θ_p are presented in Fig. B.1. As can be seen the pitch angle, which is the angle between the velocity vector and the X-Y plane, is positive when the velocity comes from below, and the yaw angle is positive when the velocity approaches from the left. The sensor angle, α, which is the

pertinent angle for determining heat transfer from the wire, is defined as the angle between the unit slant vector, $\bar{A}$, and the velocity vector, $\bar{V}$. To obtain a relationship between α and α_0, θ_p, and θ_y, the dot product of the two vectors is taken:

$$\bar{A} = \cos\alpha_0 \bar{i} + \sin\alpha_0 \bar{k} \tag{B.1}$$

$$\bar{V} = -|V|\cos\theta_p\cos\theta_y \bar{i} + |V|\cos\theta_p \sin\theta_y \bar{j} + |V|\sin\theta_p \bar{k} \tag{B.2}$$

$$\bar{A}\cdot\bar{V} = |A||V|\cos(180-\alpha) = -|V|\cos\alpha_0\cos\theta_p\cos\theta_y + |V|\sin\alpha_0\sin\theta_p \tag{B.3}$$

$$\cos\alpha = \cos\alpha_0\cos\theta_p\cos\theta_y - \sin\alpha_0\sin\theta_p \tag{B.4}$$

B.2 EFFECTIVE COOLING VELOCITY RATIO

The hot-wire anemometer output correlates to velocity as the output voltage to the fourth power. To make the signal more meaningful it is linearized by a signal conditioner (linearizer). Therefore, the conditioned output, i.e., the output from the linearizer, is approximately proportional to the flow velocity. This linearized signal, El, is calibrated to velocity with the hot-wire sensor normal to the flow, i.e., the sensor angle, α, equal to 90 degrees. This yields

$$V = A_0 + A_1 E_L + A_2 E_L^2 \tag{B.5}$$

where V is the absolute fluid velocity and A0, A1, and A2 are constants determined with a least squares curve fit. Whenever the probe is oriented to the flow at other than a sensor angle, 0, of 90 , the velocity calculated from Eq. B.5 can be considered an effective velocity, Ve, where

$$V_e = A_0 + A_1 E_L + A_2 E_L^2 \qquad \text{(B.6)}$$

The measurement technique used was based on knowing a precise relationship for the effective cooling velocity/absolute velocity ratio, Ve/V, for various orientations of the probe in the flow stream.

Experiments conducted by Schmidt and Okishi [12] showed this velocity ratio was strongly dependent on sensor angle, moderately dependent on pitch angle, and very weakly dependent on velocity, V, itself. Several correlations have been presented to describe Ve/V, however, the present experiment used a correlation recommended by Shin [13], which yielded excellent results. The recommended correlation is as follows:

$$V_e/V = B_0 + B_1\alpha + B_2\theta_p + B_3 V + B_4\alpha^2 + B_5\theta_p^2 + B_6\alpha\theta_p + B_7\alpha V + B_8\theta_p V + B_9\alpha^3 \qquad \text{(B.7)}$$

The coefficients B0 through B9 were determined, for each probe, from a least squares fit of the calibration data as described presently in section B.5.

B.3 MEASUREMENT TECHNIQUE

To obtain the velocity three distinct measurements are required. The hot-wire was rotated about it's axis to three different orientations as denoted in Fig. B.2. These probe positions relate to three different yaw angles $\theta_{y,a}$, $\theta_{y,b}$, $\theta_{y,c}$ which were set as indicated below.

$$\theta_{y,a} = \theta_y \qquad \text{(B.8)}$$

$$\theta_{Y,B} = \theta_Y + mB \tag{B.9}$$

$$\theta_{Y,C} = \theta_Y + mC \tag{B.10}$$

where mb and mc are probe turning angle increments from the a position. It should be emphasized the position a is the primary position and it is relative to this position that the final θy and θp are determined. The values of mb and mc are chosen to orient the probe in a position that suits that probes calibration. For the present experiment a probe slant angle of 0 degrees was used and it was found that for this case, values of mc and mc of 30 -30 respectively worked well. For each orientation of the probe the anemometer output voltage is measured. In the present experiment both time averaged and time resolved measurements were made as described in section 3.4. For each orientation of the wire two equations like B.4 and B.7 are obtained. Therefore, each physical location generates three sets of equations. These equations are:

For position a

$$\cos\alpha_a = \cos\alpha_0 \cos\theta_p \cos\theta_{Y,a} - \sin\alpha_0 \sin\theta_p \tag{B.11}$$

$$V_e/V = B_0 + B_1\alpha_a + B_2\theta_p + B_3 V + B_4\alpha_a^2 + B_5\theta_p^2 + B_6\alpha_a\theta_p + B_7\alpha_a V + B_8\theta_p V + B_9\alpha_a^3 \tag{B.12}$$

For position b

$$\cos\alpha_b = \cos\alpha_0 \cos\theta_p \cos\theta_{Y,b} - \sin\alpha_0 \sin\theta_p \tag{B.13}$$

(B.14)

$$V_e/V = B_0 + B_1\alpha_b + B_2\theta_p + B_3 V + B_4\alpha_b^2 + B_5\theta_p^2 + B_6\alpha_b\theta_p + B_7\alpha_b V + B_8\theta_p V + B_9\alpha_b^3$$

For position c

$$\cos\alpha_c = \cos\alpha_0 \cos\theta_p \cos\theta_{y,c} - \sin\alpha_0 \sin\theta_p \quad \text{(B.15)}$$

$$V_e/V = B_0 + B_1\alpha_k + B_2\theta_p + B_3 V + B_4\alpha_c^2 + B_5\theta_p^2 + B_6\alpha_c\theta_p + B_7\alpha_c V + B_8\theta_p V + B_9\alpha_c^3 \quad \text{(B.16)}$$

By substituting B.8, B.9, and B.10 into B.12, B.14, and B.16, the six unknown variables $\alpha_a, \alpha_b, \alpha_c, \theta_p, \theta_y$, and V remain in the six equation B.11 through B.16. These equations were solved simultaneously as described presently in section B.4. The three dimensional vector is completely described with the variables θ_p, θ_y, and V known relative to orientation a.

The procedure for arriving at the primary position a is an important one. First, the probe is inserted in some known position called the insertion position. The insertion position, which is shown in Fig. B.2, is at an orientation such that the hot-wire sensor aligns in the traverser operating plane, which is shown in Fig. 2.2. From this orientation the probe is turned some angle, called the twist angle, to orient the probe into the velocity vector. This twist angle is determined by monitoring the output of the hotwire anemometer. When the anemometer output is at a minimum that indicates the probe is headed into the flow ($\theta_{y=0}$) and that location fixes the twist angle. It should be noted that when the flow is unsteady things are not as straight-forward. In this case the position of minimum output is based on the time averaged output. From the discussions above, it is clear that position a is at an orientation that aligns the sensing wire into the flow and is an angle θ_t away from the insertion position. In

practice it was found that position a didn't need to align exactly into the flow and that one setting of the twist angle would do for a whole region of the flow field.

B.4 VELOCITY TRANSFORMATION

Once the values of θ_y, θ_p, and V are determined at a given location the three dimensional velocity vector is known in the probe coordinates (see Fig. 3.5). To relate this to the velocity vector in compressor coordinates a rather involved velocity transformation is required. This transformation involves several rotations of the coordinate system about certain axes and results, as would be expected, in a series of matrix multiplications where the components of the matrices are trigonometric functions of certain angles.

To begin with, define the velocity in probe coordinates as (Vx,Vy,Vz) with values given by

$$Vx = -V\cos(\theta p)\cos(\theta y)$$

$$Vy = V\cos(\theta p)\sin(\theta y)$$

$$Vz = V\sin(\theta p)$$

Then, the velocity in compressor coordinates is given by

TABLE B-1 ON PAGE 112.

This equation is, of course, programmed into a data reduction program where the transformation is done automatically.

B.5 CALIBRATION PROCEDURE

As mentioned previously there are two parts two the calibration procedure, the calibration of effective velocity, Ve, versus linearizer output, El, and the calibration of Ve/V for a range of pitch angle, yaw angle, and velocity. The former is referred to as the linear calibration (since Ve is approximately linear with El) and the later is called the directional calibration. In each calibration the air is supplied by a compressor and is delivered to a calibration nozzle. This nozzle generates a controllable jet of air which is used for calibration.

To perform the linear calibration, which is relatively easy, one inserts the probe into the calibration jet at a yaw angle of 90. This yields a sensor angle of 90. Then the jet velocity is adjusted to different values and the output voltage recorded. Typically twenty points are sufficient and the velocity is curve fitted with a second-order equation as given in eq. B.6.

The calibration for Ve/V is much more demanding. In this case the jet absolute velocity V is kept constant while the

wire is rotated to various orientations. The positioning of the wire is done in a systematic way. First, the pitch angle is fixed, then the yaw angle is varied from -60 to +60 in increments of 10. For each yaw angle the linearizer output is recorded. This procedure is repeated for a range of pitch angles thus yielding output voltages for a matrix of pitch and yaw angles for that preset velocity. The entire procedure is then repeated for a second velocity. The two calibration velocities are chosen to represent the range of velocities expected in the actual experiment. Finally all the data is used to generate a least squares curve fit in equation B.7. This curve fit generates the coefficients B0-B9.

The choice of pitch angles used in the above calibration is a crucial one. As mentioned previously, different probes with different slant angles, α_0, have different ranges of calibration. In general the minimum pitch angle cannot position the probe such that the short prong is obstructing the oncoming flow. Therefore, for a probe with $\alpha_0=45$ the minimum pitch angle is -45 and for a probe with $\alpha_0=0$ the minimum pitch angle is 0. The maximum pitch angle is determined by looking at calibration data. To illustrate this consider Figures B.3 and B.4. Fig. B.3 presents a typical calibration curve for a wire with $\alpha_0=0$ and Fig. B.4 presents a typical calibration curve for $\alpha_0=45$. In each figure the circles represent calibration data and the solid lines are the curve fit. There are several important points to be observed in the plots. To begin with each probe has a totally different range of pitch

angles over which it is useful. For the probe with $\alpha_0=0$, which is what was needed for the present experiment, the range is +10 to +60 (actually the upper limit could easily be extended to +70) and for the probe with $\alpha_0=45$ the range of pitch angles is -30 to +20 (actually the calibration could have extended from -40 to +30). Therefore, one has to choose a probe that has a calibration range that is suited to his experiment. Another item to notice is that the probe with $\alpha_0=0$ has a more limited range of yaw angles than does the probe with $\alpha_0=45$. Lastly, since the probe with $\alpha_0=0$ has larger spaces between successive pitch angles (for yaw angle equal to zero) it has greater pitch angle resolution.

B.6 DATA ACQUISITION AND REDUCTION

There are a few points that should be considered when taking the hot-wire data. Firstly, the linear calibration mentioned above may drift with time so that each time before data is taken this calibration must be set. This precaution is not necessary for the directional calibration because it is expressed as a ratio Ve/V and is only a function of probe geometry. Secondly, the anemometer controls should be checked before each data acquisition session. This includes checking the bridge resistance, the linearizer coefficients, the zero offset and the span.

In the present experiment, all data was stored in direct access memory for later reduction. This reduction, which

involves the solution to the six non-linear equations B.11 through B.16, was accomplished by a numerical root-solving routine.

$$\begin{bmatrix} V_\theta \\ V_r \\ V_z \end{bmatrix} = \begin{bmatrix} \cos(\theta_{pr}-\theta_o) & -\sin(\theta_{pr}-\theta_o) & 0 \\ -\sin(\theta_{pr}-\theta_o) & -\cos(\theta_{pr}-\theta_o) & 0 \\ 0 & 0 & 1 \end{bmatrix} \cdot \begin{bmatrix} 1 & 0 & 0 \\ 0 & \cos\theta_B & \sin\theta_B \\ 0 & -\sin\theta_B & \cos\theta_B \end{bmatrix}$$

$$\begin{bmatrix} \cos\phi & 0 & \sin\phi \\ 0 & 1 & 0 \\ -\sin\phi & 0 & \cos\phi \end{bmatrix} \begin{bmatrix} \cos\theta_t & \sin\theta_t & 0 \\ -\sin\theta_t & \cos\theta_t & 0 \\ 0 & 0 & 1 \end{bmatrix} \begin{bmatrix} V_x \\ V_y \\ V_z \end{bmatrix}$$

TABLE B-1